DESIGNING THE NANOPARTICLE/ELECTRODE INTERFACE FOR IMPROVED ELECTROCATALYSIS

by

SAMANTHA LYNN YOUNG

A DISSERTATION

Presented to the Department of Chemistry and Biochemistry
and the Graduate School of the University of Oregon
in partial fulfillment of the requirements
for the degree of
Doctor of Philosophy

June 2018

DISSERTATION APPROVAL PAGE

Student: Samantha Lynn Young

Title: Designing the Nanoparticle/Electrode Interface for Improved Electrocatalysis

This dissertation has been accepted and approved in partial fulfillment of the requirements for the Doctor of Philosophy degree in the Department of Chemistry and Biochemistry by:

Shannon W. Boettcher	Chairperson
James E. Hutchison	Advisor
Mark C. Lonergan	Core Member
Miriam Deutsch	Institutional Representative

and

Sara D. Hodges	Interim Vice Provost and Dean of the Graduate School

Original approval signatures are on file with the University of Oregon Graduate School.

Degree awarded June 2018

DISSERTATION ABSTRACT

Samantha Lynn Young

Doctor of Philosophy

Department of Chemistry and Biochemistry

June 2018

Title: Designing the Nanoparticle/Electrode Interface for Improved Electrocatalysis

Nanoparticle-functionalized electrodes have attracted attention in areas such as energy production and storage, sensing, and electrosynthesis. The electrochemical properties of these electrodes depend upon the nanoparticle properties, e.g., core size, core morphology, surface chemistry, as well as the structure of the nanoparticle/electrode interface, including the coverage on the electrode surface, choice of electrode support, and the interface between the nanoparticle and the electrode support. Traditionally used methods of producing nanoparticle-functionalized electrodes lack sufficient control over many of these variables, particularly the nanoparticle/electrode interface.

Tethering nanoparticles to electrodes with molecular linkers is a strategy to fabricate nanoparticle-functionalized electrodes that provides enhanced control over the nanoparticle/electrode structure. However, many existing tethering methods are done on catalytically active electrode supports, which makes isolating the electrochemical activity of the nanoparticle challenging. Furthermore, previous work has focused on larger nanoparticles, yet smaller nanoparticles with core diameters less than 2.5 nm are of interest due to their unique structural and electronic properties. This dissertation addresses both of these gaps, exploring small nanoparticle electrocatalysts that are molecularly tethered to catalytically inert electrodes.

This dissertation first reviews and compares the methods of fabricating nanoparticle-functionalized electrodes with a defined molecular interface in the context of relevant attributes for electrochemical applications. Next, a new platform approach to bind small gold nanoparticles to catalytically inert boron doped diamond electrodes through a defined molecular interface is described, and the influence of the nanoparticle/electrode interface on the electron transfer properties of these materials is evaluated. The next two studies build upon this platform to evaluate molecularly tethered nanoparticles as oxygen electroreduction catalysts. The first of these two describes the systematic study of atomically precise small gold clusters, highlighting the influence of atomic level differences in the core size and the electrode support material on the catalytic properties. The second study extends the platform approach to study small bimetallic silver-gold nanoparticles produced on the electrode surface and highlights the influence of the structural arrangement of the metals on the catalytic activity. Finally, future opportunities for the field of molecularly tethered nanoparticle-functionalized electrodes are discussed.

This dissertation includes previously published and unpublished co-authored material.

CURRICULUM VITAE

NAME OF AUTHOR: Samantha Lynn Young

GRADUATE AND UNDERGRADUATE SCHOOLS ATTENDED:

University of Oregon, Eugene, OR
Truman State University, Kirksville, MO

DEGREES AWARDED:

Doctor of Philosophy, Chemistry, 2018, University of Oregon
Bachelor of Science, Chemistry – ACS Certified, 2012, Truman State University

AREAS OF SPECIAL INTEREST:

Nanomaterial Characterization
Small Angle X-ray Scattering
X-ray Photoelectron Spectroscopy

Electrochemistry
Heterogeneous Electrocatalysis

PROFESSIONAL EXPERIENCE:

Graduate Research Employee, Hutchison Laboratory, University of Oregon, 2013-2018

Graduate Teaching Employee- General Chemistry Laboratory, University of Oregon, 2012-2013, Fall 2015

Intern, Research Experience for Undergraduates, Materials Science Institute, University of Oregon, Summer 2011

Intern, Summer Undergraduate Research Program, Clemson University, Summer 2010

GRANTS, AWARDS, AND HONORS:

Julie and Rocky Dixon Graduate Student Innovation Award, University of Oregon, 2017-2018

ACS Undergraduate Award in Analytical Chemistry, Truman State University, 2012

PUBLICATIONS:

Young, S. L., Kellon, J. E., and Hutchison, J. E. *J. Am. Chem. Soc.* **2016**, *138*, 13975-13984.

Trotochaud, L. Young, S. L., Ranney, J. K., and Boettcher, S. W. *J. Am. Chem. Soc.*, **2014**, *136*, 6744-6753.

ACKNOWLEDGMENTS

I could not have finished my degree without the help and support from many people. First, I want to thank my advisor Jim Hutchison. Jim, thank you for challenging me to think critically about my work, for helping me to acknowledge my successes, encouraging my professional development, and for supporting my interests outside of chemistry. You have been a role model for how to navigate challenging situations, how to lead and manage, and how to think about the broader implications of our work on the surrounding community and world. I am a better scientist because of you.

I am grateful to Shannon Boettcher, Mark Lonergan, and Miriam Deutsch for being willing to serve on my committee and for their mentorship throughout the years. I had the opportunity to work in both Shannon and Mark's labs during my time at the University of Oregon which were great experiences. I would not have ended up at the University of Oregon for graduate school without the wonderful experience I had in the Lonergan lab as a summer REU student in 2011. Additionally, Chris Weber, Colin Bradley, Ed Elliott, and Lena Trotochaud all mentored me on various projects and helped me develop and gain confidence as a research scientist during the early stages of my research career without judgment.

The Hutchison lab has been a wonderful place to work for the past five years. I owe so much to the past and present members of the Hutchison lab. Bev Smith, Zack Kennedy, and Ed Elliott were all incredibly helpful and welcoming when I first joined the lab. Jaclyn Kellon has been a wonderful collaborator over the years and I am proud of the work we have accomplished together. Adam Jansons, Tatiana Zaikova, Tawney Knecht, Meredith Sharps, Aurora Ginzburg, Susan Cooper, Kenyon Plummer, Brandon

Crockett, Brantly Fulton, Pat Haben, Brandi Baldock, Kris Koskela, and Rick Glover have all been supportive co-workers throughout the years and have made the lab a fun place to work. I want to thank Nic Westcott, Angela DiAscro and Casey Bisted for their work on my projects at various points as undergraduate or rotation students. Additionally, I want to thank the many others who have supported my research in important ways. Without the CAMCOR staff, most of my dissertation would not exist. Jeanne Basom and Janet Macha have been wonderful in helping with important logistics and have saved me from countless hours of dealing with administrative tasks. I want to thank the members of the Boettcher lab for being so willing to share your equipment and lab space with us over the years and for sharing your electrochemical expertise with me.

I am so grateful to the friends and family that have supported me during my time in Eugene. Having brunch with Michaela Stevens, David Stevens, Caitlyn Jackson, and Nick Larkey was a highlight every week. I particularly want to thank Michaela for being a wonderful friend from day one of graduate school. I am grateful to Matt Kast for his friendship and for organizing awesome outdoor adventures. Susan Cooper, Lisa Enman, Annie Greenaway, Conerd Frederickson, Lizzie Cochran, Mike Nellist, Meredith Sharps, Andrea Loes, Adam Jansons, and Loni Kringle have all been wonderful graduate school friends. I also want to thank my friends Samantha and JW Schneider and Kassie McLaughlin, for their support throughout the years. Finally, I want to thank my parents David and Vicki Young, my sister Andrea Young, my grandparents Ron and Melva Gafford, and the rest of my family for their unconditional love and support throughout this process. I am also so grateful to Ben Blue for being a wonderful partner over this past year. I look forward to our adventures together in Seattle for years to come.

TABLE OF CONTENTS

Chapter Page

Chapter Page

Chapter Page

Chapter Page

LIST OF FIGURES

Figure Page

Figure Page

Figure Page

LIST OF TABLES

Table Page

LIST OF SCHEMES

Scheme Page

LIST OF CHARTS

Chart Page

CHAPTER I

INTRODUCTION

Note: Portions of this chapter are expected to appear in an upcoming publication co-authored by Samantha L. Young, Jaclyn E. Kellon, Tawney A. Knecht, and James E. Hutchison. J.E.K. and I equally contributed to the writing of this chapter. T.A.K. provided assistance in compiling references and editorial support. J.E.H. provided editorial support and advice in conceptualizing this work.

Dissertation Introduction

Chemically modifying electrodes has been an active research area for decades. Murray's pioneering work using molecularly modified electrode surfaces to investigate the electron transfer processes for the design of improved molecular electrocatalysts laid the foundation for the functionalized electrode systems being studied today.[1] Many of his insights and predictions from thirty years ago are still relevant today as methods are being developed to modify electrode surfaces with more complex materials such as biomolecules, polymers, and nanomaterials. In particular, nanoparticle (NP)-functionalized electrodes are one class of modified electrodes that are being investigated for many important applications such as electrochemical energy conversion and storage,[2] sensors for biological and environmental applications,[3] and the electrosynthesis of molecules.[4]

The electrochemical activity of NP-functionalized electrodes for a desired application is influenced by several variables. In many cases, NP reactivity is strongly influenced by core size and shape. Variations in size and shape alter the proportion of undercoordinated atoms at the NP surface, dictate which crystalline facets are dominant, and can drastically affect the electronic and optical properties, especially when core size is decreased below 2 nm. For example, the ratio of CO/H_2 produced by AuNP CO_2 electroreduction catalysts was reported to depend on the core size.[5] As the core size decreased, the higher ratio of lowly coordinated atoms favored formation of H_2.

In addition to the core morphology, the chemical environment surrounding the NP can greatly contribute to observed activity. The NP ligand shell can prevent and/or promote chemical reactions and the density of NP coverage and distribution on the electrode surface can influence the electrochemical properties. As an example, the mechanistic pathway and product selectivity for catalysts can depend upon interparticle distance: At higher nanoparticle densities, there is a greater likelihood of reaction intermediates generated at one nanoparticle undergoing further reaction at a neighboring nanoparticle on the electrode. The oxygen electroreduction catalysis pathway was found to be influenced by the catalyst coverage on the electrode surface, with the proportion of peroxide intermediates found to decrease as the density of Pt nanodisk catalysts were increased.[6] Similarly, the proportion of methane and ethylene products produced by CuNP CO_2 electroreduction catalysts was found to increase as the coverage on the electrode surface increased due to the ability of the CO intermediates to be readsorbed and reacted with neighboring CuNPs.[7]

Finally, the interface between the nanoparticle and the electrode is an important variable to consider as it can dictate the electronic communication to between the nanoparticle and the electrode[8] and in some cases produce active sites for applications such as catalysis.[9] The ideal method to fabricate NP-functionalized electrodes would allow control of these variables in order to tune the desired electrochemical response. If one is able to systematically tune NP-functionalized electrode system variables, it may offer control over the desired electrochemical properties, such as facilitating electronic communication between the NP and electrode, designing catalysts that are selective for a specific product, or sensors that are selective for a target analyte.

A simple strategy to fabricate NP-functionalized electrodes is through physical deposition approaches such as electrodeposition or physical vapor deposition. Electrodeposition is one of the earliest strategies used to modify electrode surfaces with nanostructures. Metal ions can be deposited/precipitated out of solution directly onto the electrode surface by the application of a reducing potential. Some control over nanostructure size and density can be achieved by varying electroreduction potential and time. Physical vapor deposition involves the evaporation of a metal under vacuum that then selectively nucleates onto certain facets of a target substrate. Although both methods are convenient strategies to fabricate electrodes with unpassivated NP surfaces, they often yield disperse NP core sizes and have limited control over NP density on the electrode surface.

To allow for the fabrication of electrodes with more highly engineered NPs, solution deposition of preformed NPs has become more popular. The use of preformed NPs allows for more rigorous characterization of the NP system being investigated

through both solution and solid state analytical techniques before attachment to an electrode surface. The most common approaches are solution deposition techniques such as drop-casting, spin-coating, and dip-coating. Although these methods utilize well-characterized NPs, they still yield ambiguity in the density of NP coverage and the chemical environment of the NPs on the electrode. It can be challenging to reproducibly cover the electrode surface with solution deposition methods due to drying effects and sensitivity of coverage to the electrode surface preparation. Electronic communication between the NPs and the electrode is directly impacted by both the NP-electrode interface and the interactions between the NPs. Unless a defined electron transfer pathway is provided, the electron transfer between the NPs and an electrode can be hindered by the electrically insulating ligands that stabilize the NP core. Because efficient communication between the NPs and the electrode is necessary for all NP-functionalized electrode applications, fabrication methods that produce a defined NP-electrode interface are desirable.

Over the past twenty years, significant effort has gone into the design and fabrication of NP-functionalized electrodes with a defined molecular interface. The use of a discrete molecular layer to bind a NP to an electrode surface allows for a higher degree of control over the chemical environment surrounding the NP while retaining the geometric control over the NP core offered through the use of preformed NPs. There are two main methods of fabricating a defined NP-electrode interface: 1) pre-functionalization of the electrode with a molecular monolayer capable of assembling NPs or 2) utilizing the existing NP ligand shell to form a bond to the electrode surface. The use of a defined NP-electrode interface not only yields a more uniform chemical

environment but may afford the opportunity to perform systematic studies to tease out structure-property relationships for all electrochemical applications. This dissertation discusses the use of molecularly tethered NPs to investigate the electrocatalytic properties of small NPs as a function of structure, composition, and catalyst coverage.

Dissertation Overview

Chapter II reviews methods to attach nanoparticles to electrode surfaces through defined interfaces. This work evaluates the different methods of interfacing nanoparticles to electrodes in the context of universal attributes desired for applications of nanoparticle-functionalized electrodes. The studies referenced that are authored by me are expanded upon in following chapters. This work was written collaboratively by me and graduate student Jaclyn E. Kellon. Tawney A. Knecht provided assistance in compiling references and editing the document. Jim Hutchison provided guidance in conceptualizing this work and in the editorial process.

Chapter III is from a previously published article in the Journal of the American Chemical Society (Young, S. L.; Kellon, J. E.; Hutchison, J. E. Small Gold Nanoparticles Interfaced to Electrodes through Molecular Linkers: A Platform to Enhance Electron Transfer and Increase Electrochemically Active Surface Area. *J. Am. Chem. Soc.* **2016**, *138* (42), 13975-13984). This work describes a new approach to attaching small gold nanoparticles to electrodes through a defined molecular interface. By utilizing the photochemical reaction between terminal alkenes and boron doped diamond surfaces, we developed two methods to attach small gold nanoparticles to boron doped diamond electrodes through alkanethiolate linkers. The electrochemical properties of these molecularly interfaced nanoparticles were investigated using a ferrocene redox probe

tethered to the nanoparticle surface. The deliberately bound, molecularly interfaced nanoparticles displayed much more efficient electron transfer than when the same nanoparticles were simply deposited onto an electrode. The defined monolayer of nanoparticles resulting from molecular tethering resulted in a higher electrochemically active surface area compared to the deposited nanoparticles. The experimental work and writing of this chapter was performed equally between Jaclyn E. Kellon and me. Jim Hutchison provided guidance on experimental design and editorial support.

The method of constructing nanoparticle-functionalized electrodes described in Chapter III, involving the use of preformed, well-characterized nanoparticles, a catalytically inert electrode support, and a defined nanoparticle/electrode interface, enables systematic studies of the electrocatalytic properties of nanoparticles for important applications. Chapter IV demonstrates how four small ($d_{core} < 1.7$ nm) triphenylphosphine-stabilized gold clusters/nanoparticles can be tethered to boron doped diamond electrodes and evaluated as electrocatalysts for the oxygen reduction reaction. The effect of very small changes in core size (a few atoms) was able to be observed for a catalytically interesting size regime using rotating ring disk voltammetry. Further, effects of the electrode support and NP coverage on catalytic activity were identified. The experimental work and writing of this chapter was performed by me. Jim Hutchison provided advice on experimental design and editorial support.

Chapter V expands the platform described in Chapter III to incorporate bimetallic silver-gold nanoparticles. Through the use of underpotential deposition/galvanic exchange or anti-galvanic reduction, a series of silver-gold nanoparticles with different elemental compositions were rapidly fabricated while retaining the benefits of the

platform, namely the monodisperse core size and the defined molecular interface. This enabled a systematic study of the effect of elemental composition on the activity of silver-gold nanoparticles towards the oxygen reduction reaction in alkaline conditions. The location of the two metals in the nanoparticle has a surprising influence on the catalytic activity of the nanoparticles. The experiments and writing of this chapter were done by me. Jim Hutchison provided guidance on experimental design and editorial support.

The work presented in this dissertation provides a general strategy to fabricate nanoparticle-functionalized electrodes with control over important variables such as the nanoparticle core size, elemental composition, and its interface to an electrode support. This should enable rapid screening of nanoparticle catalysts and provide insight into how to design better catalysts in the future.

CHAPTER II

DEFINING THE INTERFACE FOR NANOPARTICLE-FUNCTIONALIZED ELECTRODES

Note: Portions of this chapter are expected to appear in an upcoming publication co-authored by Samantha L. Young, Jaclyn E. Kellon, Tawney A. Knecht, and James E. Hutchison. J.E.K. and I equally contributed to the writing of this chapter. T.A.K. provided assistance in compiling references and editorial support. J.E.H. provided editorial support and advice in conceptualizing this work.

This review will discuss and evaluate the different methods currently in use that employ a molecular linker to tether NPs to an electrode. First, the different methods will be reviewed, and then each method will be compared using universal attributes of interest for all applications of NP-functionalized electrodes: uniformity of the NP-electrode interface and resulting NP distribution, electronic communication between the NP and electrode, stability, and overall system tunability. Finally, predictions are made for the future directions of molecularly tethered NP-functionalized electrodes for creating advanced, multi-functional materials for important applications which will be enabled through the expansion of these fabrication methods coupled with improved analytical techniques.

Methods of fabricating a nanoparticle-functionalized electrode with a defined interface

Common strategies to construct nanoparticle (NP)-functionalized electrodes with a defined NP-electrode interface are to either assemble preformed NPs onto an electrode functionalized with molecular tethers via ligand exchange or use the NP ligand shell to form the interface (Scheme 2.1). The initial functionalization of the electrode is generally accomplished through either self-assembly chemistry or through grafting reactions. The NP ligand shell can be either directly bound to the electrode surface or it can be coupled to an existing molecular tether on the electrode. These approaches will be further described below using examples from the literature.

Scheme 2.1. General strategies to fabricate nanoparticle-functionalized electrodes with a defined NP-electrode interface.

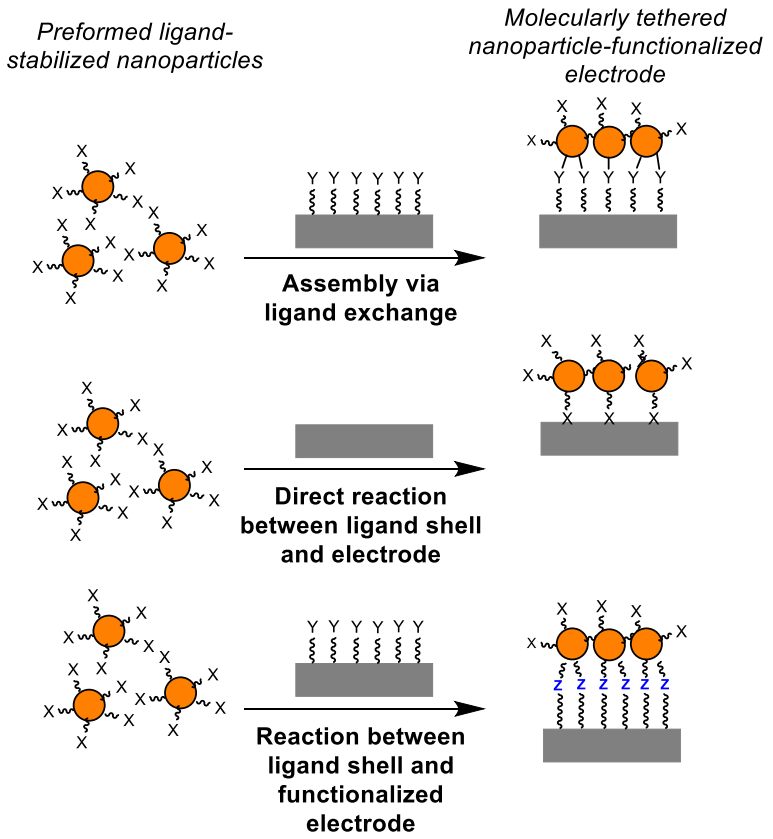

Assembly of nanoparticles onto molecularly functionalized electrodes through ligand exchange. The most common approach to fabricating a NP-functionalized electrode with a molecularly defined interface is to first modify the electrode substrate with a molecular linker. This linker typically contains a terminal functional group or charged moiety capable of capturing preformed nanoparticles through either ligand exchange or electrostatic interactions, respectively. The functionalization of the electrode surface to enable subsequent NP assembly is typically accomplished through the formation of a self-assembled monolayer (SAM), the deposition a polyelectrolyte onto an electrode substrate or a SAM, or grafting reactions. These functionalization methods will be discussed below in the context of NP assembly.

Assembly onto self-assembled monolayer linkers on electrode surfaces. Self-assembled monolayers (SAMs) can be formed on both metallic and non-metallic electrode substrates. Research done on SAMs has been extensively reviewed and will not be the subject of this paper.[1,2] Three different molecular linker-electrode chemistries are commonly used to form SAMs on an electrode surface: thiol-noble metal electrode, alkoxysilane-non-metallic electrode, and polyelectrolyte or polyelectrolyte-SAM-electrode architectures. The most common terminal functionalities used to assemble a variety of NP materials are thiol, amine, and carboxylic acids moieties.

The use of thiol SAMs to functionalize electrodes is most often done on single crystal or polycrystalline noble metal electrodes (Pt, Ag, and most often Au). These electrodes are submerged in a solution of molecules containing a terminal thiol functional group which forms a strong bond with the electrode, resulting in a molecular monolayer. The other end of the SAM contains a functional group capable of assembling NPs such as

thiols,[3–5] amines,[6,7] and carboxylic acids.[8] For example, the size dependent electrochemical properties of Au nanorods were studied through their assembly on hexanedithiol modified gold electrodes.[9] Thiol SAMs with different terminal functionalities can be used together to form mixed molecular monolayers. These systems can be used to control the NP density on the SAM surface through the introduction of a diluent ligand, such as a hydroxy-terminal SAM which does not interact strongly with the NP core material.[8] A wide variety of molecular composition can be introduced into the interior of the SAM such as conjugation,[10] aromatic moieties,[10,11] and redox active gates/bridges.[4,5] CdSe quantum dots were assembled onto a variety of dithiol SAM modified gold electrodes to investigate the electron tunneling rate dependence on linker length and interior composition.[11] Furthermore, three-dimensional architectures can be achieved through layer-by-layer assembly of alternating SAM-NP-SAM exposures.[8,12,13]

Functionalized alkoxysilanes are another class of molecules that have been widely used to form self-assembled monolayers on surfaces. These monolayers are formed through condensation reactions with hydroxyl groups on the electrode surface to form electrode-O-Si linkages between the electrode and the alkoxysilane. This chemistry is most commonly used to functionalize tin-doped indium oxide (ITO) electrodes[12,14–17] but has also been employed with surface oxidized silicon[12] and boron-doped diamond (BDD).[18] After molecular monolayer assembly, the distal functional group on the silane is used to assemble NPs. The most common alkoxysilanes used are 3-(aminopropyl)-triethoxysilane (APTES)[12,14,16,18] and 3-(mercaptopropyl)-trimethoxysilane (MPTMS),[12,14,17–20] both of which are commercially available. This chemistry was used to assemble AuNPs onto APTES or MPTMS-functionalized BDD and the different

tethering chemistries were compared to physiadsorbed NPs on BDD in regard to their stability and electron transfer properties.[18] AuNPs (d_{core} ~14 nm) were tethered to both APTES and MPTMS-functionalized ITO electrodes and the influence of the AuNP tethering chemistry on the electrocatalytic activity towards methanol electrooxidation was investigated.[14]

Another method utilizing a self-assembled molecular linker to assemble NPs is the use of polyelectrolytes. Polyelectrolytes are ionically charged polymers that electrostatically assemble either directly onto a bare electrode surface[21–23] or onto carboxylic acid terminated SAM-functionalized electrodes.[8,24–31] In contrast to assembling NPs onto the electrode through forming covalent bonds with the NPs as in the thiol or amine terminated SAMs, the polyelectrolyte layers capture NPs through electrostatic interactions. This strategy has been reported to capture a wide variety of NP core materials through electrostatic interactions including diamond,[21] gold,[22,23] palladium,[22,32] and semiconductor quantum dots.[1,24] Commonly used polyelectrolytes to assemble NPs are poly-L-lysine (PLL), poly(diallyldimethylammonium) chloride (PDADMAC), poly(amidoamine) (PAMAM) and poly-L-arginine (PLA), all of which are cationic. This method was used to assemble different sizes of CdTe and CdSe quantum dots onto PDADMAC modified carboxylic acid SAMs on planar Au electrodes to investigate the influence of core size on the charge transfer properties of these materials.[1] AuNPs and nanorods were assembled onto poly(styrenesulfonate)-APTES-functionalized ITO electrodes to study the influence of core size and shape on their electrocatalytic activity towards methanol electrooxidation and oxygen reduction.[33] The influence of the lattice strain of PdNPs on their ability to adsorb hydrogen was probed by

assembling PdNPs onto PLL-modified ITO electrodes to inform future catalytic studies.[22] This approach has also been utilized to fabricate and investigate the electrochemical properties of nanocomposites, such as graphene-NP materials.[34]

Assembly onto grafted linkers on electrode surfaces. Grafting chemistry is an alternative approach to modify surfaces with molecular tethers. Grafting reactions are initiated through electrochemical, photochemical, or thermal generation of a radical which can then bind to an electrode surface. This approach generally forms covalent carbon-electrode bonds between the linker and the electrode material.

Electrochemical grafting has been used to graft molecules to the surface of electrodes to produce functionalize electrodes that facilitate nanoparticle assembly. The reduction of aryl diazonium molecules has been used to functionalize electrode surfaces through grafting and has been the subject of several reviews.[35,36] Diazonium ions are generated *in situ* through the reaction of nitrite with substituted arylamines because most diazonium compounds are not shelf stable. The intermediate aryl diazonium molecule is then electrochemically reduced to produce a radical that reacts with the electrode surface. Electrode supports that can sufficiently reduce the diazonium molecule and react with the generated radical can be modified with this approach. This approach has been used to functionalize different carbon surfaces, noble metals, and metal oxide surfaces with aryl molecules possessing many different functional groups such as carboxylic acid,[37] amine, azide,[38] thiol,[39,40] and nitro groups[41,42] which can be used to capture NPs. AuNPs (d_{core} ~ 16-30 nm) have been assembled onto aminophenyl and thiophenol functionalized glassy carbon electrodes modified through the diazonium reduction to evaluate the stability of the interface[39] and its use as a biosensor to detect antibodies.[43] Other similar

electrochemical reduction techniques for non-aryl diazonium molecules have also been used to modify electrode surfaces. Poly(ethylenediamine) has been electrochemically grafted to glassy carbon and graphite electrodes to generate a series of samples with varying interface thicknesses to study NP-mediated electron transfer.[44] In addition to assembling NPs, the electrodeposition of these NPs onto an interface generated through electrochemical reduction has been reported.[40,42]

Photochemical grafting is another method used to functionalize electrode surfaces with a molecular interface to assemble NPs. The photochemical grafting of alkenes to boron doped diamond electrodes was pioneered by the Hamers group and is generally accepted to occur through the photoemission of an electron from the substrate into the acceptor level of the alkene. This chemistry has been expanded to functionalize amorphous carbon, silicon, metal oxide, and metal nitride surfaces generally through the same mechanism.[45,46] Larger AuNPs (d_{core} ~15-40 nm) have been assembled onto amine functionalized boron doped diamond (BDD) generated through photochemical grafting allylamine to study the stability of the interface and the electron transfer properties.[47] Smaller AuNPs (d_{core} < 2 nm) have also been assembled onto thioacetate or thiol molecular monolayers generated from grafting undecenyl-thioacetate to boron doped diamond electrodes. Using this approach, the effect of core size and the interface on NP-mediated electron transfer was studied for this smaller NP core size regime.[48] In contrast to the use of alkenes, irradiating elemental sulfur or carbon disulfide was reported to functionalize diamond surfaces with sulfur groups to facilitate the assembly of AuNPs.[49]

Silicon electrodes have been functionalized though hydrosilylation reactions through heating alkenes or alkynes which then react with the substrate surface. AuNPs

were assembled onto thiol monolayers on silicon electrodes through heating a trifluoroacetyl (TFA)-protected alkenylthiol to functionalize the electrode and then removed the TFA protecting group to enable NP assembly through Au-thiolate bonds.[50] Alkyne monolayers on silicon were generated by heating 1,8-nonadiyne and were further functionalized through "clicking" an azide with a terminal amine to the monolayer that was able to capture the AuNPs.[51]

Utilizing the nanoparticle ligand shell to form the interface. This approach leverages terminal functionality in the NP stabilizing ligand shell to bind the NP to the electrode surface instead of assembling NPs onto molecularly modified electrodes through ligand exchange reactions. This is typically accomplished by a reaction between a functional group in the nanoparticle ligand shell with either an existing molecular tether on the electrode surface or the electrode substrate itself. Both strategies will be described in this section.

Attachment to a pre-functionalized electrode. The development of efficient chemistries in organic synthesis such as click chemistry and host/guest supramolecular chemistry has been expanded to couple nanomaterials to surfaces. Improved nanoparticle syntheses have enabled the incorporation of functional groups that can undergo chemistry with an electrode containing an appropriate functional group. The combined use of these advances in synthesis have been used to link NPs to electrodes through several different approaches.

In synthetic organic chemistry, two different molecules are often bound to each other through coupling chemistry. Coupling reactions have also been applied to bind nanoparticles to functionalized electrodes through their ligand shells. The copper(I)-

catalyzed azide-alkyne cycloaddition, the most well recognized of the "click chemistry" reactions proposed by Sharpless et al.,[52] has been used to couple nanoparticles to functionalized electrode surfaces. Gold nanoparticles (d_{core} = 10-13 nm) with undecyn-1-thiolate ligands were bound to azide-functionalized glassy carbon electrodes through this azide-alkyne cycloaddition reaction, and these AuNP functionalized electrodes were demonstrated to selectively catalyze the electrooxidation of nitrite in the presence of competing pollutant ions.[38,53] Molecularly linked multilayer structures of Au, TiO_2 and SiO_2 nanoparticles were constructed on Au, silicon, ITO, and stainless steel electrodes through "clicking" azide functionalized NPs and alkyne-functionalized NPs to each other in a layer by layer assembly approach.[54] These metallic and semiconductor NP heterostructures were demonstrated to be catalytically active towards the photochemical degradation of dyes, methanol electrooxidation, and electrochemical water splitting. The azide-alkyne click chemistry has also been demonstrated without the copper catalyst by using strained alkynes. Magnetite (Fe_3O_4) NPs possessing strained cyclooctynes in their ligand shell were reacted with azide-functionalized silicon electrodes to tether the NPs to the surface.[55] The formation of amides through the reaction between carboxylic acids and amines has also been used to functionalize electrode surfaces with NPs. Carboxylic acid AuNPs (d_{core} ~3 nm) were reacted with amine-functionalized planar Au electrodes to link the AuNP to the electrode through amide bonds.[56] Subsequently, a protein was bound to the AuNP surface to study its electron transfer properties using this electrode structure.

Another approach to attach NPs to functionalized electrodes though their ligand shells is to use strong non-covalent interactions such as host/guest chemistry or

interactions of metal ions with molecules. The interaction of biotin ligands with the protein avidin is one of the strongest non-covalent interactions known in nature,[57] and this interaction has been used to bind NPs to electrode surfaces. Avidin or biotin were coupled to the carboxylic acid ligand shell of ~12 nm AgNPs, and these functionalized AgNPs were then bound to biotin or avidin functionalized planar Au electrodes respectively in order to study their electron transfer properties.[58] A similar strategy was used to assemble ~60 nm AgNPs onto planar Au electrodes through the biotin/avidin interaction in order to construct amperometric sensors to detect the pesticide dimethoate.[59] Strong non-covalent interactions have also been formed using synthetic host/guest supramolecular chemistry and have been used to tether NPs to electrodes. The ability of cyclodextrin and calixarene to strongly bind guest molecules has been used for this purpose. AuNPs with cyclodextrin terminal ligands were bound to a planar Au electrode functionalized with a monolayer possessing terminal iron porphyrin compounds through supramolecular interactions between the cyclodextrin and the metalloporphyrin.[60] Similarly, cyclodextrin-functionalized AuNPs were bound through interactions between the cyclodextrin ligand and terminal ferrocenes on the functionalized ITO electrode.[61] This electrode was active towards the electrooxidation of ascorbic acid. The interactions between metal ions and carboxylic acids is another linking chemistry that has been used to bind NPs to electrodes using their ligand shells. Carboxylic acid-functionalized AuNPs ($d_{core} \sim 2$ nm) were bound to carboxylic acid SAMs on planar Au through the use of Zn^{2+} as a bridge.[62]

Direct binding of the nanoparticle ligand shell to the electrode surface. Whereas the previous section described the binding of the NP ligand shell to a preformed

molecular layer on the electrode surface, another strategy is to bind the ligand shell *directly* to the bare electrode surface. This has been typically accomplished using the grafting chemistry described previously. Alkenethiolate stabilized AuNPs (d_{core} ~ 4 nm) have been interfaced to silicon substrates through Si-C bonds using thermal hydrosilylation reactions.[63] Photochemical grafting reactions were used to bind small alkenethiolate stabilized AuNPs (d_{core} 0.8-2.5 nm) to BDD through covalent C-C bonds and were used to study the electron transfer properties as a function of core size in this small size regime.[48] AuNP/graphene oxide nanocomposites were formed by the reduction of the diazonium group generated from phenylamine ligands.[64]

Evaluation of NP-functionalized electrode fabrication methods for attributes relevant to electrochemical performance

There are several attributes that are generally important across all applications of nanoparticle-functionalized electrodes. These attributes include: (1) uniformity of the NP/electrode interface and the resulting distribution of NPs across the electrode surface, (2) sufficient electronic communication between the NP and the electrodes, (3) the stability of the functionalized electrode, and (4) the ability to further modify the electrode after fabrication. For some attributes, the choice of general strategy to construct NP-functionalized electrodes, either through assembly onto molecular linkers or using the NP ligand shell for attachment is the main factor in imparting the desired properties. In other cases, the choice of NP binding chemistry or electrode support material is the more important variable regardless of if the NPs are assembled through ligand exchange or bound through their ligand shell. The different methods of fabricating nanoparticle-

functionalized electrodes will be evaluated and compared in the context of these universal attributes desired for electrochemical performance.

Uniformity of the molecular interface and resulting nanoparticle distribution on the monolayer surface for producing consistent electrochemical performance. In order to extract reliable structure-property relationships for NP-functionalized electrodes, the NPs should all be in a uniform chemical environment such that they are the same distance from the electrode and neighboring particles. While different applications may require different molecular monolayer features in terms of monolayer/NP density, methods to reproducibly produce a uniform molecular monolayer with a uniform NP distribution on this interface is typically desired for all applications.

Density and ordering of the interface. Some studies rely on a dense, insulating molecular monolayer that completely passivates the electrode surface. The systems that lead to the highest molecular densities are fully-saturated alkanethiol SAMs on gold and electrochemically grafted ethylenediamine on glassy carbon. Both methods offer control over the extent of electrode passivation by altering the SAM length or organic layer thickness respectively. Alkanethiol SAMs on gold can form crystalline-like interfaces on single crystal gold electrodes that typically passivate the electrode substrate.[65–67] Although these SAMs generally lead to complete electrode passivation, defects in the electrode substrate can lead to pinholes and disorder in the SAM.[68,69] Gooding and co-workers were able to control the thickness of the poly(ethylenediamine) organic layer, ranging from 6.6 ± 1.3 Å to 37.7 ± 1.2 Å, through successive cycling at anodic potentials.[44] Although both methods provide tunability in the extent of electrode passivation, each has its limitations. SAMs offer a monolayer of uniform density and

thickness, but bi-functionalized SAMs of greater than 18 methylene units are not achievable. Conversely, greater thicknesses can be achieved in poly(ethylenediamine) systems, but these layers suffer from variable thicknesses across the electrode surface leading to a non-uniform NP/electrode interface. Despite each method's limitations, both can yield a dense, completely passivated electrode surface.

It is not always necessary that the electrode surface be fully passivated. Depending on the nature of the study, the electrode material and electronic conductivity of the interface may be more important. Non-metallic electrodes require the use of either alkoxysilane, polyelectrolyte or chemically grafted monolayers, each of which offer different levels of control over the interface uniformity. The two commonly used alkoxysilane molecular monolayers, APTES and MPTMS, yield different monolayer densities. APTES forms a sparse monolayer while the MPTMS is more dense, but still not completely passivating.[14,18] Furthermore, silane chemistry is prone to polymerization/cross-linking thus leading to ambiguity in both interface thickness and chemical environment. Photochemical grafting of alkenes results in sparse, disordered monolayers with shorter alkenes being more ordered than longer alkenes.[70] Multilayer formation can occur during the electrochemical grafting of aryl diazonium molecules which can lead to variability of interface thickness.[71] Although this can be prevented using radical scavengers during the grafting reaction[72,73] or by incorporating bulky substituents[74–76] into the linker molecule, there is a potential trade-off between interface density and uniformity.

Uniformity of nanoparticle distribution on the electrode surface. When investigating the electrochemical properties of NPs, it is critical that the data are not

convoluted by multiple NP-chemical environments. Although either a submonolayer of discrete NPs or a dense monolayer are desirable for different applications/studies, a surface with variations in NP distribution across the surface can lead to variability in the observed electrochemical properties. The formation of NP aggregates on the electrode surface can lead to irreproducible results since it is challenging to control the degree of aggregation. The terminal functionality of alkoxysilane SAMs have been reported to influence the molecular monolayer density and the overall distribution of NPs on the monolayer. The use of the MPTMS tether has been reported to yield uniform, sub-monolayer coverage of gold nanoparticles while the APTES tether results in an aggregated sub-monolayer of gold NPs (Figure 2.1).[14,18] Alkanethiol SAMs provide control over NP density through two methods: the use of mixed SAMs and NP exposure time. The use of a non-coordinating, diluent ligand in combination with a SAM capable to NP assemble serves to both prevent NP aggregation and control the NP density.[8] Additionally, Chirea et. al. were able to control the density of gold nanorods on alkanethiol SAMs by altering the length of time the SAM-modified electrode was exposed to the solution of gold nanorods.[77]

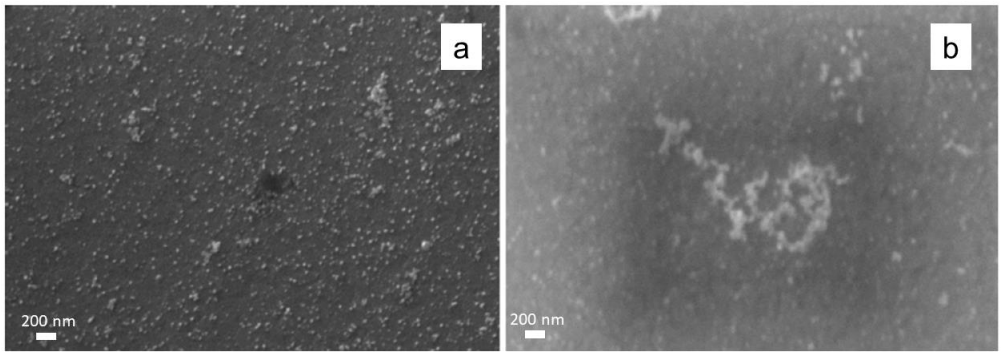

Figure 2.1. Scanning electron micrographs of AuNPs on MPTMS-ITO (a) and APTES-ITO (b) electrodes. Adapted from ref. 14.

Similar to alkanethiol/amine SAM systems, molecular monolayers formed through grafting reactions have been shown to yield evenly dispersed, submonolayers of NPs on their surface.[39,48] Using the NP ligand shell to directly graft NPs to electrodes or to bind them to a molecular monolayer through coupling chemistry has also been shown to yield an evenly dispersed submonolayer of nanoparticles on the electrode surface given that the NP cores are stable to the reaction conditions.[38,48,63] In studies that grafted alkenethiolate-AuNPs to silicon electrodes through hydrosilylation reactions, significant core growth and aggregation was observed when reactions were performed at higher temperatures where the NPs were destabilized.[63]

Facilitating electronic communication through the NP-electrode interface. When fabricating NP-functionalized electrodes for a given application, it is typically desirable that there not only be communication between the NP and the electrode, but that this electron transfer is fast. Incorporating a molecular monolayer that separates the NP from the electrode substrate adds another barrier to electron transfer. Good electronic communication between the NP and the electrode may directly impact the sensitivity of amperometric sensors and the overpotential of electrocatalysts. Additionally, for fundamental electron transfer studies the observed rates of electron transfer should not be limited by the NP-electrode electron transfer step (unless that is what is being probed). The electronic communication between a NP and the electrode surface is influenced by nanoparticle core size and the thickness/length and interior composition of the linker.

Molecular monolayer thickness/length, interior composition and nanoparticle size. Prior to NP assembly, a molecularly functionalized electrode often impedes electronic communication between a redox probe and the electrode surface. It has been

well established that the addition of NPs to electrodes functionalized with an insulating molecular layer restores electronic communication between a solution phase redox probe and the electrode (Figure 2.2a). Chazalviel and Allongue provided a theoretical framework explaining NP-mediated electron transfer through a molecular monolayer as a function of both the monolayer thickness and nanoparticle core size (Figure 2.3).[78] The rate of NP-mediated electron transfer across an insulating molecular monolayer is inversely proportional to the thickness/length of that monolayer. Additionally, the effect of insulating molecular monolayer thickness/length on NP-mediated electron transfer has a greater impact for small NPs (d_{core} < 10 nm) than larger NPs.

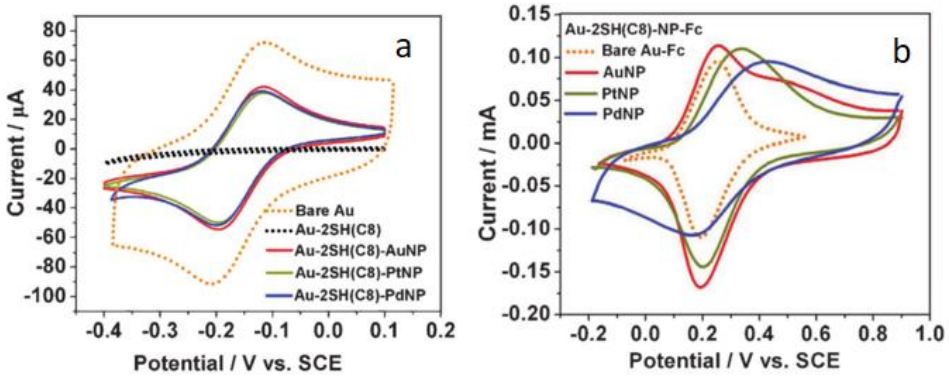

Figure 2.2. Cyclic voltammograms of a bare Au electrode, 1,8-dithiol functionalized Au electrode and AuNPs, PdNPs and PtNPs assembled onto 1,8-dithiol functionalized gold electrodes with a ruthenium hexamine solution phase redox probe (a) and a tethered ferrocenyl redox probe (b). Figure adapted from ref 3.

Consequently, it is important to take into consideration both the NP core size and linker length when designing a NP-functionalized electrode system with a defined molecular interface. Small NPs are of interest as active materials for many applications due to their unique electronic and structural properties compared to their larger counterparts. If using small NPs, much consideration should be put into how those

particles will be interfaced to the electrode as to not unintentionally reduce NP-electrode electronic communication. For example, while the attachment of larger NPs through their ligand shell to a ligand-functionalized electrode has proven effective, the longer linker lengths associated with this method could hinder NP-mediated electron transfer when using small NPs. For applications where fast electron transfer is needed, methods that can incorporate shorter molecular linkers are beneficial to decrease the tunneling barrier. Another strategy to enhance the rate of electron transfer between the NP and electrode is to use conjugated linkers. To incorporate conjugation or aromaticity into the molecular monolayer, either thiol SAMs on gold or aryl diazonium electroreduction methods should be employed.

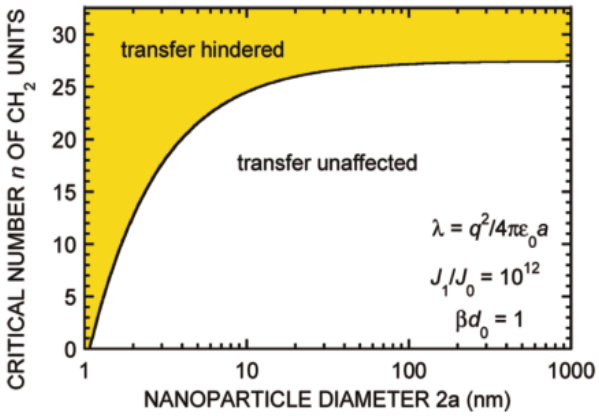

Figure 2.3. Critical number *n* of CH_2 units above which a SAM coated with gold nanoparticles is expected to lead to a change in the voltammogram of a reversible redox system in solution (shaded area) as compared to that obtained on a bare gold electrode. Adapted from ref. 78.

Ability to characterize nanoparticle-mediated electron transfer. Regardless of application, understanding the NP-mediated electron transfer kinetics is important when investigating the electrochemical properties of NP-functionalized electrodes. When measuring the NP electrochemical activity, it is beneficial to be able to distinguish

between the NP activity and that of the other system components, such as the underlying electrode substrate. Typically, redox probes are used to characterize the electronic properties of NP-functionalized electrodes. Redox probes can either be dissolved in the electrolyte solution, (solution phase probes), or directly bound to the NP surface, (surface bound probes). Although solution phase probes are most commonly used for characterization, they have some limitations. When using a solution phase probe, a dense, fully passivating molecular monolayer is required to ensure that any electrochemical response is NP-mediated and not a result of the probe interacting directly with the electrode material. A solution phase redox probe is appropriate when using thiol SAMs, MPTMS alkoxysilane SAMs and electrochemical grafting methods. Conversely, APTES alkoxysilane SAM, and polyelectrolyte monolayers enhance electron transfer between a solution phase redox probe and the electrode material.[14,18,25] It is hypothesized that this enhancement is a result of the redox probe accumulating on the ionic surface of the monolayer, thus reducing diffusion limited electron transfer rates.

If the NP-electrode interface does not result in a fully passivated electrode, a surface bound redox probe may be more appropriate to characterize NP-mediated electron transfer. When employing a surface bound redox probe there are a few considerations to be made. It is important that the probe only binds to the NP, not the underlying molecular interface or electrode substrate. The probe can either be bound directly to the NP core or through the NP ligand shell. In either case, the probe should not have an affinity for the electrode material. Furthermore, for fabrication methods that yield a sparse molecular monolayer that NPs are assembled onto, it is important that the redox probe cannot associate or bury itself into the molecular monolayer and come into

direct contact with the electrode material which could result in measuring electron transfer that is not NP-mediated. This can be prevented through the incorporation of a hydrophobic/hydrophilic group within the redox probe that is not compatible with the relative hydrophobicity/hydrophilicity of the molecular monolayer. Unlike solution phase probes, appropriate surface bound probes may not be commercially available and may require synthesis. If all of these considerations are met, a surface bound probe is a great way to ensure any observed electrochemical activity is due to the NPs.

Redox probes have different mechanisms and rates of electron transfer. Solution phase probes can either undergo inner or outer sphere electron transfer, both of which are slower than surface bound redox probes. Liu et. al. nicely demonstrated the importance of redox probe when studying NP-mediated electron transfer.[3] They looked at Au, Pt and Pd NP-dithiol-gold electrode systems using both solution phase and surface bound redox probe. While minimal differences in electrochemical behavior were observed with the solution phase probe, differences in electrochemical behavior of both the NP core material and in SAM length were observed using a surface bound probe (Figure 2.2b). They conclude that the electrochemical behavior of these systems was being limited by the electron transfer rate of the solution redox probe.

Resistance to desorption or degradation to preserve long-term electrochemical performance. The NP, molecular interface, and electrode support of NP-functionalized electrodes need to be stable to desorption, to chemical degradation, and to NP aggregation over long periods of time to realistically be useful for commercial applications. In the context of nanoparticles tethered to an electrode through a molecular interface, both the electrode-molecular interface and the NP-molecular interface should

be evaluated for their ability to preserve the intended system morphology by preventing NP desorption and aggregation. Furthermore, the electrode substrate must be compatible with the desired operating conditions.

Both the stability of the electrode material and the electrode-interface are important for retaining sufficient electronic communication between the NP and the electrode over time. The electrolyte and potential window required for a study often dictate which electrode support is most appropriate. For example, silicon electrodes will dissolve in alkaline electrolytes limiting their application in acidic or non-aqueous electrolytes. Silicon can also easily form electrically insulating oxide layers in aqueous electrolytes unless the electrode surface is completely passivated by a molecular layer. A decrease in electron transfer rates for AuNP-functionalized silicon electrodes was observed over ~50 cycles in an aqueous solution of $Ru(NH_3)_6^{3+}$ which was attributed to the formation of insulating SiO_x underneath the molecular monolayer (Figure 2.4).[51] In contrast, carbon electrodes can be operated in acidic, alkaline, and non-aqueous electrolytes without concern of dissolution or oxidation of the surface. Boron doped diamond (BDD) in particular has been reported to have a remarkable stability across a wide potential window since it is inert towards hydrogen or oxygen evolution catalysis which can limit the available potential window for metallic electrodes or other carbon electrodes.[79]

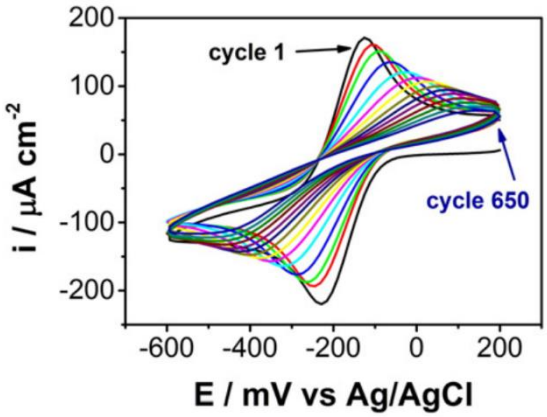

Figure 2.4. Cyclic voltammograms of a AuNP-functionalized Si electrode in an aqueous solution of $Ru(NH_3)_6^{3+}$ every 50 cycles up to 650 cycles. The diminished electrochemical response with increasing cycles is believed to cause by the formation of an insulating SiO_x layer at the electrode surface. Adapted from ref 51.

Similarly, the choice of interface chemistry can also limit or enable operation of the electrode under certain conditions. The strength of the bond of the molecular monolayer to the electrode substrate will influence the probability of interface desorption. Covalent carbon-carbon bonds, which are formed in electrode modification methods such as aryl diazonium electrochemical reduction or photochemical grafting of alkenes, are anticipated to be stable since a significant amount of energy is required to break that bond. These interfaces have been reported to be stable over many cycles as determined through preservation of the redox activity of the bound nanoparticle or organometallic catalysts.[39,80] In contrast, self-assembled monolayers of thiols on planar noble metal electrodes have been reported to desorb from the electrode surface under reducing potentials in alkaline media which could potentially limit application in those conditions.[81,82]

The NP-molecular interface chemistry will determine the likelihood of NP desorption or aggregation during electrochemistry. In general, covalent bonds between

the NP and the interface are anticipated to be more stable to both desorption and aggregation than electrostatic interactions. Furthermore, the presence of stabilizing ligands on the nanoparticle surface can also preserve the NP core by preventing core dissolution or fusion during electrochemistry. These ligands are present in many nanoparticles that are assembled onto or reacted with an interface, but not on NP-functionalized electrodes fabricated through electrodeposition or electrostatic adsorption. The interface chemistry can be sensitive to pH which can cause nanoparticle desorption or aggregation. The morphology and coverage of citrate-stabilized AuNPs assembled on electrodes through Au-amine bonds have been observed to be influenced by pH with NP desorption occurring as the pH is increased due to deprotonation of the amine which inhibits electrostatic interactions allowing nanoparticle desorption (Figure 2.5).[47] AuNPs assembled onto amine-terminated silane monolayers have shown an increase in aggregation on the surface in contrast to assembly onto thiol-terminated silanes.[14,33]

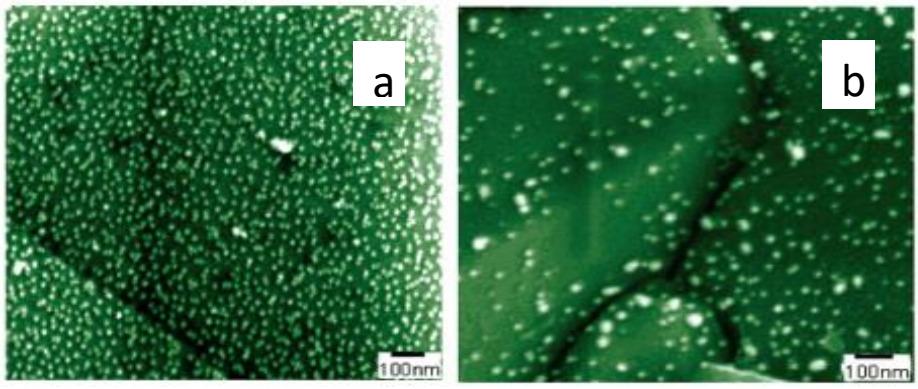

Figure 2.5. Scanning electron micrographs of AuNPs assembled onto amine-terminated BDD electrodes immersed into different pH Au colloidal solutions: (a) pH = 4, (b) pH = 5. Adapted from ref 47.

Ability to tune or modify the electrode structure or composition post-electrode fabrication to access to additional properties. For general use with many

types of NPs and for many different applications, it is desirable to have access to a number of different structures and/or have opportunities to manipulate the structure post-fabrication to create more advanced materials. This can include the ability to vary the interface length/thickness, control over the density of NP coverage on the electrode surface, and incorporate additional functional ligands, metals, or nanoparticle layers onto the surface of the bound nanoparticle.

The length of the interface influences the electron transfer between the NP and the electrode as discussed above as well as the steric arrangement of the nanoparticles on the surface, so for certain applications or studies, it might be desirable to have the ability to vary this interface. For fabrication methods such as self-assembly of molecular linkers or photochemically or thermally grafting alkene linkers onto electrode surfaces, there is no inherent limitation to the length of the molecular tether assuming it is stable and can be synthesized. The aryl diazonium grafting method is limited to an aryl group as the interface due to the inherent nature of the chemistry. Methods that utilize the ligand shell as part of the interface to the electrode will likely be limited to longer tethers since longer ligands are generally better at stabilizing the nanoparticle core.

The coverage of NPs on an electrode surface can influence the electrochemical properties as previously discussed making it desirable to have methods to control this variable. Assembly methods ultimately rely on the efficacy of ligand exchange with a surface bound ligand which is not always controllable. Some control over the coverage can be achieved by forming a mixed monolayer of a NP binding ligand and an inert, diluent ligand.[50] The use of efficient coupling chemistry like azide/alkyne "click"

chemistry or directly binding nanoparticles to electrodes can make varying the coverage as a function of reaction time more reliable.[38,63]

In many cases, it is desirable to be able to modify the NP surface after it is interfaced to an electrode to create new structures or compositions that would be challenging to synthesize otherwise. The addition of metals to a nanoparticle surface through methods such as underpotential deposition (UPD) which are typically selective for metallic surfaces such as noble metals, is a useful post-fabrication modification to create multimetallic NP compositions (Figure 2.6a).[83,84] Since UPD can occur on metallic surfaces, the electrode must either be an inert material such as carbon or ITO, or it must be completely passivated. Similarly, for biological applications, the addition of biomolecules such as enzymes or proteins to NP surfaces is often done after the initial electrode fabrication (Figure 2.6b).[56] Similarly, the electrode material should be inert towards the binding chemistry used to attach the biomolecule to the NP surface for it to occur selectively. Finally, molecularly tethered multilayer nanoparticle structures are often desired to increase the overall surface area. These are typically constructed in a layer by layer approach where an initial monolayer of NP is attached to the electrode and then functionalized with a ligand that can facilitate an additional NP monolayer, and this process is continued iteratively (Figure 2.6a, b).[54,83] As with the previous modifications discussed, it is desirable that the binding chemistry used to form the nanoparticle multilayers is selective for the nanoparticle surface. For example, the use of dithiols to link multiple layers of AuNPs together while supported on a planar Au electrode could lead to complications unless the planar Au electrode is completely passivated. The ordering of the nanoparticles on the surface can also influence the quality of the resulting

multilayer structures. It is known that longer chain SAMs on metallic electrodes are more dense and ordered than monolayers formed through grafting methods.[70] The uniformity and density of the initial monolayer should be considered when looking to create nanoparticle multilayer structures.

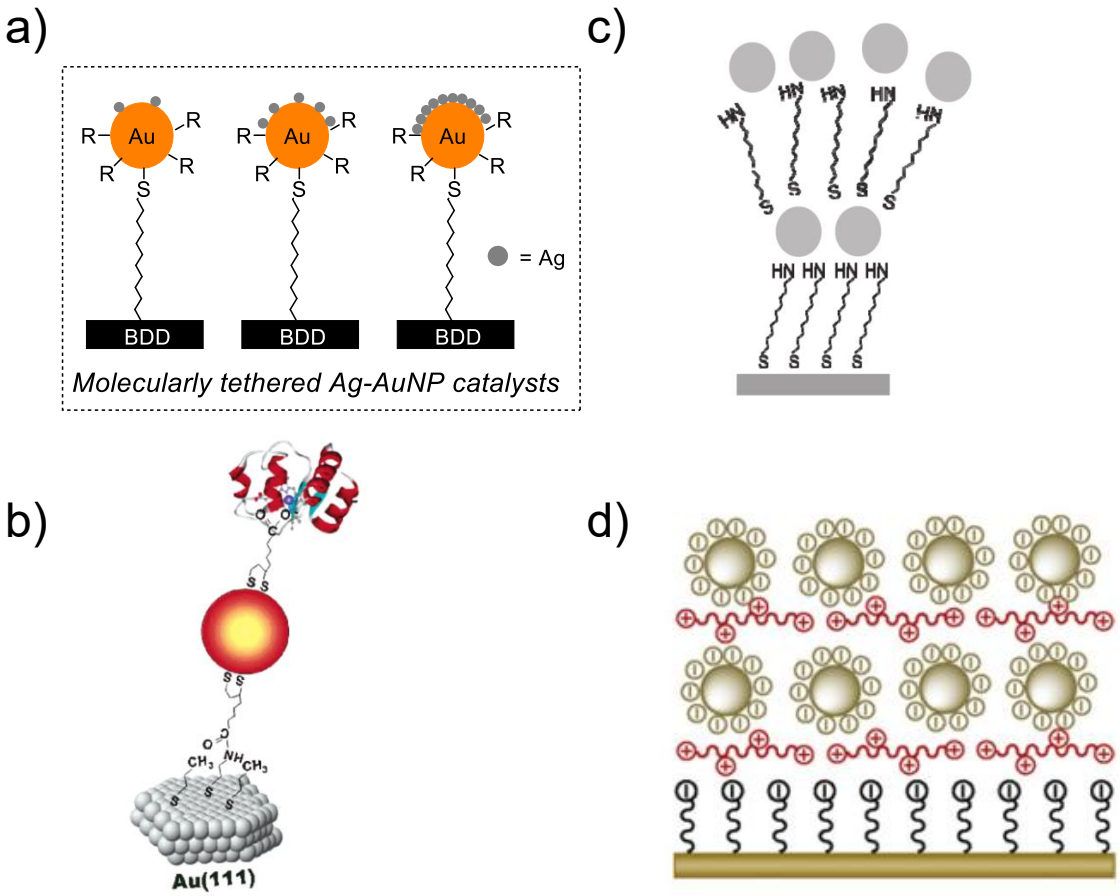

Figure 2.6. Depictions of post-fabrication manipulation of the NP-electrode structure and composition. Post-modification of tethered AuNPs with silver (a). Schematic illustration of the molecular assembly of cyt *c*-NP hybrid structure on the Au(111) surface (b). NP-multilayer architectures through layer-by-layer assembly with SAMs (c) and polyelectrolytes (d). Adapted from refs 84, 56, 7, and 28.

Bridge to Chapter III

Chapter II reviewed existing methods to fabricate NP-functionalized electrodes that are used for many applications. From this literature survey, it was clear that methods

to interface small nanoparticle electrocatalysts to inert electrodes through molecular linkers were still lacking. In order to pursue future studies of small NP electrocatalysts, these existing methods needed to be improved. Chapter III describes the development of a new approach to bind small gold nanoparticles to catalytically inert, boron doped diamond electrodes through molecular linkers. The electron transfer between the molecularly tethered nanoparticle and the electrode was characterized using a redox probe bound to the nanoparticle surface and was compared to nanoparticle-functionalized electrodes fabricated using solution deposition methods. The enhanced electrochemical behavior of the molecularly interfaced NPs highlights the significant influence of the interface on NP-mediated electron transfer and suggests that similar modified electrodes can serve as versatile platforms for studies of the electrocatalytic properties of nanoparticles.

CHAPTER III

SMALL GOLD NANOPARTICLES INTERFACED TO ELECTRODES THROUGH MOLECULAR LINKERS: A PLATFORM TO ENHANCE ELECTRON TRANSFER AND INCREASE ELECTROCHEMICALLY ACTIVE SURFACE AREA

Introduction

Nanoparticles (NPs) have been employed in a wide range of applications including sensing,[1,2] energy storage and conversion,[3,4] catalysis,[5] and electrochemical applications[6] due to their core size dependent properties and high surface area to volume ratio. NPs can impart chemical reactivity to otherwise inert, but abundant, materials and dramatically increase the surface area available for chemical transformations while minimizing the use of the active, often precious, metals.[7–9]

Nanoparticle-functionalized electrodes have been studied for electrochemical applications such as amperometric sensing,[10,11] photocatalysis,[12] and electrocatalysis.[4,13] In electrochemical applications, the addition of nanoparticles to an electrode surface enhances the electrode's catalytic activity[4,6] and can promote electron transfer through otherwise insulating molecules.[14,15] The enhanced electrochemical properties of NP-

functionalized electrodes have been attributed to the NP's electronic structure,[16] surface chemistry,[17] crystal facets,[18–21] density on the electrode surface,[22,23] as well as the interface between the NP and the electrode support.[24–27]

A number of studies have attempted to correlate the electrochemical properties of NP-functionalized electrodes with nanoparticle composition and structure.[13,16,18,28–30] Nanostructures deposited by vacuum evaporation or electrodeposition,[31–33] and their interfaces with the electrode, are difficult to characterize, making it challenging to attribute observed electrochemical properties to specific structures. Such deposition methods also make it hard to control the resulting NP core size distribution or coverage on the electrode. In order to understand the electrochemical properties of specific nanoparticle structures, it is necessary to fabricate NP-functionalized electrodes with uniform NP core sizes, known surface chemistry, and a defined interface between the NP and the electrode support.

The solution deposition of preformed nanoparticles is an alternative strategy to fabricate NP-functionalized electrodes that allows for more rigorous characterization of the NPs since solution-state characterization techniques are available in addition to solid-state techniques.[34] Further, bonding such NPs to an electrode might be useful to control the NP-electrode interface. Several methods to deposit (or attach) ligand-stabilized NPs on electrode materials are presented in Scheme 3.1. The simplest approaches involve solution deposition techniques (e.g., drop-casting, spin-coating, dip-coating) to modify the electrode surface with preformed NPs, or mixing nanoparticles with a support material (i.e. carbon black) which is then fabricated into an electrode.[18,28] While these methods are admittedly convenient, there are several drawbacks making it difficult to

directly relate NP morphology to observed electrochemical behavior. Solution deposition methods offer limited control of the NP surface coverage, the NP-electrode interface and/or interactions between the NPs, all of which influence electrochemical properties. NP coverage and attachment on electrodes prepared through solution deposition methods can also be sensitive to surface pretreatment steps and/or NP desorption may occur over time.[6]

To preserve the core size of preformed nanoparticles during deposition, a stabilizing ligand shell is required, typically composed of electrically insulating ligands. This can pose a barrier to electron transfer throughout the NP-functionalized electrode if efforts are not made to provide an electron-tunneling pathway. Two common ways to enhance electron transfer are to form bonds between the ligands and electrode surface or other NPs in the film, or to remove the ligands through thermal or chemical treatments. Such treatments can result in growth or destabilization of the NP core.[35–37]

A strategy to improve the NP-electrode interface while retaining NP morphology is to attach NPs to an electrode via a molecular monolayer, as shown in Scheme 3.1. These approaches provide a molecular interface between the NP and the electrode material and allow for more control over interactions between NPs while retaining the core size control offered by use of preformed NPs. It has been shown that electron transfer from a redox probe to an electrode through a NP-molecular monolayer-electrode assembly only occurs if the NP is bound to the monolayer through electrostatic or covalent interactions.[38] Proximity to the surface alone does not seem sufficient to promote NP-mediated electron transfer. Two covalent attachment strategies are shown in Scheme 3.1. In the first, the NP ligand shell is used to graft the NP directly to the

electrode through a functional group known to interact strongly with the electrode material (denoted X in Scheme 3.1). In the second case, NPs can be assembled onto chemically modified electrodes through ligand exchange with a functional group known to bind to the NP surface (denoted Y in Scheme 3.1). Each approach results in a defined interface for efficient electron transfer and should prevent NP desorption from the electrode surface compared to NPs that are non-specifically adsorbed.

Scheme 3.1. Methods of attaching preformed, ligand-stabilized nanoparticles to electrode substrates.

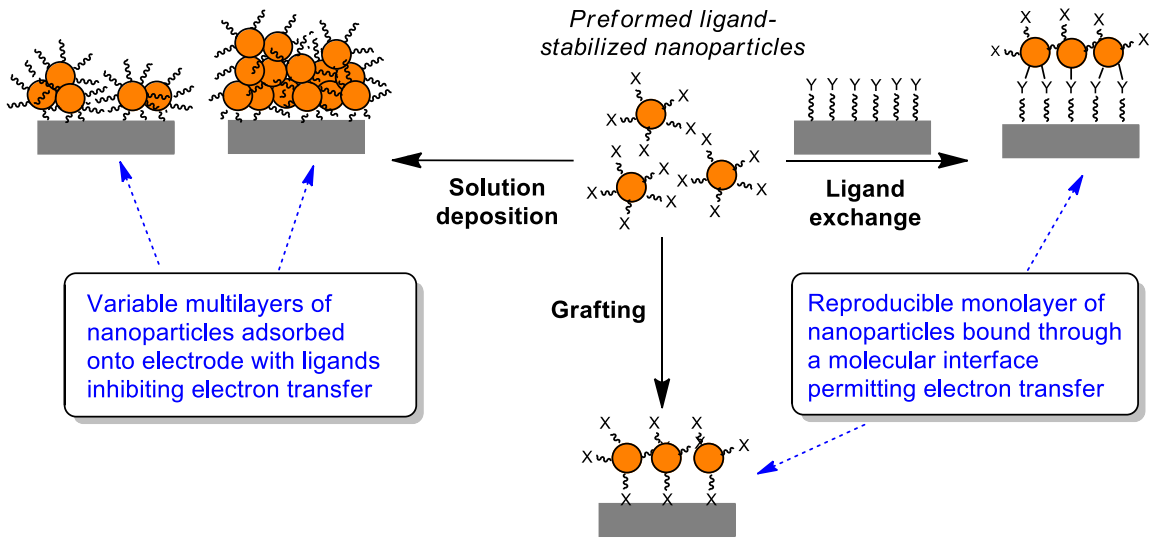

The assembly of nanoparticles onto a molecular monolayer has been demonstrated for larger (d_{core} >10 nm) citrate-stabilized AuNPs. These AuNPs have been assembled on molecular monolayers on planar Au,[15,38–40] glassy carbon,[14,41,42] silicon,[43] and boron doped diamond.[44,45] However, the AuNP attachment chemistry can be sensitive to pH (e.g., AuNPs assembled through Au-amine bonds) and have limited electrochemical windows (e.g., thiol monolayer desorption from planar Au at cathodic potentials in alkaline conditions [46,47]). In some cases, the electrode supports are unstable in aqueous electrolytes (e.g., silicon) limiting their general use in electrochemical

applications. The use of gold electrodes makes it difficult to characterize AuNPs and to distinguish the electrochemical properties of the AuNP from those of unpassivated areas of the electrode. Some methods used to functionalize other electrode supports, particularly for carbon electrodes, yield linkers of non-uniform thicknesses[14,48] or are influenced by variable microstructure,[49] leading to uncertainty about the NP-electrode interface and irreproducible electrochemical responses. The challenges in controlling the NP-electrode interface, as well as the limited stability of these systems under electrochemical conditions, mean that these platforms are not ideal for general electrochemical study of NPs, particularly small NPs that are already more challenging to characterize.

Small NPs (d_{core} < 2.5 nm) are reported to have unique electronic and catalytic properties due to their size and their number of under-coordinated surface atoms.[16,28,50] Small changes in NP size and surface chemistry in this regime can significantly affect these properties,[51] warranting the further investigation of NPs of uniform size, well-established surface chemistry, and a defined interface between the NP and the electrode. One of the few existing electrochemical studies of small NPs bound to an electrode by a molecular monolayer was reported by Hicks et al.[52] They adhered small AuNPs (d_{core} = 1.6 nm), stabilized by a mixed hexanethiolate/mercaptoundecanoic acid ligand shell, to a planar Au electrode through Zn^{2+}/carboxylate bridges. In order to further understanding of NP-mediated electron transfer and electrocatalytic properties of NPs in this small size regime, a robust, versatile platform that allows for small, uniform NPs to be attached to an electrode through molecular monolayers is needed.

Herein, two approaches to interface small AuNPs (d_{core} < 2.5 nm) to boron doped diamond (BDD) electrodes through molecular linkers have been developed and the electrochemical properties of the assemblies compared. Boron doped diamond was selected as the electrode material because it is relatively inert, has a wide electrochemical window and can be used to generate defined NP-electrode interfaces through photochemical grafting of alkenes to its surface.[53] In one approach, AuNPs are directly grafted to the electrode surface using the NP ligand shell as the covalently bound molecular linker. A second approach involves ligand exchange to link AuNPs to a molecular monolayer covalently bound to the electrode surface. The efficiency of the NP attachment chemistry was studied, showing that both methods yield monolayer coverage and that NP core size is not affected during the grafting and assembly processes. AuNPs with different core sizes and ligand shells were successfully assembled demonstrating the versatility of the platform. Using a redox probe tethered to the NP surface, the electrochemical properties of the different molecularly tethered AuNP systems were compared to one another and to those prepared by drop-casting AuNP films and depositing a AuNP monolayer formed at the air-water interface.

Experimental

Materials and characterization. Water (18.2 MΩ·cm) was obtained from a Barnstead Nanopure Diamond system. Chloroform was filtered through basic alumina before use with nanoparticles to remove any acidic impurities. All other reagents were used as received without further purification. Hydrogen tetrachloroaurate was obtained from Strem Chemicals. S-(10-undecenyl)-1-thioacetate was received from Sigma

Aldrich. Electrochemical grade free-standing boron doped diamond (BDD) substrates (Element Six, 1 cm x 1 cm) were used for all experiments.

Nuclear magnetic resonance spectroscopy (^{1}H NMR) spectra were collected on a Varian Inova 300 MHz NMR to verify material purity. Ultraviolet-visible spectroscopy (UV-Vis) spectra were collected using an Ocean Optics USB2000 spectrometer and samples were measured in a quartz cuvette (1 cm path length). Small angle x-ray scattering (SAXS) patterns were collected on an Anton Paar SAXSess mc^2 instrument operating in line collimation mode. The samples were measured in an epoxy sealed quartz capillary (Charles Supper) and were exposed to a monochromated x-ray source (Cu Kα, 1.54Å) operating at 40 kV and 50 mA. Data were collected by averaging 50 scans of 5-20 second exposures. Scattered x-ray intensity was measured with a charge-coupled device (CCD) detector (Roper Scientific). Data were desmeared using the Anton Paar SAXSquant software to produce scattering patterns and were imported into the Irena macro within IGOR Pro for modeling.[54] Models were fit to the scattering patterns using a Gaussian distribution, spherical form factor, and a dilute structure factor to determine the core size distribution of the AuNPs. All reported size distributions came from the Modeling II macro within Irena. Transmission electron microscopy (TEM) images were acquired on a FEI Titan 80-300 TEM. Samples were prepared by drop-casting a dilute solution of the nanoparticles on a lacey carbon coated copper TEM grid (Ted Pella).

X-ray photoelectron spectroscopy (XPS) was performed on a ThermoScientific ESCALAB 250 X-ray Photoelectron Spectrometer using an Al Kα monochromated source (150 W, 20 eV pass energy, 500 μm spot size). The spectra were analyzed using a Smart background and were calibrated to the C1s hydrocarbon peak (284.8 eV). Peak

fitting was done using ThermoScientific Avantage 4.75 software. Scanning electron microscopy (SEM) images were collected on a Zeiss Ultra-55 Scanning Electron Microscope using a secondary electron detector at an accelerating voltage of 25 kV.

Cyclic voltammograms were collected using a BAS 100B Electrochemical Analyzer (Bioanalytical Systems). Ag|AgCl (3 M NaCl) reference electrodes and a platinum wire auxiliary electrode (Bioanalytical Systems) were used for all measurements. The geometric surface area of the working electrode was defined using a Viton o-ring (0.6 cm inner diameter) in a custom glass electrochemical cell. Electrical contact to the BDD electrodes was made through a back contact with silver paint and copper wire.

Synthesis and characterization of gold nanoparticles. Undecenethiolate-stabilized gold nanoparticles (UDT-AuNPs) were synthesized following a modified two-phase Brust preparation.[55] $Au_{101}(PPh_3)_{21}Cl_5$ (TPP-Au_{101}) and $Au_{11}(PPh_3)_8Cl_3$ (TPP-Au_{11}) were synthesized using previously reported methods.[51,56] Nanoparticles were characterized using ^{1}H NMR, UV-Vis spectroscopy, SAXS, and TEM.

Direct functionalization of boron doped diamond with UDT-AuNPs. Boron doped diamond (BDD) substrates were cleaned with aqua regia and piranha solution before hydrogen termination. Hydrogen termination, which was necessary for photochemical grafting, was performed in a tube furnace with flowing H_2 in a quartz tube under conditions reported to produce hydrogen terminated diamond surfaces.[57] The BDD was heated to 850° C and held at that temperature for 20 minutes before cooling back down to room temperature under H_2. Contact angle goniometry was used to verify that the thermal treatment effectively hydrogen terminated the BDD surface. The contact

angle increased from 40° to 70° after hydrogen termination, indicating an increased hydrophobicity of the BDD. The sharpening of the peak at 284.8 eV in the x-ray photoelectron spectroscopy (XPS) C1s spectrum, attributed to C-H bonds, and the disappearance of the oxidized carbon shoulder at ~288.6 eV indicated that the BDD was successfully hydrogen terminated (Figure A1).

The procedure for photochemical grafting was adapted from Hamers and co-workers.[53,58] To graft the UDT-AuNPs to BDD (**Graft-UDT-AuNP**), a solution of UDT-AuNPs in heptane was sparged with argon to remove oxygen. The concentration of the nanoparticle solution, measured using the absorbance of the solution at 500 nm, was ~0.2 absorbance units. A hydrogen terminated BDD substrate was submerged in ~1 mL of the nanoparticle solution in a 10 mL beaker and irradiated through a quartz window with a UVP UVGL-58 Handheld UV lamp (254 nm, ~1 mW/cm^2) for 7 hours in an argon filled chamber. Photochemical grafting was performed in an argon filled chamber to minimize ozone generation during irradiation. The substrate was rinsed extensively with dichloromethane and hexanes to yield the UDT-AuNP-functionalized BDD substrate (**Graft-UDT-AuNP)**.

Assembly of triphenylphosphine gold nanoparticles onto undecyl thioacetate modified BDD (UDTA-BDD).

Functionalization of boron doped diamond using S-10-(undecenyl) thioacetate. An undecyl thioacetate monolayer was formed on BDD by photochemically grafting S-10-(undecenyl) thioacetate to BDD using a procedure adapted from Hamers and co-workers.[53,58] Neat S-10-(undecenyl) thioacetate (~2 μL) was placed on a hydrogen terminated BDD substrate and sandwiched between a quartz slide to produce a film on

the BDD substrate. This sample was irradiated at 254 nm for 5 hours under argon in a Novascan PSD Pro Series Digital UV Ozone System. The substrate was removed and sonicated in 30 mL chloroform (2x 5 min) followed by sonication in toluene (2x 5 min) to remove any physiadsorbed thioacetate to yield **UDTA-BDD**.

*Assembly of TPP-Au_{101} on UDTA-BDD (**TPP-Au_{101}-UDT**).* **UDTA-BDD** was submerged in a solution of TPP-Au_{101} in tetrahydrofuran (0.1 mg/mL). The solution was sparged with N_2 and kept under N_2 overnight to assemble the nanoparticles on the monolayer through ligand exchange. The sample was removed and vigorously shaken in dichloromethane for one minute (3x) to remove physiadsorbed TPP-Au_{101} and $AuClPPh_3$ from the ligand exchange.

*Assembly of TPP-Au_{11} on undecanethiol-functionalized BDD (**TPP-Au_{11}-UDT**).* Before assembly of TPP-Au_{11}, the thioacetate group on **UDTA-BDD** was deprotected to yield a thiol-functionalized surface. A mixture of K_2CO_3 (0.3 g, 2.2 mmol) in N_2-sparged methanol (20 mL) was stirred for 10 minutes. **UDTA-BDD** was submerged in the mixture for 2 hours and kept under N_2 to prevent disulfide formation. HCl (10 mL, 0.2 M, N_2 sparged) was then added to the mixture to yield the deprotected undecanethiol-functionalized BDD (**UDT-BDD). UDT-BDD** was removed and rinsed with dichloromethane. **UDT-BDD** was then submerged in a solution of N_2-sparged TPP-Au_{11} in basic chloroform (0.1 mg/mL). The solution was heated to 55°C under N_2 and left to react overnight, conditions that have previously been used for ligand exchange of TPP-Au_{11}.[59] The sample was removed and vigorously rinsed in dichloromethane for one minute (3x) to remove physiadsorbed TPP-Au_{11} and free triphenylphosphine ligand from the ligand exchange.

Binding the redox probe 6-ferrocenyl(carbonyloxy)hexanethiol ($FcCO_2HT$) to the AuNP surface. The redox probe 6-ferrocenyl(carbonyloxy)hexanethiol ($FcCO_2HT$) was synthesized based on a method previously reported (details in the supporting information).[60] The **Graft-UDT-AuNP** electrodes were treated with ozone (50 ppm in N_2) for five minutes, followed by a ten minute soak in H_2O. This treatment is known to remove a portion of the thiolate ligand shell.[61] The sample was soaked in 1 mM $FcCO_2HT$ (in dichloromethane) to assemble the redox probe on the open sites on the NP, followed by extensive rinses with dichloromethane and acetonitrile to remove non-specifically bound $FcCO_2HT$ from the surface. The **TPP-Au$_x$-UDT** samples were soaked in 1 mM $FcCO_2HT$ (in dichloromethane) to exchange some of the triphenylphosphine ligands for $FcCO_2HT$, followed by extensive rinses with dichloromethane to remove any unbound $FcCO_2HT$.

Deposition of monolayer films of AuNPs formed by self-assembly at the air-water interface onto BDD. A 10 mL beaker was filled with H_2O and the water surface was coated with a solution of NPs dispersed in dichloromethane. Once the dichloromethane had evaporated, the resulting monolayer of NPs was transferred to a bare BDD electrode by placing the BDD substrate on top of the NP monolayer at the air-water interface.

Results and Discussion

The aim of this study was to evaluate the electrochemical properties of small, uniform ligand-stabilized AuNPs at a molecularly defined electrode interface and to evaluate the role of the interface and core size on those properties. A NP-functionalized electrode possessing a monolayer of evenly distributed NPs bound through a well-defined

interface that also retain their initial core size once assembled on the surface was required for this study. Boron doped diamond (BDD) was chosen as an electrode support because it is a robust material that is electrically conductive, stable in most common electrolytes, relatively inert towards most electrocatalytic transformations, and has a wide electrochemical window.[62] Furthermore, molecular monolayers can be generated through the photochemical grafting of alkenes to form covalent C-C bonds between the BDD and the grafted molecule.[53,58] Small ligand-stabilized AuNPs (d_{core} < 2.5 nm) were chosen as a model system to assemble due to their interesting electronic and catalytic properties and since well-established synthetic methods that afford both a narrow core size distribution and defined surface chemistry exist.

Scheme 3.2 outlines two routes used to obtain AuNPs bound through an undecanethiolate tether to a hydrogen terminated BDD substrate. In Route 1, preformed undecenethiolate AuNPs (UDT-AuNPs) are covalently attached to the BDD through direct photochemical grafting of their ligand shell to the substrate (**Graft-UDT-AuNP**). This is a direct, single-step approach to attach synthetically accessible and stable alkene-modified AuNPs. In Route 2, two different core sizes of preformed triphenylphosphine-stabilized AuNPs (d_{core} = 0.8 nm and 1.9 nm) are assembled via ligand exchange onto an undecyl thioacetate-functionalized molecular monolayer covalently bound to BDD (**UDTA-BDD**). The thioacetate protecting group prevents disulfide formation and other undesired thiol-alkene reactions during the initial photochemical grafting of the linker to the substrate. The thioacetate group is easily deprotected to the free thiol prior to AuNP assembly, if needed. Triphenylphosphine-stabilized AuNPs were used since they are known to readily undergo ligand exchange reactions with thiols.[59,63,64] An undecyl

thioacetate monolayer was used to maintain a constant linker length across all three systems studied, allowing for direct comparisons to be made. The assembly approach provides a method when shorter molecular linkers are desired, and/or when NPs of a desired core material/size cannot be synthesized with terminal alkenes in their ligand shell.

Scheme 3.2. Two strategies to prepare AuNP-functionalized electrodes with a molecular nanoparticle-electrode interface.

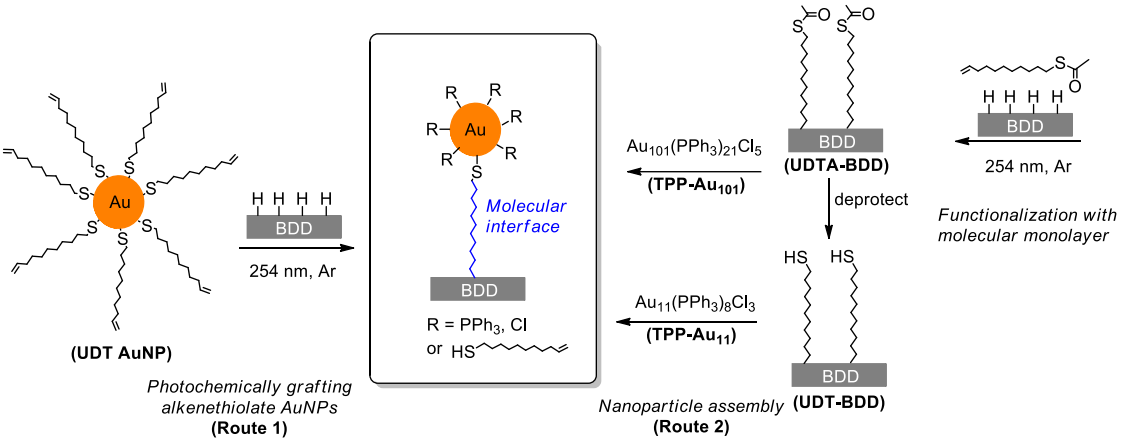

Synthesis and characterization of ligand-stabilized AuNPs for attachment.

Undecenethiolate-stabilized AuNPs (UDT-AuNPs) were synthesized as previously reported and purified by sequential precipitations.[55] ^{1}H NMR verified that purification removed any free ligand or phase transfer catalyst (Figure A2). The UDT-AuNPs were found to be 2.1 ± 0.1 nm by small angle x-ray scattering (SAXS) and transmission electron microscopy (TEM) (Figure A3). The absence of a plasmon peak in the UV-Vis spectrum is consistent with this size (Figure A4).

Two types of triphenylphosphine-stabilized AuNPs (TPP-Au_x) were synthesized for use in ligand exchange reactions with the molecular monolayer. $Au_{101}(PPh_3)_{21}Cl_5$ (TPP-Au_{101}) was synthesized as previously reported.[56] The core size of TPP-Au_{101} was

determined to be 1.9 ± 0.5 nm by SAXS, and was corroborated by TEM and UV-Vis (Figure A5, A6). $Au_{11}(PPh_3)_8Cl_3$ (TPP-Au_{11}) was synthesized by reduction of $AuClPPh_3$ with $NaBH_4$.[51] ^1H NMR and UV-Vis of TPP-Au_{11} confirmed that only $Au_{11}(PPh_3)_8Cl_3$ was synthesized and not a mixture of $Au_{11}(PPh_3)_8Cl_3$ and the less stable form $Au_{11}(PPh_3)_7Cl_3$ (Figure A7, A8).[51] The core size of TPP-Au_{11} was determined to be 0.8 ± 0.2 nm by TEM (N = 530) (Figure A8).

Building the AuNP-molecular monolayer-BDD platform.

*Route 1: Photochemically grafting undecenethiolate AuNPs to BDD (**Graft-UDT-AuNP**).* UDT-AuNPs were grafted to BDD upon irradiation of BDD in a dilute heptane solution of UDT-AuNPs at 254 nm under argon. X-ray photoelectron spectroscopy (XPS) of **Graft-UDT-AuNP** was performed to determine if the UDT-AuNPs were altered by the grafting process (Figure A9). The elemental $Au_{84.5}$:$S_{162.5}$ ratio was used to compare the thiolate ligand shell before and after the grafting process, since 162.5 eV is the characteristic binding energy of a thiol. There was minimal change in the $Au_{84.5}$:$S_{162.5}$ ratio when the UDT-AuNPs are grafted versus when they were simply drop-cast onto a BDD substrate (Table 3.1) indicating the integrity of the ligand shell of the UDT-AuNPs is maintained throughout the grafting process. The difference in $Au_{84.5}$:$S_{162.5}$ ratios between the two samples can be explained by ozone generated in the grafting chamber from trace oxygen resulting in the oxidation of a small amount of the thiolate ligands in the **Graft-UDT-AuNP** sample.

A control experiment was performed to assess if the XPS Au4f signal was due to grafting UDT-AuNPs or simply AuNP physiadsorption to the BDD surface. A bare BDD substrate was treated in the same way as the **Graft-UDT-AuNP** samples except that it

was not irradiated by 254 nm light. The $Au_{84.5}$:$C_{284.8}$ ratio obtained via XPS was used to compare AuNP surface coverage over the BDD substrate. The $Au_{84.5}$:$C_{284.8}$ ratio underestimates the true coverage since the C1s peak at 284.8 eV originates from both the BDD substrate as well as the alkenethiolate ligand shell. The **Graft-UDT-AuNP** sample has roughly an order of magnitude higher $Au_{84.5}$:$C_{284.8}$ ratio compared to the sample that was not irradiated (Table 3.1). This suggests that the majority of the Au4f XPS signal is not a result of physiadsorbed AuNPs, and that the UDT-AuNPs were successfully grafted to BDD.

Table 3.1. Comparison of elemental ratios of UDT-AuNPs on BDD by XPS

Sample	$Au_{84.5}:S_{162.5}$	$Au_{84.5}:C_{284.8}$
Drop-cast sample [a]	2.9 ± 0.1 [b]	-
Graft-UDT-AuNP	3.4 ± 0.2 [b]	0.12 ± 0.02 [b]
Control sample, no UV [c]	3.3 ± 0.1 [d]	0.020 ± 0.002 [d]

[a] Sample prepared by drop-casting UDT-AuNPs onto BDD substrate
[b] Average of two samples, three spots analyzed per sample
[c] Sample exposed to all grafting conditions except irradiation by 254 nm light
[d] Average of three spots on one sample

Route 2: TPP-Au_x NP assembly onto undecanethiolate monolayers on BDD.

Before AuNP assembly, an undecyl thioacetate molecular monolayer was grafted to BDD

by irradiation at 254 nm under argon to produce **UDTA-BDD** as shown in Scheme 3.2. XPS was used to evaluate the efficacy of the photochemical grafting method in forming an undecyl thioacetate monolayer on BDD. The S2p region of the XPS of **UDTA-BDD** showed a peak at 164.2 eV, characteristic of a thioacetate group (Figure A10). A control experiment was performed where a hydrogen terminated BDD (H-BDD) substrate was exposed to 10-undecene-1-thioacetate in the dark. The grafted **UDTA-BDD** and the control sample were compared with XPS using the $S_{164.2}$:$C_{284.8}$ elemental ratios as a metric to evaluate the extent of thioacetate grafting. The grafted thioacetate yielded a $S_{164.2}$:$C_{284.8}$ ratio of 0.023 ± 0.007 (determined from averaging four samples) while the control sample only had a $S_{164.2}$:$C_{284.8}$ ratio of 0.002. This verifies the efficacy of the photochemical grafting and confirms that the thioacetate signal observed in **UDTA-BDD** is due primarily to grafting, not physiadsorption to the BDD surface. Cyclic voltammetry was used to assess the extent of BDD passivation. The **UDTA-BDD** electrode showed an 87% decrease in capacitive current and significant suppression of oxygen reduction current compared to the H-BDD electrode (Figure A11).

Ligand exchange reactions were used to tether TPP-Au_{101} to **UDTA-BDD**. The $Au_{84.5}$:$C_{284.8}$ elemental ratios from XPS were used to compare AuNP surface coverage between samples. When **UDTA-BDD** was exposed to TPP-Au_{101}, XPS yielded a $Au_{84.5}$:$C_{284.8}$ ratio of 0.15 ± 0.07 whereas a bare BDD substrate exposed to TPP-Au_{101} yielded a $Au_{84.5}$:$C_{284.8}$ ratio of 0.05 ± 0.01. In addition, XPS provided evidence that TPP-Au_{101} is assembled on **UDTA-BDD** through Au-thiolate bonds from the appearance of a new peak in the S2p spectrum at a lower binding energy, ~162.8 eV, indicative of a Au-thiolate bond (Figure A12). In addition to the presence of the thiolate bond, a P2p peak

at 131.2 eV and Cl2p peak at 197.8 eV are also present, indicating that the portion of the TPP-Au_{101} ligand shell that does not undergo ligand exchange remains intact throughout the assembly process (Figure A12).

TPP-Au_{11} could also be assembled on BDD through undecanethiolate linkers, but first required deprotection of the terminal thioacetate in **UDTA-BDD** to yield a surface rich in thiol groups (**UDT-BDD)**. When **UDT-BDD** was exposed to TPP-Au_{11}, XPS yielded a $Au_{84.5}$:$C_{284.8}$ ratio of 0.10 ± 0.06 while a bare BDD substrate exposed to TPP-Au_{11} yielded a $Au_{84.5}$:$C_{284.8}$ ratio of 0.005 ± 0.001. The characteristic peak for a Au-thiolate bond also appeared in the XPS S2p spectrum which suggests that TPP-Au_{11} is bound to the molecular monolayer surface through Au-thiolate bonds (Figure A13). The ability of the system to assemble both TPP-Au_{101} and TPP-Au_{11} exemplifies its versatility.

Assessing surface coverage of AuNPs on BDD. While $Au_{84.5}$:$C_{284.8}$ ratios from XPS provided a means of comparing the Au surface coverage between samples, a method was needed to determine NP surface coverage more directly. Figure 3.1a,b shows scanning electron microscope (SEM) images of **Graft-UDT-AuNP** and **TPP-Au_{101}-UDT** samples showing even AuNP coverage with no signs of NP aggregation. In comparison, the bare BDD and **UDTA-BDD** show no features in this size range at the same magnification (Figure 3.1c,d). Due to the small size of the AuNPs, the SEM is near its resolution limit, preventing quantitative size analysis of the AuNPs, however it is still possible to estimate the coverage of nanoparticles from these images. The coverage of AuNPs obtained via molecular tethering is estimated to be ~10^{11} NPs/cm^2 for both the **Graft-UDT-AuNP** and **TPP-Au_{101}-UDT** samples, determined by counting NPs on the

SEM images. Using the NP core diameter and ligand shell contribution to determine the NP area, and assuming the NPs are monodisperse and the BDD is flat, the theoretical coverage of a hexagonally close packed monolayer was calculated. The tethered samples yield approximately 10% NP coverage relative to a theoretical monolayer of NPs. For comparison, other methods reported to assemble monolayers of ~ l3 nm citrate-stabilized AuNPs on planar supports through molecular tethers resulted in ~1-30% coverage of AuNPs relative to a theoretical monolayer of NPs.[38,44,45]

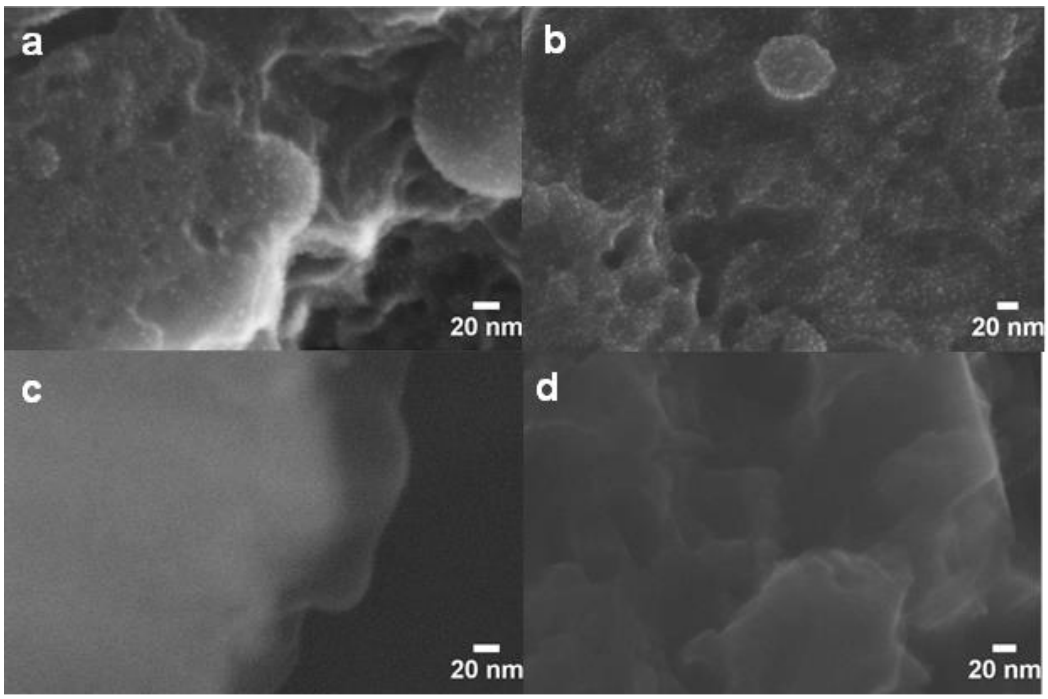

Figure 3.1. SEM images of a) **Graft-UDT-AuNP**, b) **TPP-Au$_{101}$-UDT,** c) a bare BDD substrate, and d) **UDTA-BDD.** The small, white features in a) and b) demonstrate the methods yield monolayer coverage of nanoparticles, and the absence of these features in c) and d) verify that these features are indeed nanoparticles and do not originate from the substrate.

Assessing nanoparticle-mediated electron transfer using a AuNP tethered redox probe. A small amount of a redox probe, 6-ferrocenyl(carbonyloxy)hexanethiol ($FcCO_2HT$), was introduced into the ligand shell of the AuNPs through Au-thiolate bonds to electrochemically evaluate the AuNP-UDT systems. A redox probe bound to the NP

surface was chosen to examine NP-mediated electron transfer instead of a redox probe in solution to minimize any direct electron transfer between the redox probe and the BDD electrode support. $FcCO_2HT$ was chosen because of its fast electron transfer, allowing for the electron transfer from the NP to the electrode to be directly observed.[40] In addition, the hydrophilic ester moiety prevents the ferrocene from burying itself in the hydrophobic alkane monolayer. This probe also facilitates the comparison of this platform to existing reports of planar Au self-assembled monolayers of ferrocene thiols.[60]

Two different methods were used to attach $FcCO_2HT$ to the AuNP surface for the **Graft-UDT-AuNP** samples and the **TPP-Au$_x$-UDT** samples. The **Graft-UDT-AuNP** sample was initially treated with dilute ozone to remove a portion of the thiolate ligand shell. The $FcCO_2HT$ probe was then introduced to replace the partially removed thiolate ligand shell. This method was used in lieu of a direct ligand exchange between the $FcCO_2HT$ and the undecenethiolate ligands because thiol for thiol ligand exchanges do not always readily occur, especially when trying to replace a longer chain ligand with a shorter ligand.[65] This dilute ozone treatment was previously shown not to cause NP growth or destabilization.[61] $FcCO_2HT$ was attached to **TPP-Au$_x$-UDT** samples through simple ligand exchange with the triphenylphosphine ligands.[59,63] Chart 3.1 depicts the two molecularly tethered AuNP systems with bound $FcCO_2HT$ redox probes.

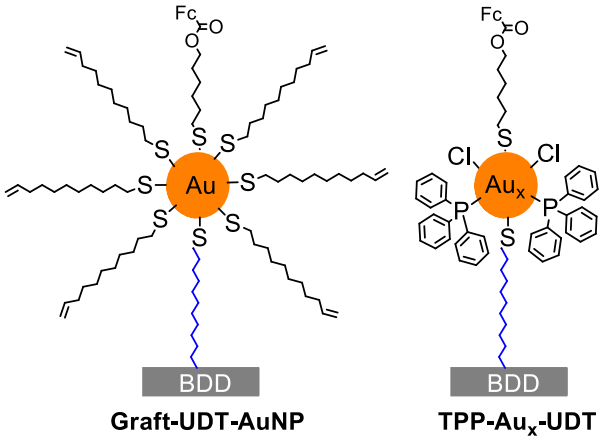

Chart 3.1. Molecularly tethered AuNP-functionalized boron doped diamond electrodes with bound ferrocene (Fc) redox probes.

Several control experiments were performed to ensure the measured current was from redox probe bound to the NP surface. To ensure the $FcCO_2HT$ signal was only from ferrocenes bound to the AuNPs (rather than directly to the BDD), a bare substrate was treated in the same manner used to attach $FcCO_2HT$ to the **Graft-UDT-AuNP** samples (Figure A14). No $FcCO_2HT$ signal was detected, indicating that $FcCO_2HT$ does not attach directly to the BDD surface. It was also possible in the **TPP-Au$_x$-UDT** systems that the $FcCO_2HT$ could form disulfide bonds with free terminal thioacetate or thiol functionalities in the molecular monolayer. To investigate this scenario, **UDTA-BDD**, **TPP-Au$_{101}$-UDT**, and **TPP-Au$_{11}$-UDT** were treated with known disulfide reducing agents (dithiothreitol or tris(2-carboxyethyl)phosphine (TCEP)) to reduce any disulfide bonds between the molecular monolayer and the redox probe (Figures A15, A16). A small reduction in faradaic current was observed, however, the peak potentials remained unchanged. Finally, to further confirm that the observed current only originated from probe bound to the NP, **Graft-UDT-AuNP** was treated with a 0.1 M KCN solution to decompose the AuNPs. Less than 10% of the initial $FcCO_2HT$ remained in the cyclic

voltammograms of the decomposed sample, suggesting that the majority of the current in the original **Graft-UDT-AuNP** sample is from NP-bound redox probe (Figure A17).

Effect of molecular tethering method and NP core size on electrochemical properties. Cyclic voltammetry (CV) was used to investigate the electrochemical properties of the $FcCO_2HT$-AuNP-UDT systems (Figure 3.2, top row). All three systems exhibit behavior of a reversible, surface bound redox probe where the peak current scales linearly with the scan rate (Figure A18), and are stable over many electrochemical cycles. Slightly different peak-to-peak separations (ΔE_p), full width at half maximum (FWHM), and $E^{0'}$ values were found for each system (Table 3.2). ΔE_p can be used to assess the barrier to electron transfer. For an ideal surface bound redox probe, the ΔE_p is 0 mV. The small $\Delta E_p \leq 41$ mV for all three $FcCO_2HT$-AuNP-UDT systems indicates the undecanethiolate molecular tether does not significantly inhibit electron transfer. The **Graft-UDT-AuNP** ($d_{core} = 2.1 \pm 0.1$ nm) and the **TPP-Au$_{101}$-UDT** ($d_{core} = 1.9 \pm 0.5$ nm) systems had ΔE_p values within 2 mV of each other, 30 mV and 28 mV respectively, while the smaller **TPP-Au$_{11}$-UDT** ($d_{core} = 0.8 \pm 0.2$ nm) system had a ΔE_p of 41 mV. The larger ΔE_p suggests the **TPP-Au$_{11}$-UDT** system experiences a greater barrier to electron transfer than the **Graft-UDT-AuNP** and **TPP-Au$_{101}$-UDT** samples. Chazalviel and Allongue theorized that the rate of NP-mediated electron transfer across a molecular monolayer is dependent on both molecular layer thickness and NP core size, with electron transfer being more hindered as NP size is decreased.[66] The similar ΔE_p values for the similarly sized AuNP systems and larger ΔE_p exhibited by the smaller, **TPP-Au$_{11}$-UDT** system is in agreement with Chazalviel's theoretical model. The FWHM for all three systems are near 90 mV, the ideal value for a surface bound redox couple. This

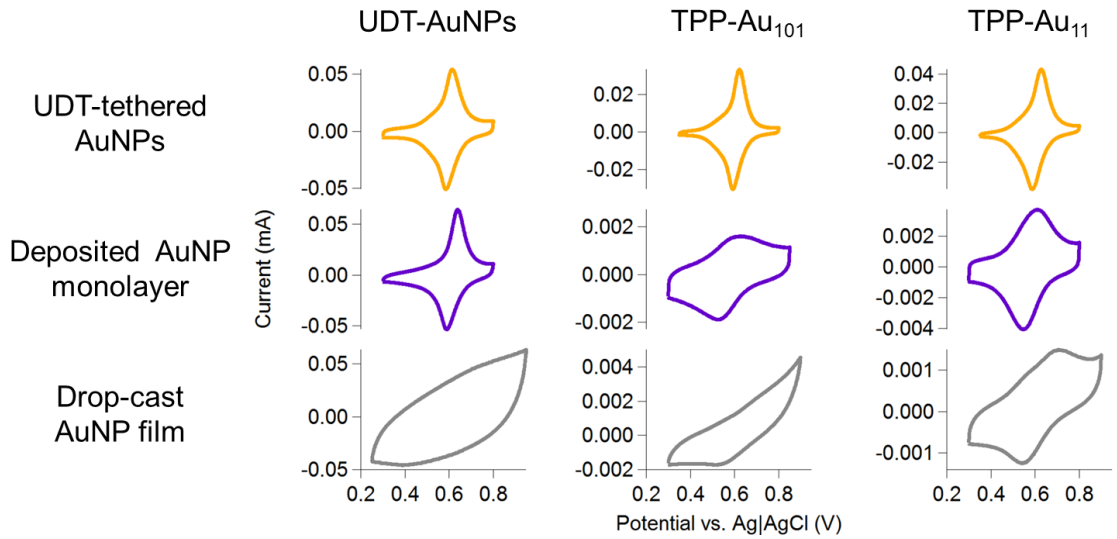

Figure 3.2. Comparison of cyclic voltammograms of the AuNP-BDD electrodes fabricated by different methods: binding a monolayer of AuNPs through an undecanethiolate monolayer (top row), depositing a AuNP monolayer film formed by self-assembly at the air-water interface (middle row), and drop-casting a AuNP film (bottom row). All samples were treated with $FcCO_2HT$. CVs were taken in 0.1 M $HClO_4$ at 100 mV/s.

suggests there are no major ferrocene-ferrocene interactions in the $FcCO_2HT$-AuNP-UDT systems as such interactions would broaden both the anodic and cathodic peaks. The narrow FWHM values also suggest that spatial inhomogeneity in electron transfer rates reported for BDD[67,68] do not significantly influence the results reported here. Lastly, both **TPP-Au$_x$-UDT** samples' $E^{0'}$ values were within 2 mV of each other while the **Graft-UDT-AuNP** system's $E^{0'}$ value was decreased by 6-8 mV. This could suggest that $E^{0'}$ is ligand shell dependent and not dependent on core size. The variance in electrochemical properties with changing NP size is evidence that the observed electron transfer is NP-mediated. Both molecular tethering routes yield almost identical electrochemical properties, where $E^{0'}$ is slightly affected by the ligand shell. Either route is suitable to fabricate a NP-functionalized electrode with a uniform monolayer of molecularly tethered NPs that exhibits reproducible electrochemical behavior.

Table 3.2. Electrochemical properties of the $FcCO_2HT$-AuNP-BDD electrodes

AuNP sample	*NP-attachment method*	*ΔE_p (mV)*	*FWHM (anodic) (mV)*	*$E^{0'}$ (mV)*	*Electrochemically active Au surface area (cm^2)*
UDT-AuNP					
	UDT-tethered	30	90	601	0.9 ± 0.3[c]
	Deposited monolayer	50	78	615	0.9
	Drop-cast	*N/A*[a]	*N/A*[a]	*N/A*[a]	1.2
TPP-Au_{101}					
	UDT-tethered	28	68	607	0.43 ± 0.03[c]
	Deposited monolayer	101	> 400	580	0.02
	Drop-cast	*N/A*[a]	*N/A*[a]	*N/A*[a]	*N/A*[b]
TPP-Au_{11}					
	UDT-tethered	41	84	609	0.5 ± 0.3[c]
	Deposited monolayer	65	170	580	0.01
	Drop-cast	168	> 300	627	0.02

[a] Unable to identify clear $FcCO_2HT$ signal
[b] Characteristic sharp Au oxide reduction peak not present
[c] Averaged over three samples

Although it is tempting to compare the $FcCO_2HT$-AuNP-UDT systems to analogous AuNP-SAM-electrode systems, most AuNP-SAM-electrode systems employ passivating monolayers and thus are able to use solution phase redox probes for electrochemical characterization. Since the molecular monolayers formed on boron doped diamond are not completely passivating,[69] the electrochemical response observed from a solution redox probe in the AuNP-UDT-BDD system arises from both AuNPs and the BDD substrate. Liu et al. reported a AuNP-SAM-electrode system studied with a tethered redox probe assembled AuNPs (d_{core} = 5-15 nm) on terminal thiol SAMs.[40] Although, they used a very fast scan rate, 50 V/s, preventing the comparison of ΔE_p

values due to its scan rate dependence, sample preparation and peak shapes can be compared. The 6-(ferrocenyl) hexanethiol probe they used was diluted 1:9 with 1-pentanethiol to prevent major ferrocene-ferrocene interactions. Even with their use of a diluent ligand, the CV has a prominent anodic shoulder indicating the ferrocene probe resides in different local environments. Similarly, Kondo et al. reported assembly of large AuNPs (~12 nm) on 3-mercaptopropyltrimethoxysilane linkers on boron doped diamond, also using bound 6-(ferrocenyl) hexanethiol to electrochemically evaluate their samples.[45] While they ran CVs in 0.1 M $NaHCO_3$, preventing direct comparison of $E^{0'}$ values, the FWHM values of their system were almost double compared to the $FcCO_2HT$-AuNP-UDT samples reported in this work. They also observed small ΔE_p values (~17 mV). The slightly smaller ΔE_p values in their system are likely a result of the larger AuNP core size and that their molecular linker is a third of the length of the undecanethiolate linkers used in this work, both of which have been reported to influence electron transfer.[38,66] The $FcCO_2HT$-AuNP-UDT systems do not require the use of a diluent ligand to achieve narrow redox peaks. This could be due to the uniform spacing of AuNPs across the BDD, allowing for each $FcCO_2HT$ molecule to reside in chemically equivalent environments.

Effect of NP attachment method on electrochemical properties: molecular tethering, deposition of a monolayer, and drop-casting. NPs tethered to electrodes through a molecular interface were compared to electrodes prepared by other solution deposition techniques. One simple method often used to prepare NP monolayers (or submonolayers) on electrodes is NP self-assembly at the air-water interface, followed by transfer of the NP monolayer to the electrode.[70–72] A AuNP monolayer was formed

through self-assembly at an air-water interface and then deposited on a BDD electrode. This sample was then treated with $FcCO_2HT$ to directly compare the effect of the molecular interface on the electrochemical properties (Figure 3.2, middle row). All three samples prepared through deposition of a AuNP monolayer to BDD had larger ΔE_p values than their respective UDT-tethered samples (Table 3.2). These larger values suggest that the barrier to electron transfer increases in the absence of a covalent molecular interface. For the TPP-Au_x samples, the fwhms were significantly broader than their tethered analogues, indicating that the environment of $FcCO_2HT$ is not uniform. The $E^{0'}$ for both TPP-Au_x samples prepared by deposition of the NP monolayer decreased to 580 mV while the UDT-AuNP $E^{0'}$ increased to 615 mV supporting the previous claim that redox potential is dependent on ligand shell. The broad redox peaks and subsequently ill-defined electrochemical properties of the physically adsorbed NP monolayer further demonstrate the necessity of strong interactions between the NP and the electrode to facilitate efficient electronic communication between the redox probe and electrode.

The electrochemical properties of molecularly tethered NPs were also compared to thicker, drop-cast NP samples. Drop-cast NP films were prepared from casting a solution of AuNPs in dichloromethane onto BDD resulting in ~2 mg of AuNPs on the BDD electrodes. Each sample was then treated with $FcCO_2HT$ for a direct comparison. CVs of drop-cast TPP-Au_{101} and the UDT-AuNPs showed no distinct $FcCO_2HT$ redox peaks while the drop-cast TPP-Au_{11} sample showed broad $FcCO_2HT$ redox peaks with a large ΔE_p of 170 mV (Figure 3.2, bottom row). There were significantly more AuNPs on the drop-cast samples than the samples prepared through NP grafting or assembly, thus a

much larger current response is expected if all of the NPs are available to perform electrochemistry. However, this is not observed in the CVs, presumably because only the NPs at the surface of the sample are accessible to the $FcCO_2HT$ probe and electrochemically. The ill-defined or absent $FcCO_2HT$ redox peaks for the drop-cast AuNP electrodes indicates an efficient electron transfer pathway is lacking between the redox probe and the electrode, either due to poor electrical contact between the NPs and the electrode or the physical distance between the $FcCO_2HT$-functionalized NPs and the electrode. Similar results were observed in previous work examining multi-layer films of ferrocenated AuNPs.[72] These results demonstrate that one cannot simply drop-cast thicker layers of ligand-stabilized NPs onto electrode substrates as a means of increasing NP loading, for applications such as electrocatalysis, since the NP-electrode interface greatly affects the electrochemical properties.

To compare the electrochemically active surface areas of these samples, the Au surface area was determined for each sample by integration of the gold oxide reduction peak at 0.9 V vs. Ag|AgCl in cyclic voltammograms (Figure A19).[73] For the molecularly tethered samples, the reduction peak did not disappear after multiple cycles, suggesting that the AuNPs are strongly tethered to the electrode. Additionally, the electrochemically active Au surface area of the TPP-Au_x deposited monolayer and drop-cast samples is an order of magnitude lower than their molecularly tethered analogues. This could indicate that the NPs are not as electrochemically accessible as the tethered NPs or that NP desorption occurs throughout the $FcCO_2HT$ treatment and/or electrochemical measurements. Although the differences in electrochemically active surface area between the systems are not fully understood, one possible reason a trend in surface area

was not observed for the UDT-AuNP samples could be due to their exposure to ozone to remove a portion of the thiolate ligand shell prior to $FcCO_2HT$ attachment. This ozone treatment leads to more electrochemically active sites which are not produced in the TPP-Au_x systems and may also explain the differences between the electrochemically active surface areas of **Graft-UDT-AuNP** and **TPP-Au_{101}-UDT,** despite similar NP coverage.

The clear differences between the deposited monolayer and the drop-cast samples demonstrated that the electrochemical properties of NP electrodes fabricated from solution deposition techniques are variable from sample to sample. Such variability is due to a lack of control over NP-NP interactions and the NP-electrode interface. In contrast, the molecularly tethered systems exhibit reproducible electrochemical properties. These results exemplify the importance of a defined interface when studying the electrochemical properties of NP-functionalized electrodes.

Conclusions

Two strategies were demonstrated for tethering small (d_{core} < 2.5 nm) ligand-stabilized AuNPs to a boron doped diamond electrode through a molecular interface. The NPs retain their composition, initial core size and shape throughout the process and yield uniform monolayer NP assemblies with ~10^{11} NPs/cm^2 coverage resulting from either method. Nanoparticle-mediated electron transfer through molecular monolayers was evaluated by attaching redox probes to the AuNP surfaces. The smaller **TPP-Au_{11}-UDT** system exhibits a greater barrier to electron transfer than the larger **Graft-UDT-AuNP** and **TPP-Au_{101}-UDT** systems as might be expected if the nanoparticle core size influences electron transfer as theorized by Chazaviel and Allongue.[66] In all cases, the molecular NP-electrode interface results in more efficient electron transfer than the two

solution deposited samples, and a greater proportion of the nanoparticles are electrochemically active when using a molecular tether. In contrast to samples produced by solution deposition methods where the electrochemical response depends strongly on the exact deposition conditions, the electrochemical properties of the molecularly tethered samples were reproducible across a number of preparations.

This molecular tethering strategy offers a versatile platform to interface nanoparticles with an otherwise inert electrode material. Because the platform yields samples with reproducible electrochemical responses, it provides the opportunity to quantitatively study NP-mediated electron transfer as a function of NP morphology and linker length. It also provides a system to study the influence of core size and the NP-electrode interface on the electrocatalytic behavior of preformed nanoparticles. Both will be the focus of future work with this platform. In addition, the platform should prove useful for grafting other nanomaterials stabilized by ligands possessing terminal alkenes or assembling other nanoparticle core materials onto an appropriate terminal functional group on the monolayer. This approach could be further expanded to attach nanoparticles to substrates other than BDD where alkenes can be photochemically grafted, such as silicon, SiO_2, TiO_2, and amorphous carbon.[74–77]

Bridge to Chapter IV

With a platform to interface small gold nanoparticles to electrodes in hand, the following chapter describes the use of this approach to examine small gold nanoparticles and clusters as electrocatalysts for the oxygen reduction reaction. Traditionally small nanoparticles and clusters have been studied as electrocatalysts after they have been deposited onto an electrode support that is not completely inert itself. This method

produces an electrode surface modified with clusters with a dispersity of sizes making it challenging to elucidate which cluster size is responsible for the catalytic activity or what role the electrode substrate plays in the overall process. Starting with preformed ligand stabilized nanoparticles or clusters where the structure and size are well-characterized before attachment to the electrode is an alternative strategy to address these issues. Without a defined interface to the electrode, however, these stabilizing ligands can hinder electron transfer. Chapter IV describes the first examination of preformed small gold clusters as oxygen reduction electrocatalysts with a deliberate nanoparticle-electrode interface to an inert electrode support using the approach developed in Chapter III. This platform enabled a systematic study of how small changes in core size, even changes as small as one atom, can affect the resulting electrocatalytic properties. Additionally, the use of an inert substrate lead to different trends observed compared to existing studies that use reaction electrode supports, highlighting the influence of the electrode support on catalytic activity.

CHAPTER IV

ATOMICALLY PRECISE GOLD CLUSTERS TETHERED TO BORON DOPED DIAMOND THROUGH MOLECULAR LINKERS: INFLUENCE OF CORE SIZE AND CATALYST COVERAGE ON OXYGEN ELECTROREDUCTION ACTIVITY

Note: This chapter is expected to appear in an upcoming publication co-authored by Samantha L. Young and James E. Hutchison. I performed all experimental work and writing of this chapter. J.E.H. provided advice on experimental design and editorial support.

Nanoparticles and clusters are being investigated as electrocatalyst materials for many important applications such as energy production and storage,[1] biological sensors,[2] and electrosynthesis.[3] The properties of nanoparticle catalysts such as activity, selectivity, and stability have been observed to depend on their core size. When the core size of the nanoparticle is smaller than 2 nm, electronic and structural properties that are not observed in large particles emerge, including quantization of the energy levels,[4,5] an increased ratio of undercoordinated atoms at the surface which can serve as active catalytic sites, and a higher surface area to volume ratio, which is desirable for minimizing the overall amount of catalyst material that has to be used. Gold nanoparticles (AuNPs) and clusters, in particular, have been explored as catalysts for many different redox transformations.[6] Chen and co-workers reported that small gold nanoparticles/clusters ($d_{core} \leq 2$ nm) deposited onto glassy carbon electrodes were efficient oxygen reduction (ORR) electrocatalysts in alkaline electrolytes for the four-

electron pathway which directly reduces oxygen to hydroxide without the production of peroxide intermediates.[7]

Recently, we evaluated ~2 nm gold and silver nanoparticles that were molecularly tethered to boron doped diamond electrodes as ORR electrocatalysts in alkaline media using rotating ring disk voltammetry.[8] We were surprised to find that AuNPs alone catalyzed only the two-electron pathway, producing a peroxide intermediate. Addition of silver to the gold surface was necessary to catalyze the four-electron pathway. There are several differences between our ORR study with AuNPs[8] and the work reported by Chen and co-workers.[7] We measured AuNPs that were tethered to a BDD electrode through a molecular linker, in contrast to the drop-cast films of AuNPs on glassy carbon that were measured in the study by Chen and co-workers.[7] The difference in NP catalyst coverage on the electrode surface was significantly different between the two studies, with a submonolayer of AuNPs being investigated in our work and a thin film of AuNPs being measured in the report by Chen and co-workers. Finally, the catalytic activity of the electrode support is different between the two studies, since BDD is inert towards ORR while glassy carbon is active towards the two-electron ORR pathway.

Based on the findings of our study with AuNPs tethered to BDD,[8] we decided to reexamine small AuNPs that were deposited on glassy carbon electrodes to facilitate better comparison to previous work.[7] We deposited films of 1.5 nm triphenylphosphine-stabilized AuNPs (TPP-Au_{101}) onto glassy carbon electrodes through solution deposition methods without the use of a molecular linker. The concentration of the AuNP solution was varied to attempt to vary the NP coverage on the glassy carbon surface. We performed cyclic voltammetry (CV) on these TPP-Au_{101} films on glassy carbon and

found that the ORR activity varied significantly as a function of NP coverage (Figure 4.1a). On samples that had an intermediate coverage of TPP-Au_{101} on the GC surface, an improvement in ORR activity was observed, indicated by a decrease in reduction onset potential compared to bare GC (Figure 4.1a, Sample 1). However, if the coverage was too high, the cyclic voltammograms demonstrated worse activity than bare GC (Figure 4.1a, Sample 2). If the TPP-Au_{101} coverage was too low, the CV's appeared essentially identical to bare GC (Figure 4.1a, Sample 3). Rotating ring disk voltammograms of bare GC were collected using our setup, confirming that GC can catalyze the indirect two-electron pathway as evidenced by significant ring current (Figure 4.1b), consistent with previous reports.[9,10]

Based upon these results with the solution deposited TPP-Au_{101} on GC, it appears that GC likely contributes to the overall catalytic activity measured for these AuNP samples. In the samples with intermediate coverage (Figure 4.1a, Sample 1), there were presumably a sufficient number of AuNPs with good electronic connection on the GC surface for the AuNPs to influence ORR activity, but the GC surface was not completely blocked from participating in electrocatalysis. In the samples with higher AuNP coverage (Figure 4.1a, Sample 2), the worse ORR activity is likely due to passivation of the GC electrode surface preventing it from participating in ORR, and the lack of electrochemically accessible NPs with good electronic connection to the electrode. The samples with lower AuNP coverage (Figure 4.1a, Sample 3) likely did not have enough AuNPs on the surface to influence ORR significantly, and the electrocatalytic activity was dominated by the ORR active GC electrode. These findings lead us to consider the role of the electrode substrate and the nanoparticle coverage on ORR activity using our

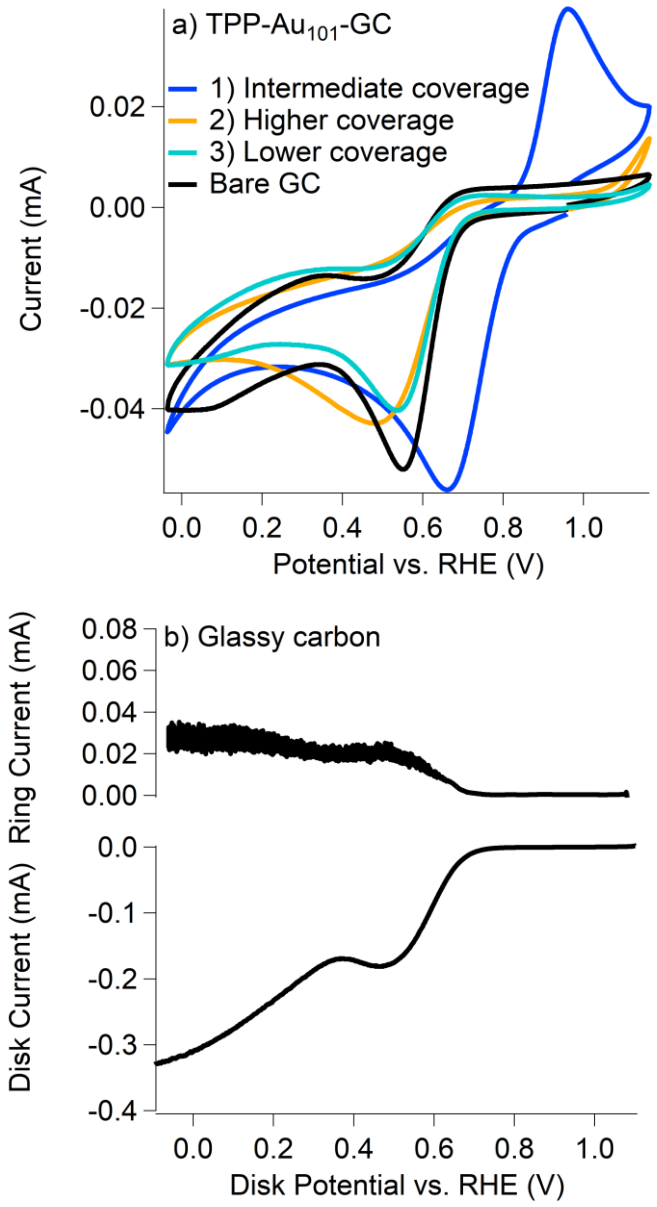

Figure 4.1. a) Overlay of cyclic voltammograms of multiple samples of TPP-Au_{101} on glassy carbon electrodes prepared using solution deposition methods taken in O_2 saturated 0.1 M NaOH at 100 mV/s. The black trace is a bare glassy carbon electrode for comparison. The sample to sample variation in the reduction onset potential and voltammogram shape demonstrates the sensitivity of the ORR activity as a function to Au cluster/NP coverage on the GC electrode. b) Rotating ring disk voltammogram of glassy carbon in O_2 saturated 0.1 M KOH at with a scan rate of 10 mV/s and a rotation rate of 500 rpm. The presence of ring current indicates that GC can reduce oxygen to peroxide in these conditions.

platform to molecularly tether AuNPs to catalytically inert boron doped diamond

electrodes.[11] Since previous reports have suggested the ORR catalytic activity increased as the size of the Au clusters/nanoparticles was decreased, we decided to examine even smaller Au clusters than previously studied to see if this trend continued.

A series of four triphenylphosphine-stabilized Au_x clusters/NPs (x= 8, 9, 11, or 101) were synthesized following published procedures[12–15] (details in Appendix B). The Au_8, Au_9, and Au_{11} clusters were further purified through crystallization and this crystallized product was used for all studies. Both ^1H and ^{31}P nuclear magnetic resonance spectroscopy (NMR) was used to verify that the clusters/nanoparticles were free from excess ligand and that the desired cluster was made (Figure B1-B4). The absence of a plasmon in the UV-Vis spectra corroborated that the clusters/NPs were smaller than 2 nm (Figure B5). The boron doped diamond (BDD) electrodes were functionalized with heptane-thioacetate monolayers through photochemically grafting 6-heptene-1-thioacetate using our previously published method.[11] The TPP-Au_x materials were assembled onto the heptane-thioacetate (HTA) monolayers through ligand exchange reactions at room temperature (TPP-Au_x-BDD). The samples were measured by x-ray photoelectron spectroscopy (XPS) (Figure B6-B9). The XPS Au:$C_{284.8}$ ratios were used to assess the extent of TPP-Au_x cluster assembly on the HTA monolayer. The higher Au:$C_{284.8}$ ratios on HTA-functionalized BDD compared to bare BDD showed that the TPP-Au_x clusters were assembled onto the thioacetate monolayer and not simply physisorbed to the BDD surface. These assembly conditions are known to preserve the core size of TPP-Au_{11} and TPP-Au_{101}[15,16] and these materials were previously assembled onto molecular monolayers on BDD.[11] To determine if the TPP-Au_8 and TPP-Au_9 clusters were able to undergo ligand exchange reactions while preserving their core size,

experiments were done reacting the Au cluster with 1 eq of 1-hexanethiol to mimic the ligand exchange reaction between the bound molecular monolayer and the cluster. DOSY ^{1}H NMR measurements suggested that the core was preserved and that the 1-hexanethiol was bound to the cluster surface (Figure B10). UV-Vis measurements corroborated that the core was preserved since the spectra shape did not change over the reaction time (Figure B5).

The ORR electrocatalytic activity of the TPP-Au_x-BDD samples were evaluated using rotating ring disk voltammetry (Figure 4.2). The presence of ring current in all TPP-Au_x-BDD samples, indicative of peroxide formation, showed that none of these materials were able to catalyze the direct, four-electron reduction pathway. The lack of current in measurements taken in argon-sparged electrolyte confirmed that the activity measured in the oxygen-sparged electrolytes was a result of ORR. The lack of significant catalytic activity for the unmodified BDD sample (Figure 4.2a) confirms that the observed catalytic activity in the TPP-Au_x-BDD samples is due to the Au_x clusters and not influenced by the electrode support. The TPP-Au_x-BDD samples were also examined as ORR electrocatalysts in acidic electrolytes. All materials were found to be less active in acid with higher overpotentials and lower currents than observed in base (Figure B11). Consequently, all subsequent experiments focused on ORR in alkaline electrolytes.

As the size of the AuNP/cluster increased, the two-electron ORR activity was observed to improve indicated by the decreased overpotentials for generation of peroxide. The reduction onset potential continuously shifted positive as the core size increased with the trend TPP-Au_9-BDD (0.55 V) < TPP-Au_{11}-BDD (0.65 V) < TPP-Au_{101}-BDD (0.85 V). TPP-Au_8-BDD did not show any significant improvement in electrocatalytic activity

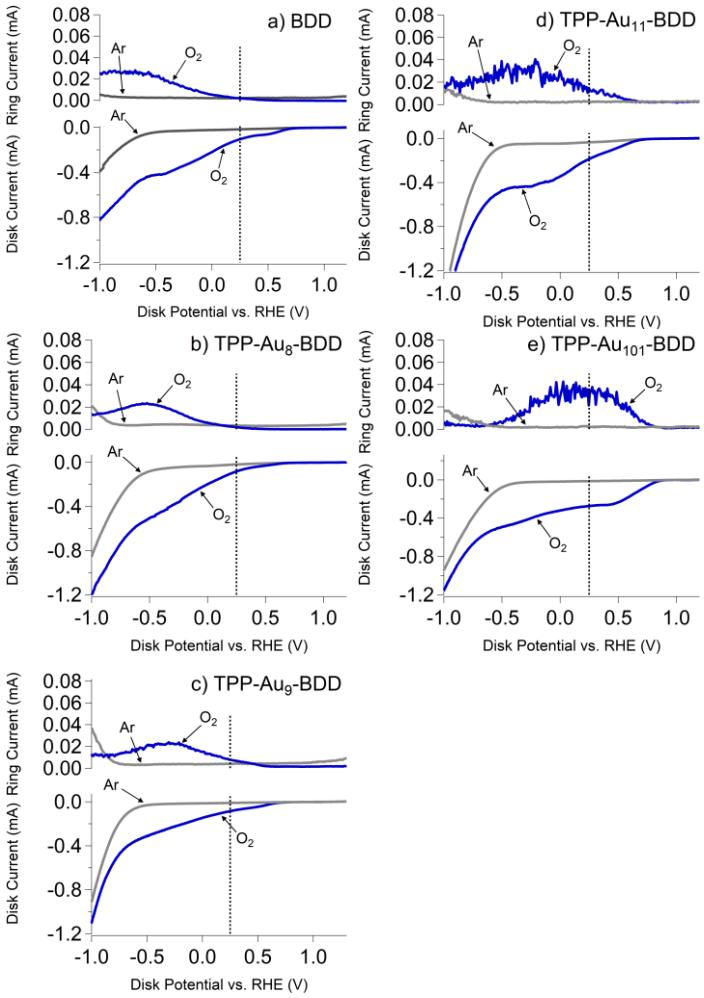

Figure 4.2. Rotating ring disk voltammograms of Au clusters/NPs tethered to BDD through heptane-thiolate linkers to evaluate their ORR electrocatalytic activity in alkaline conditions: a) bare BDD, b) TPP-Au_8-BDD, c) TPP-Au_9-BDD, d) TPP-Au_{11}-BDD, and e) TPP-Au_{101}-BDD. Measurements were taken at 20 mV/s in either O_2 saturated (blue traces) or Ar saturated (gray traces) 0.1 M KOH while rotating at 500 rpm. The vertical dashed line at 0.25 V vs. RHE is for convenient comparison between samples.

compared to the bare BDD electrode. The ~250 mV improvement in overpotential observed between TPP-Au_8-BDD (Figure 4.2b) and TPP-Au_9-BDD (Figure 4.2c) highlights how even a difference of one atom in the Au cluster can affect the electrocatalytic activity. A slight decrease in the ring current is observed at higher potentials suggesting that the Au clusters/NPs were able to begin reducing a portion of

the generated peroxide to hydroxide. Only the largest core size studied, TPP-Au_{101}-BDD (Figure 4.2e), was able to completely reduce the peroxide intermediate within this potential window, with no significant ring current remaining at -0.6 V.

Compared to the previous report by Chen and co-workers,[7] an opposite size trend was observed in this work with the larger Au clusters/NPs having lower reduction onset potentials than the smaller Au clusters/NPs. Furthermore, none of the TPP-Au_x-BDD catalysts in this study were observed to catalyze the four-electron ORR pathway which is in contrast to what was reported with small AuNPs on glassy carbon.[7] There are several differences between this work and the work by Chen and co-workers[7] that could potentially explain the conflicting trends. First, the surface chemistry is not identical in all cases since only two of the AuNPs/clusters examined by Chen and co-workers were stabilized by triphenylphosphine ligands and the influence of surface chemistry was not examined in depth in their work.[7] Electrochemical cycling is known to cause ligand desorption from surfaces.[17] The P 2p XPS spectra of TPP-Au_{11}-BDD and TPP-Au_{101}-BDD were examined before and after electrochemistry. Approximately one-third of the TPP ligands were lost on the TPP-Au_{11}-BDD sample as determined by comparing the P:Au ratios, while almost all of the TPP ligands were lost on the TPP-Au_{101}-BDD sample with no significant P 2p signal present after electrochemical cycling (Table B1). The ability of the larger TPP-Au_{101} sample to lose ligands more readily providing a larger proportion of bare Au surface to serve as catalytically active sites is one reason it might be more catalytically active than the smaller clusters in this study.

Another significant difference between this work and previous reports is that the TPP-Au_x clusters are bound to a catalytically inert electrode support (BDD) which means

that the Au NPs/clusters are solely responsible for the production of ORR catalytic activity. The previous study used glassy carbon as an electrode support which is itself able to reduce oxygen to produce peroxide (Figure 4.1b). It is possible that in previous work, the GC and the Au clusters/NPs are acting as co-catalysts with GC readily producing peroxide that can easily diffuse to a neighboring Au cluster/NP to undergo further reduction.

Finally, the cluster/NP coverage on the BDD surface is orders of magnitude less than the drop-cast AuNP films on GC measured by Chen and co-workers.[7] It is possible that having higher coverage of Au clusters/NPs on the surface could allow a peroxide intermediate produced at a Au cluster/NP to immediately diffuse to a neighboring cluster/NP to undergo further reduction before it is able to diffuse away from the electrode surface into the electrolyte as has been discussed in previous work with larger nanodisk catalysts.[18,19] The probability of this occurring would decrease as the cluster/NP coverage on the electrode surface is lowered.

The influence of AuNP/cluster catalyst coverage on ORR activity was further investigated using TPP-Au_{11} tethered to BDD. A sample of TPP-Au_{11}-BDD was made with higher coverage and then compared to the lower coverage TPP-Au_{11} sample. The coverage of TPP-Au_{11} was increased by assembling TPP-Au_{11} onto the HTA-BDD surface by heating at 50°C which are conditions known to promote ligand exchange of this material while preserving the original core.[13] The ORR activity of the two samples with varying coverage were then compared using rotating ring disk voltammetry (Figure 4.3). Both TPP-Au_{11}-BDD samples were still only active for the two-electron ORR pathway as evidenced by the presence of significant ring current (Figure 4.3). However,

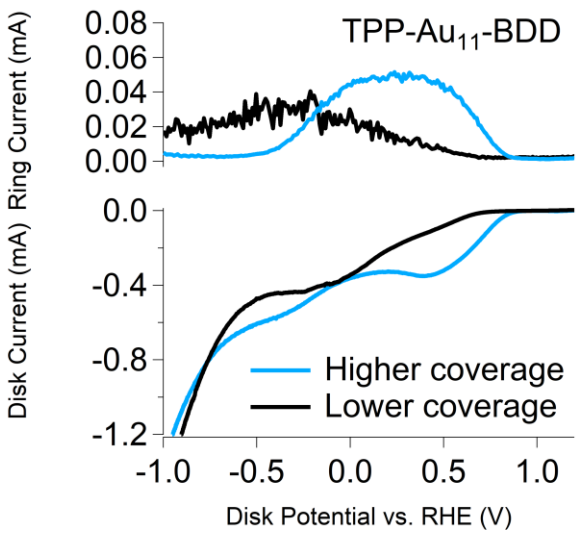

Figure 4.3. Rotating ring disk voltammograms of TPP-Au_{11}-BDD samples in O_2 saturated 0.1 M KOH with higher coverage (blue trace) or lower coverage (black trace) of the TPP-Au_{11} cluster on the electrode.

the TPP-Au_{11}-BDD sample with higher coverage was more active for two-electron ORR with the reduction onset potential shifted ~250 mV more positive than the sample with lower coverage (Figure 4.3). The generated peroxide intermediate was also more quickly reduced in the higher coverage sample evidenced by the decrease in ring current beginning at ~0.1 V than the lower coverage sample. The improvement in overpotential and the more facile reduction of the peroxide intermediate in the higher coverage TPP-Au_{11} sample suggests that having clusters/NPs close to one another improves ORR electrocatalysis (Figure 4.3). Additionally, the TPP-Au_{11}-BDD sample with higher coverage had a reduction onset potential more comparable to what was previously reported,[7] suggesting that coverage played a role in that work. While further work will need to be done to fully understand the effect of NP coverage, these results highlight the importance of considering NP coverage when evaluating materials and methods to control NP coverage on electrode supports should be explored.

In this work, a series of four atomically precise Au clusters/NPs were assembled onto molecular monolayers on boron doped diamond electrodes. This is the first report of a submonolayer of preformed clusters of this size with a defined molecular NP/electrode interface being evaluated as electrocatalysts. When a submonolayer of AuNPs/clusters were interfaced to a catalytically inert boron doped diamond electrode, they exhibited two-electron ORR activity in alkaline electrolytes. The two-electron ORR activity observed in this work with the Au clusters/NPs tethered to BDD is in contrast to the four-electron ORR activity previously reported for films of AuNPs deposited on glassy carbon electrodes.[7] While previous work predicted that the ORR activity would improve as the AuNP/cluster core size was decreased, we observed that the overpotential for the two-electron ORR pathway decreased as the AuNP/cluster core size was increased, opposite of the predicted result. The significant differences observed between Au_8, Au_9, and Au_{11} demonstrated that a difference of only a few atoms can influence the catalytic activity, highlighting the importance of knowing what material is being deposited onto the surface which is not always known when clusters are deposited on the surface through methods such as electrodeposition. These results demonstrate the importance of considering the influence of the electrode support and the catalyst density on the electrode surface when evaluating nanomaterial catalysts.

Bridge to Chapter V

Chapter IV demonstrated the use of my nanoparticle/electrode platform to investigate the influence of gold nanoparticle and cluster size on the electrocatalytic activity for the oxygen reduction reaction for this catalytically interesting size regime. Chapter V expands upon this platform to investigate the influence of elemental

composition and structure for bimetallic silver-gold nanoparticles on their ability to catalyze the oxygen reduction reaction. In literature reports, bimetallic nanoparticles have been demonstrated enhanced catalytic activities compared to their monometallic counterparts as a result of synergistic interactions between the two metals. However, it has traditionally been challenging to examine the influence of elemental composition and placement without competing effects since maintaining the core size and morphology across different compositions can be challenging using traditional nanoparticle synthetic techniques. In Chapter V, a series of silver-gold nanoparticles molecularly tethered to boron doped diamond electrodes were produced through the modification of the surface of the bound gold nanoparticle with silver using the techniques of underpotential deposition/galvanic exchange or anti-galvanic reduction. This approach rapidly produces series of nanoparticles with different compositions while preserving the nanoparticle core morphologies and defined molecular interfaces to the electrode. These studies allowed for further insight into how the elemental composition and structure influences the catalytic activity of silver-gold nanoparticles.

CHAPTER V

SMALL SILVER-GOLD NANOPARTICLE ELECTROCATALYSTS MOLECULARLY INTERFACED TO BORON DOPED DIAMOND: ASSESSING THE INFLUENCE OF CORE SIZE, STRUCTURE, AND COMPOSITION ON OXYGEN ELECTROREDUCTION IN ALKALINE CONDITIONS

Note: This chapter is expected to appear in an upcoming publication co-authored by Samantha L. Young and James E. Hutchison. I performed all experimental work and writing of this chapter. J.E.H. provided advice on experimental design and editorial support.

Introduction

Improved heterogeneous electrocatalysts are needed to realize new applications such as energy production and storage,[1] amperometric sensing in biological systems,[2] wastewater remediation,[3] and electrosynthesis.[4] These catalysts need to be efficient (low overpotential and high current density), selective for the desired product, stable, and ideally made from cheap elements. Nanoparticles (NPs) are one class of heterogeneous electrocatalysts that have shown promise as electrocatalysts. Nanoparticles possess high surface area to volume ratios, core size dependent properties, and a high proportion of undercoordinated atoms at their surface which can serve as active catalytic sites, all of which make them attractive materials to investigate as electrocatalysts. Multimetallic NPs can further introduce unique catalytic properties from synergistic interactions of multiple elements on the nanoscale. These synergistic effects can result in unique

electronic and structural properties that are not observed in their monometallic nanoparticle analogues.[5,6]

Maintaining control over the subnanometer composition and structure of nanoparticle electrocatalysts is complex and has prevented elucidation of precise nanoparticle structure/catalytic activity relationships. The electrocatalytic activity of nanoparticle electrocatalysts can be influenced by the nanoparticle's core size, surface chemistry, proportion of undercoordinated surface atoms on their surface, coverage or loading on a support, and their interface to an electrode support.[7] Active nanoparticle catalysts are often very small (< 5 nm) which can make analyzing their morphologies on an electrode support material challenging. Multimetallic nanoparticles are even more challenging to characterize in terms of understanding the overall composition, which metal or metal combinations are on the surface and serving as active catalytic sites, and how the different metals influence each other electronically and structurally in a synergistic fashion. Recently, we reported a method to interface a monolayer of small AuNPs (d_{core} < 2.5 nm) to boron doped diamond electrodes through covalently bound molecular linkers.[8] This method provides a defined, molecular nanoparticle-electrode interface that promotes efficient electron transfer and provides a higher electrochemically active surface area compared to nanoparticles attached to boron doped diamond through solution deposition methods where the interface was less defined. Boron doped diamond is electrocatalytically inert making it a good choice of support to examine the catalytic properties of the nanoparticle catalysts without effects from the support. The control that this method provides over the nanoparticle-functionalized electrode makes it an effective platform to evaluate the electrocatalytic activity of nanoparticles.

Improved catalysts are needed for the oxygen reduction reaction (ORR). ORR is the cathodic reaction that is the basis for many energy conversion technologies, but it suffers from slow kinetics.[9] For fuel cell technologies, catalysts that can reduce oxygen directly to hydroxide (in alkaline media) in one step without producing peroxide intermediate products is preferred since it is energetically favorable and no corrosive peroxide intermediates are formed that can damage fuel cell membranes. Currently, platinum based catalysts are the best ORR catalysts reported for the direct, four-electron ORR pathway.[6] There have been a number of research efforts to find alternative Pt-free catalyst materials that can maintain the same level of ORR activity, but reduce costs. Several classes of Pt-free nanomaterials have been reported to be efficient four-electron ORR catalysts in alkaline media,[10] including transition metal oxides (e.g., Mn_3O_4 nanoparticles[11]), doped carbon nanomaterials (e.g., N or S-doped graphene[12]) and other noble metals (e.g., Pd[13], Ag[14], and Au[15] nanostructures). Noble metal electrocatalysts have the advantage of increased durability over longer periods of operation and better electrical conductivity than metal oxides or carbon nanomaterials.

Bimetallic Ag-Au nanostructures are one Pt-free material that has been reported to have ORR electrocatalytic activity comparable to Pt in alkaline conditions.[16–19] The advantages of using Ag-Au bimetallic nanostructures are two-fold: 1) The combination of the two metals has been reported to exhibit improved ORR catalytic activity compared to their monometallic counterparts, and 2) The substitution of Ag for Au reduces the overall amount of the more expensive metal used. Several studies examining 4-8 nm Ag-Au nanostructures deposited on glassy carbon electrodes reported that the ORR catalytic performance of Ag-Au bimetallic NPs is affected by the ratio of the two metals in the NP

with slight shifts in the reduction offset potential as the Ag:Au ratio was changed.[18,19] Additionally, the arrangement of the two elements in the NP (alloy, core-shell, or Janus structure) was observed to affect the ORR overpotential.[16,17] In studies by Chen and co-workers, all of the Ag-Au bimetallic NPs were better ORR electrocatalysts compared to the monometallic AgNPs.[16,17] However, the Janus and core-shell structured Ag-AuNPs exhibited better ORR catalytic activity in alkaline conditions when compared to the alloyed Ag-AuNPs.[16,17] The enhanced ORR activity of the Janus/core-shell Ag-Au nanoparticles was hypothesized to be a result of the asymmetric structure of the two metals in the Ag-AuNP that facilitated electron transfer from Ag to Au as well as synergistic effects resulting from accessibility of the two metals during catalysis. These previous studies that have reported improved ORR activity through varying the elemental composition and from using Janus or core-shell Ag-Au bimetallic NPs suggest that further exploration of how the amount of Ag added to AuNP surfaces influences ORR catalytic performance would be beneficial.

While this previous work demonstrates the promise of Ag-Au nanostructured ORR electrocatalysts, differences in the nanostructure morphology between compositions and the methods used to attach the NP electrocatalyst to an electrode support add some uncertainty when attempting to extract nanostructure/electrocatalytic activity relationships. In the studies that examined the role of elemental composition on ORR activity, the shape and size of the nanostructures changed in addition to the composition making it challenging to isolate the effect of composition on the resulting electrocatalytic properties. All of the studies discussed above formed a catalyst ink by sonicating the Ag-Au nanomaterials in the presence of a carbon powder or Nafion. Sonication can induce

size changes and metal leaching in nanoparticles adding uncertainty in how the structure of the Ag-Au nanostructure changed while attaching it to the electrode .[20] The Ag-Au/carbon catalyst inks were then drop-cast onto a glassy carbon electrode for electrochemical analysis. Solution deposition methods to attach NPs to electrode supports, such as drop-casting, do not produce a defined interface between the nanoparticles and the electrode. This lack of defined interface can hinder electron transfer due to the electrically insulating ligands that stabilize the nanoparticle core.[8] In addition to the ill-defined interface between the NP and the electrode, the choice of glassy carbon as the electrode support complicates analysis of the nanomaterial's ORR electrocatalytic activity since glassy carbon is not completely inert to ORR in alkaline conditions.[21] Finally, all of the previous studies with Ag-Au bimetallic NP ORR electrocatalysts have examined nanoparticles that are at least 4 nm or larger in core size.[16–19] The properties of metallic NPs have been observed to change drastically as the core diameter is decreased to ~2.5 nm or smaller, inspiring interest in studying these materials as catalysts. Exploration of smaller Ag-Au bimetallic nanoparticles still needs to be performed to understand the influence of structure and composition on ORR activity in this unique size regime. Utilizing an approach to fabricating a bimetallic nanoparticle electrocatalyst that would incorporate small NPs with a defined interface to an inert electrode support and would allow for systematic variation of the composition without inducing morphology changes would help further understanding of the catalytic properties of these materials.

In this work, a series of ~2 nm Ag-AuNPs interfaced to boron doped diamond through undecanethiolate linkers were studied as ORR electrocatalysts in alkaline

conditions. Varying amounts of Ag were added to the surface of grafted 2.1 nm undecenethiolate stabilized-AuNPs through either galvanic replacement of copper that was underpotentially deposited onto the AuNP surface or through anti-galvanic reduction while preserving the NP monolayer on the BDD electrode. Ag-AuNPs with varying Ag:Au ratios were evaluated for ORR electrocatalytic activity and stability using rotating ring disk voltammetry. As the amount of Ag was increased on the AuNP surface, the direct, four-electron ORR pathway was observed to be the primary mechanism. The grafted 2 nm Ag-AuNPs were found to outperform monometallic AgNPs and AuNPs as ORR catalysts, and were found to be stable for at least 30 minutes of continuous operation without loss of activity. The 2 nm Ag-AuNPs were found to be significantly better ORR catalysts than larger bimetallic Ag-AuNPs or 2 nm bimetallic NPs prepared by addition of Au to a AgNP core, indicating unique synergistic effects resulting from this particular structure. Changes in the Ag-AuNP structure resulting from electrochemical cycling were measured. The role of synergistic electronic and structural effects in the unique ORR activity of the 2 nm Ag-AuNPs are evaluated.

Experimental

Materials and Characterization. Water (18.2 MΩ·cm) was produced from a Barnstead Nanopure Diamond system. Hydrogen tetrachloroaurate was purchased from Strem Chemicals. Silver nitrate, silver sulfate, and copper sulfate were obtained from Mallinckrodt. Potassium hydroxide (semiconductor grade, 99.99%) was purchased from Aldrich. All reagents were used as received without further purification. Free-standing, electrochemical grade boron doped diamond substrates (Element Six) were custom cut into round disks (0.78 cm^2) to be used in the rotating ring disk electrode setup.

Nuclear magnetic resonance spectroscopy (^{1}H NMR) was performed on a Varian Inova 500 MHz instrument to assess the purity of materials. Ultraviolet-visible (UV-Vis) spectra of nanoparticle samples were collected on a Shimadzu Bio-Spec-1601 DNA/Protein/Enzyme Analyzer in a quartz cuvette (1 cm path length). Transmission electron microscope (TEM) images of the undecenethiolate-stabilized AgNPs were collected on a FEI Tecnai G2 Spirit TEM instrument. Samples were prepared for TEM analysis by drop-casting a dilute solution on a lacey carbon copper coated TEM grid (Ted Pella).

X-ray photoelectron spectroscopy (XPS) was performed on a ThermoScientific ESCALAB 250 X-ray Photoelectron Spectrometer using an Al Kα monochromated source (150 W, 20 eV pass energy, 500 μm spot size). A Smart background was used for spectra analysis and spectra were referenced to the C 1s hydrocarbon peak (284.8 eV). Peak fitting was done using ThermoScientific Avantage 4.75 software. Scanning electron microscope images of the nanoparticle functionalized electrodes were collected on a FEI Helios NanoLab 600i FIB-SEM instrument in immersion mode using an accelerating voltage of 5 kV, a working distance of ~3 mm, and a Through-Lens detector.

Electrochemical measurements were performed on a Bio-Logic SP-300 potentiostat. The NP-functionalized BDD working electrode was housed inside a Pine Research ChangeDisk RRDE tip (PTFE shroud, platinum ring) for all measurements using a glassy carbon support disk to make electrical contact with the holder. The ChangeDisk RRDE tip was attached to a Pine Research MSR rotator. Ag|AgCl reference electrodes (3 M NaCl, Bioanalytical Systems) were used for copper underpotential deposition. A Hg|HgO reference electrode (CH Instruments) was used for

electrocatalysis experiments. The collection efficiency of the rotating ring disk electrode setup was calculated to be 30% determined from measurement of 1 mM potassium ferricyanide in 0.5 M KCl.

*Synthesis of undecenethiolate-stabilized gold or silver nanoparticles (**UDT-AuNPs** and **UDT-AgNPs**).* UDT-AuNPs were synthesized from a modified two-phase Brust preparation as described in our previous publication.[8,22] UDT-AgNPs were synthesized based on a previously reported procedure with slight modifications.[17] Silver nitrate (0.17 g, 1.0 mmol) was dissolved in 30 mL of water (18.2 MΩ) in a 100 mL round bottom flask equipped with a large magnetic stir bar. Tetraoctylammonium bromide (TOAB) (2.1 g, 3.8 mmol) was dissolved in 20 mL of toluene and added to the $AgNO_3$ solution and stirred for an hour. The aqueous phase was discarded and 10-undecene-1-thiol (UDT) (0.22 g, 1.1 mmol) was added to the remaining slightly gray colored organic phase. The solution was allowed to stir for 15 minutes before adding a freshly made aqueous solution of sodium borohydride (0.45 g, 12 mmol, 20 mL H_2O) in one portion while vigorously stirring. The reaction turned dark brown over the course of one minute and was allowed to stir for four hours at room temperature. The organic phase was then collected and the solvent was removed via rotary evaporation. The material was purified by several precipitation/centrifugation steps with dichloromethane/methanol to remove excess UDT and TOAB.

Grafting undecenethiolate-AuNPs and AgNPs to boron doped diamond. Undecenethiolate-stabilized AuNPs (UDT-AuNPs) and AgNPs (UDT-AgNPs) were grafted to boron doped diamond electrodes following our previously published procedure.[8] Briefly, a dilute solution of UDT-AuNPs or UDT-AgNPs in heptane was

added to a 10 mL beaker containing a hydrogen terminated BDD substrate which was placed into a homemade grafting chamber. The sample was irradiated through a quartz slide with a 254 nm UVP UVGL-58 Hand-held UV lamp (~1 mW/cm^2) for seven hours under argon. The samples were rinsed with dichloromethane to remove physiadsorbed nanoparticles.

Modifying the surface of undecenethiolate-stabilized AuNPs with silver (Ag-AuNP-BDD). Before addition of silver, a portion of the UDT ligands were first removed from UDT-AuNP-BDD by treating the sample with dilute ozone (~50 ppm, diluted with N_2) for five minutes using a previously reported method.[23] The AuNP surface was modified with copper using underpotential deposition (UPD) via chronoamperometry. The electrochemical setup for Cu UPD consisted of the **UDT-AuNP-BDD** working electrode housed in the rotating ring disk electrode setup which was rotated at 500 rpm during deposition, a glass electrochemical cell containing an acidic $CuSO_4$ solution (1 mM in 0.1 M H_2SO_4), a Ag|AgCl (3 M NaCl) reference electrode, and a platinum wire auxiliary electrode. The amount of copper that was underpotentially deposited on the AuNP surface was controlled by varying the deposition time (1-30 seconds) and/or the deposition potential (50-150 mV vs. Ag|AgCl). The samples were rinsed extensively with water before immersing them in an acidic solution of silver sulfate for 15 hours (0.1 mM Ag_2SO_4 in 0.1 M H_2SO_4) to galvanically replace the copper on the NP surface with silver. Alternatively, several **Ag-AuNP-BDD** samples were also prepared without the Cu UPD step, by simply soaking ozone treated **UDT-AuNP-BDD** in acidic silver sulfate solutions of varying concentrations (0.1 mM to saturated Ag_2SO_4 in 0.1 M H_2SO_4) for 15

hours. The **Ag-AuNP-BDD** samples were extensively rinsed with H_2O to remove any physiadsorbed Ag_2SO_4 before performing subsequent characterization.

Modifying the surface of undecenethiolate-stabilized AgNPs with gold (Au-AgNP-BDD). **UDT-AgNP-BDD** was placed in aqueous solution of $HAuCl_4$ (~1.3 μM) for ~1 hour to exchange a portion of the Ag atoms for Au without causing significant etching/pitting of the AgNP core. Some samples were also prepared by immersing UDT-AgNPs in a more concentrated aqueous solution of $HAuCl_4$ (500 μM) for 15 hours to try to increase the amount of gold on the AgNPs. All samples were rinsed extensively with water to remove excess $HAuCl_4$ before subsequent analysis.

Assembling larger citrate stabilized AuNPs onto heptane-thioacetate monolayers on boron doped diamond. The heptane-thioacetate monolayer was formed through grafting 6-heptene-1-thioacetate to hydrogen terminated BDD using previously reported conditions.[8] Citrate stabilized AuNPs (Sigma Aldrich, 10 nm in diameter, OD = 1, stabilized in citrate buffer) were added to a 1 mL centrifuge tube and spun at 15000 rpm for 45 minutes to remove some excess citrate buffer, forming a loose pellet of AuNPs. The supernatant was discarded, and the NP pellet was redispersed in 0.5 mL nanopure H_2O (pH adjusted to 11 with NaOH), followed by addition of 0.1 mL of a saturated NaCl solution to slightly destabilize the AuNPs in order to promote binding to the thioacetate monolayer. A heptane-thioacetate functionalized BDD was immersed in this solution of AuNPs overnight. Samples were rinsed extensively with nanopure H_2O before further analysis. Silver was added to the surface of these AuNPs using the methods as described above for the 2 nm AuNPs.

Evaluating samples as oxygen electroreduction electrocatalysts in alkaline conditions. The NP-BDD disk electrodes were placed in the rotating ring disk holder. The electrochemical cell was a Nalgene container (125 mL), the reference electrode was a Hg|HgO electrode (1 M KOH), and the auxiliary electrode was a coiled platinum wire. Glass components were avoided to prevent cell contamination from etching by KOH. The electrolyte (0.1 M KOH, ~40 mL) was sparged for at least 10 minutes before taking measurements with oxygen when assessing ORR electrocatalysis or with argon for control experiments. The working electrodes were rotated at 500 rpm during measurement while bubbling either oxygen or argon during data collection. RRDE voltammograms are plotted versus the reference hydrogen electrode (RHE) for ease of comparison to existing literature.

Results and Discussion

The aim of this work was to evaluate different compositions of Ag-Au nanoparticles as ORR electrocatalysts using the existing platform that provides a well-defined molecular interface between the nanoparticle and the catalytically inert boron doped diamond electrode support. One way to extend this platform to rapidly fabricate a series of Ag-AuNPs of different bimetallic compositions is by using the techniques of underpotential deposition, galvanic exchange, and anti-galvanic reduction (Scheme 5.1). Underpotential deposition of a metal occurs at a potential more positive than its thermodynamic reduction potential when the interactions between a metal ion in solution and a substrate are stronger than the interactions between the metal ions themselves.[24] This phenomenon has been employed to functionalize a number of metallic substrates with a submonolayer or monolayer of a new metal, and the amount of the new metal

introduced can be controlled through varying the deposition potential and time.[24] The underpotential deposition of copper has been extensively studied on planar Au surfaces[24] and has also been demonstrated on larger AuNP surfaces.[25,26] Once copper has been deposited onto the AuNP surface, it can be replaced on Ag through galvanic exchange reactions (Scheme 5.1, Method 1). Alternatively, it has been reported that when Au clusters and small AuNPs are immersed in a solution containing Ag^{+}, spontaneous reduction of Ag onto the Au surface occurs through a

Scheme 5.1. Two routes to Ag-AuNPs molecularly tethered to boron doped diamond electrodes

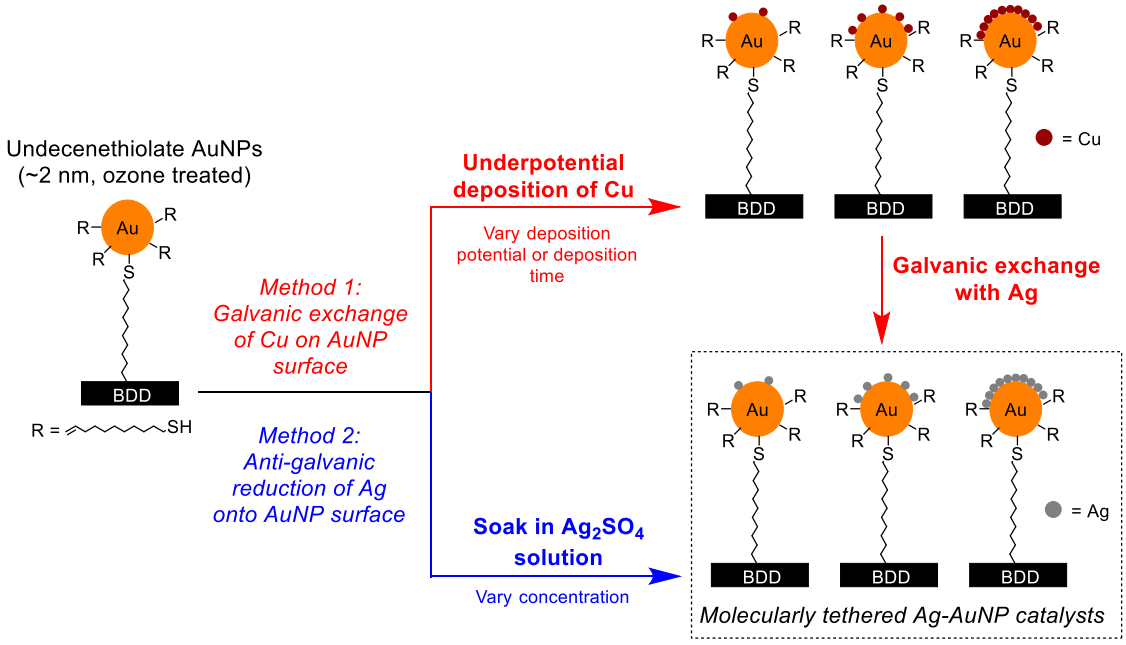

phenomenon called anti-galvanic reduction (Scheme 5.1, Method 2).[27,28] While the origins of anti-galvanic reduction are still not fully understood, it is thought to be catalyzed by highly reactive atoms at a nanoparticle surface. Both methods should be selective for the AuNP surface and the amount of Ag deposited should be limited to a few monolayers since the deposition is a result of unique interactions with Au. Since the Ag is being deposited onto small, monodisperse AuNP cores already bound to electrode

surface, a series of Ag-AuNPs with different Ag:Au ratios can be quickly synthesized while maintaining the same core size, and excess Ag salts can simply be removed through rinsing with water.

Fabricating silver-modified gold nanoparticle (Ag-AuNP-BDD) and gold-modified silver nanoparticle (Au-AgNP-BDD) electrocatalysts. *Synthesis and characterization of the undecenethiolate-stabilized gold and silver nanoparticles for grafting to BDD.* The undecenethiolate-stabilized AuNPs (UDT-AuNPs) and undecenethiolate-stabilized AgNPs (UDT-AgNPs) were synthesized from modified two-phase Brust preparations.[8,17,22] From TEM, both sets of nanoparticles are spherical in shape (Figure C1 and C2). From TEM analysis of 1183 NPs, the core size distribution of UDT-AgNPs are 2.5 ± 0.7 nm (Figure C1). The size distribution of the UDT-AuNPs were previously found to be 2.1 ± 0.1 nm by small angle x-ray scattering.[8] UV-vis spectra of the UDT-AuNPs showed no strong plasmon resonance (Figure C3), and the UDT-AgNPs showed a broad plasmon peak around 450-500 nm as is expected for NPs in this size range (Figure C4). ^{1}H NMR verified that the undecenethiolate ligands were bound to the AgNP surface indicated by the broadened peaks (Figure C5). The presence of the undecenyl disulfide after decomposition of the UDT-AgNPs with iodine provided further confirmation that the NPs were stabilized by an undecenethiolate ligand shell (Figure C5).

Addition of silver to UDT-AuNP-BDD. UDT-AuNPs were photochemically grafted to boron doped diamond that was previously shown to covalently bind UDT-AuNPs to BDD through a molecular interface while preserving the NP core integrity.[8] **UDT-AuNP-BDD** samples were treated with dilute ozone to remove a portion of the

thiolate ligand shell to reveal bare Au surface for subsequent functionalization steps and catalysis applications.[23] In one approach, copper was first deposited onto the AuNP surface through underpotential deposition (UPD), followed by exchanging the copper for silver via galvanic replacement (Scheme 5.1, Method 1). The amount of silver deposited on the AuNPs could be somewhat varied by changing the copper deposition potential or time (Table 5.1). Lower deposition potentials or longer deposition times typically produced samples with higher silver content as assessed by XPS Ag:Au ratios. Very minimal copper was detected, even for the sample with the most copper deposited (**1.8-Ag-AuNP-BDD**), suggesting that the galvanic replacement for silver was successful.

In a second approach, **Ag-AuNP-BDD** samples were prepared without the Cu UPD step by simply exposing **UDT-AuNP-BDD** to silver sulfate (Scheme 5.1, Method 2). Silver deposited directly on the AuNPs (without the copper underpotential deposition step) through a process that has been described as anti-galvanic reduction.[27,28] The amount of silver deposited could be varied by changing the concentration of the Ag_2SO_4 solution (Table 5.1). However, the highest Ag:Au ratios could be achieved on the samples prepared through the Cu UPD/galvanic exchange approach (Table 5.1). Thiolate sulfur (~163 eV) was detected by XPS for **Ag-AuNP-BDD** samples prepared through either method of Ag deposition, suggesting that the UDT-AuNP core remained intact (Figure C6) during silver deposition.

Several control experiments were performed to determine if silver was only depositing on the AuNP surface or if it was also depositing on the BDD electrode substrate. Bare BDD substrates were put through the both the UPD approach (Table 5.1, **BDD-UPD)** and the anti-galvanic reduction deposition procedures (Table 5.1, **BDD-**

Ag_2SO_4) used to fabricate the **Ag-AuNP-BDD** samples. By XPS, the Ag:$C_{284.8}$ ratio was only 0.0006 ± 0.0002 for **BDD-UPD**, and no Ag was detected for **BDD-Ag_2SO_4** indicating that the majority of the Ag signal observed in the **Ag-AuNP-BDD** samples was from silver that deposited on the AuNP surface.

Shifts in the Au 4f and Ag 3d XPS binding energies were further evidence of the Ag being deposited onto the AuNP surface (Table 5.1). In general, the Au binding energies were shifted to higher values and the Ag binding energies were shifted to lower values in the **Ag-AuNP-BDD** samples compared to what they were in their respective monometallic NP systems. These binding energy shifts are indicative of an electronic interaction between the Ag and Au, and has been previously observed in other multi-metallic nanostructures.[17,18,29]

Table 5.1. XPS ratios and binding energies for Ag-AuNP-BDD samples						
Sample	*Cu deposition potential vs. Ag|AgCl (mV)*	*Cu deposition time (s)*	*XPS Ag:Au ratio*	*XPS Ag:$C_{284.8}$ ratio*	*Au binding energy (eV)*	*Ag binding energy (eV)*
1.8-Ag-AuNP-BDD	50	30	1.8 ± 0.3	0.18 ± 0.01	84.43	368.29 ± 0.03
1.00-Ag-AuNP-BDD	100	45	1.00 ± 0.02	0.053 ± 0.007	84.827 ± 0.006	368.77 ± 0.01
0.50-Ag-AuNP-BDD	100	5	0.50 ± 0.01	0.042 ± 0.009	84.89 ± 0.06	368.57 ± 0.07
0.36-Ag-AuNP-BDD	100	30	0.36 ± 0.02	0.043 ± 0.001	84.92 ± 0.01	368.55 ± 0.01
0.28-Ag-AuNP-BDD	150	30	0.28 ± 0.02	0.032 ± 0.004	84.91 ± 0.03	368.53 ± 0.05
0.25-Ag-AuNP-BDD[a]	-	-	0.25 ± 0.02	0.019 ± 0.002	84.897 ± 0.006	368.54 ± 0.06
0.48-Ag-AuNP-BDD[b]	-	-	0.48 ± 0.05	0.032 ± 0.004	84.87 ± 0.03	368.60 ± 0.04
BDD-UPD (control)[c]	50	30	-	0.0006 ± 0.0002	-	368.8 ± 0.2
BDD-Ag_2SO_4 (control)[d]	-	-	-	no Ag detected	-	-
UDT-AuNP-BDD	-	-	-	-	84.72 ± 0.01	-
UDT-AgNP-BDD	-	-	-	0.12 ± 0.01	-	368.873 ± 0.006

[a]UDT-AuNP-BDD soaked in 0.1 mM Ag_2SO_4 in 0.1 M H_2SO_4 without the Cu UPD step
[b]UDT-AuNP-BDD soaked in saturated Ag_2SO_4 in 0.1 M H_2SO_4 without the Cu UPD step
[c]Bare BDD substrate that underwent the same deposition process used to make Ag-AuNP-BDD with the Cu UPD method
[d]Bare BDD substrate that was soaked in saturated Ag_2SO_4 in the same way used to make Ag-AuNPs via the anti-galvanic reduction method

Addition of gold to UDT-AgNP-BDD. To fabricate **UDT-AgNP-BDD**, UDT-AgNPs were first grafted to BDD in a manner identical to grafting the UDT-AuNP analogue. The UDT-AgNPs that underwent grafting to BDD resulted in a Ag:$C_{284.8}$ XPS ratio of 0.12 ± 0.01. A BDD sample that was exposed to UDT-AgNPs without irradiation by 254 nm light had an XPS Ag:$C_{284.8}$ ratio of only 0.045 ± 0.004 indicating that the

grafting was successful. The S 2p XPS signal from the undecenethiolate ligand was still present after grafting suggesting that the AgNPs remained stable throughout the grafting process (Figure C7).

To introduce Au onto the surface of the AgNPs, the **UDT-AgNP-BDD** samples were immersed in an aqueous solution of $HAuCl_4$ of varying concentrations to exchange some of the Ag atoms for Au through galvanic replacement. XPS showed that Au successfully replaced some of the Ag atoms. Samples exposed to a more dilute $HAuCl_4$ solution (~1.3 μM) had a Au:Ag XPS ratio of 0.03 ± 0.01 (average of six spots across two samples). Samples soaked in a more concentrated $HAuCl_4$ solution (~500 μM), resulted in a higher Au:Ag ratio of 8 ± 3 (average of six spots across two samples) indicating that Au did not only replace Ag atoms at the AgNP surface which is expected from literature.[30,31] A second small signal in the Au 4f XPS spectrum was also detected at a more positive binding energy, and a Cl 2p signal was detected indicating that some $HAuCl_4$ was likely still present after galvanic exchange. Thiolate sulfur was still detected in the XPS S 2p region in both samples suggesting that the UDT-AgNPs are still stabilized by thiolate ligands. Shifts in the Au and Ag binding energies were observed, similar in direction to those observed with **Ag-AuNP-BDD**, supporting that the Au was added to the AgNP (Figure C8). A BDD sample exposed to $HAuCl_4$ did not show any significant Au signal by XPS, indicating that Au is reacting with the AgNP.

SEM was performed to assess the morphology of the nanoparticles as well as their coverage on the BDD surface (Figure 5.1). The morphology of the UDT-AuNPs (Figure 5.1a) and UDT-AgNPs (Figure 5.1b) are spherical and are uniformly distributed across the BDD surface. No significant change in morphology or in NP coverage was observed

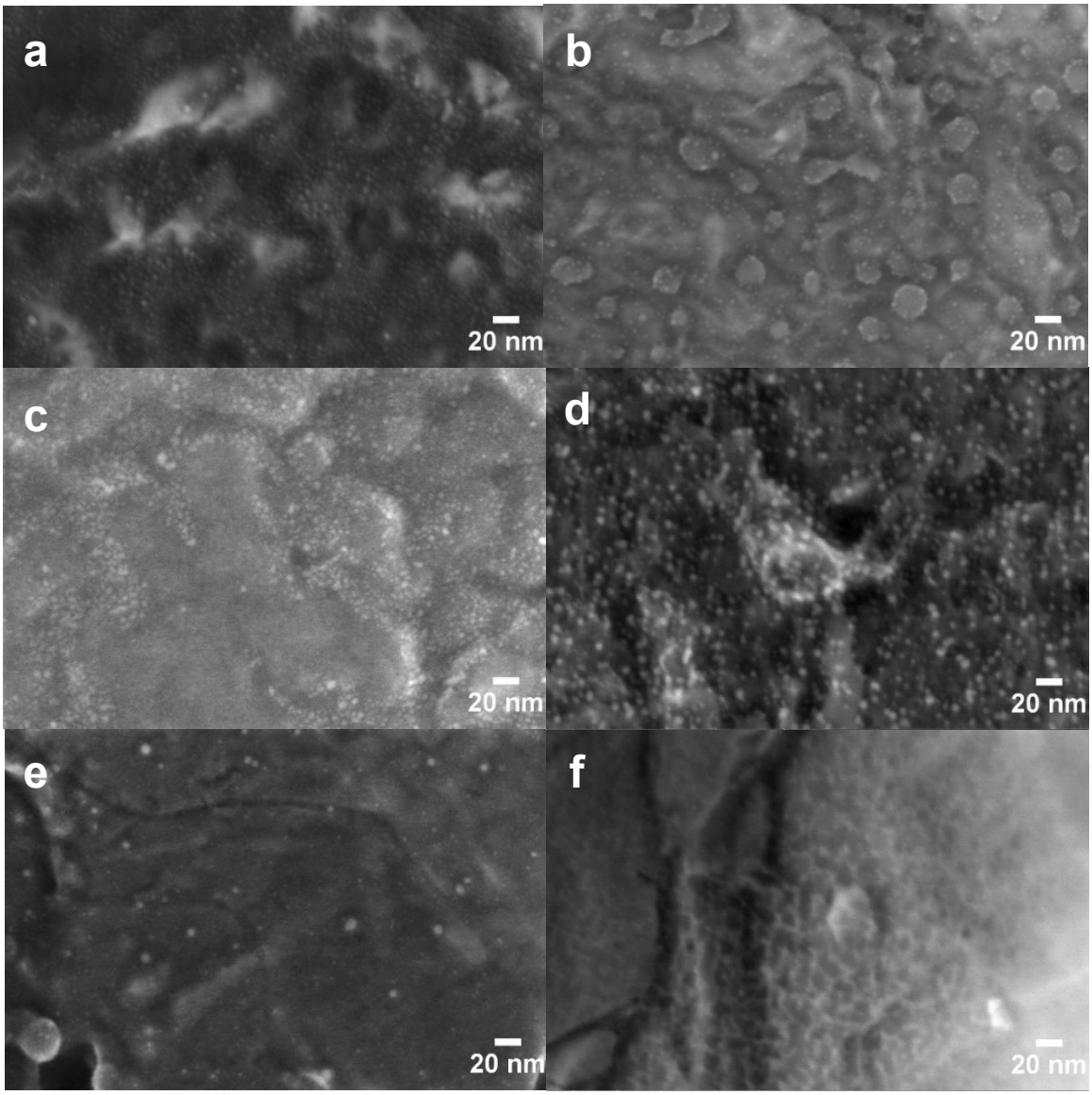

Figure 5.1. SEM images of the various Ag-Au nanoparticle catalyst compositions bound to BDD through an undecenethiolate linker, : a) Ozone treated UDT-AuNP-BDD, b) UDT-AgNP-BDD, c) Ag-AuNP-BDD (UPD method, Ag:Au ratio = 0.26), d) Ag-AuNP-BDD (anti-galvanic reduction method, Ag:Au = 0.48), e) Au-AgNP-BDD (Au:Ag = 0.02), and f) Au-AgNP-BDD (Au:Ag = 6.8). Images a-b show that grafting the UDT-AuNPs or UDT-AgNPs resulted in an evenly dispersed monolayer of NPs evidenced by the small white dots, and images c-e demonstrate that no significant change in the size or morphology of the NP cores occurred upon addition of Ag or Au. Image f shows that the AgNP cores began to destabilize when a significant amount of Au was added.

when Ag was added to the AuNP surface through either the UPD method or anti-galvanic reduction method (Figure 5.1c, 1d). Qualitatively, no core size growth was observed,

suggesting that thick shells of Ag are not depositing onto the AuNP surface in the **Ag-AuNP-BDD** samples. When Au was added to the AgNPs in a very small amount to prepare **Au-AgNP-BDD** (Au:Ag ratio ~ 0.03), no noticeable change in the AgNP morphology was observed in the SEM images (Figure 5.1e). However, when a larger amount of Au was added to the AgNPs (Au:Ag ratio ~ 8), the morphology changed from spherical nanoparticles to a more nanostructured network (Figure 5.1f). This is consistent with previous reports of galvanic exchange of silver nanoparticles with gold where etching and hollowing of the Ag nanostructures has been observed.[30,31]

Assessing the ability of the monometallic and bimetallic gold and silver nanoparticle modified electrodes to be oxygen electroreduction electrocatalysts in alkaline conditions. Rotating ring disk electrode voltammetry (RRDE) was used to assess the electrocatalytic ability of the nanoparticle electrodes towards the oxygen reduction reaction (ORR). Any hydrogen peroxide byproduct produced at the disk electrode (i.e., the tethered NP electrocatalysts) can be detected at the ring electrode, which provides direct evidence into the pathway by which ORR is occurring on these electrocatalysts, either direct, four-electron reduction (Equation 1), or indirect, two-electron reduction (Equations 2 and 3).

$$O_2 + 2H_2O + 4e^- \rightarrow 4OH^- \qquad (1)$$

$$O_2 + H_2O + 2e^- \rightarrow HO_2^- + OH^- \qquad (2)$$

$$HO_2^- + H_2O + 2e^- \rightarrow 3OH^- \qquad (3)$$

The **Ag-AuNP-BDD** electrodes were observed to catalyze ORR primarily through a direct, four-electron pathway in base (Figure 5.2). Only one ORR reduction event was observed for all of the **Ag-AuNP-BDD** samples with an onset at ~0.94 V vs. RHE. As the

amount of silver was increased on the surface, the ring current (i.e., peroxide product) decreased, indicating that the addition of silver was shifting the ORR pathway from indirect, two-electron to direct, four-electron. This is in contrast to the AuNPs alone (**UDT-AuNP-BDD**) which resulted in significant ring currents. Furthermore, the shape of the disk voltammogram exhibited two reduction events (onsets at 0.95 V and 0.05 V vs. RHE) unlike the **Ag-AuNP-BDD** samples which have one clear reduction event, providing evidence that AuNPs of this size alone can only catalyze ORR via the indirect, two-electron pathway. Since BDD is a poor electrocatalyst for ORR (Figure C9) in the potential window of interest, the observed electrocatalytic activity is from the NP electrocatalysts.

To ensure that the disk current was a result of ORR, a control experiment was performed where the 0.1 M KOH electrolyte was sparged with argon instead of oxygen and the RRDE measurement was collected (Figure C10). No significant current was measured in the potential window of interest with an argon sparged electrolyte, indicating that the electrocatalytic activity measured is a result of a reaction with oxygen.

The overpotentials of the **Ag-AuNP-BDD** ORR electrocatalysts are comparable to what is reported for other Ag-Au nanoparticles of this structure, and are very close to that observed with Pt/C electrocatalysts.[16] While Au and Ag are still noble metals, they are cheaper than Pt, and the use of the nanoparticle helps increase the active surface area and minimize the total amount of metal that has to be used. The **Ag-AuNP-BDD** electrodes were also observed to be stable over the course of 30 minutes being held at a constant reducing potential (-0.39 V vs. RHE) with minimal decrease in the disk current and no increase in the ring current (Figure C11).

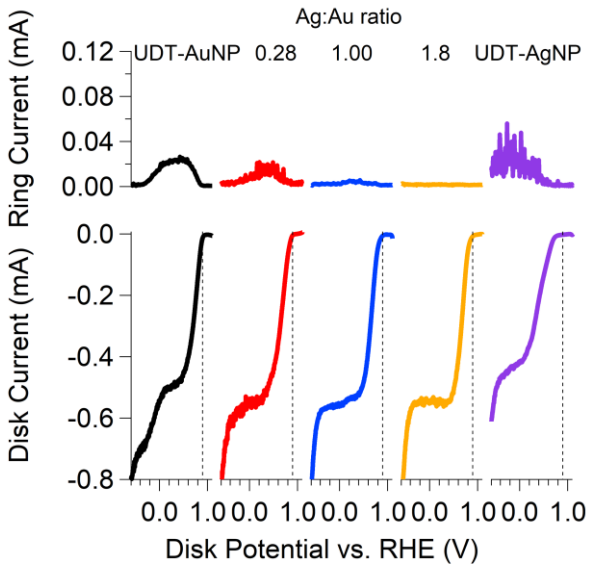

Figure 5.2. Comparison of the rotating ring disk voltammograms of Ag-AuNP-BDD, UDT-AuNP-BDD, and UDT-AgNP-BDD in O_2 saturated 0.1 M KOH. All samples were measured at a scan rate of 20 mV/s while rotating at 500 rpm. The dashed lines at 0.9 V vs. RHE are to facilitate comparison between samples.

Despite the observation that increasing the amount of Ag on the AuNP surface improved the ORR activity, 2.5 nm AgNPs alone (**UDT-AgNP-BDD**) were not good ORR electrocatalysts (Figure 5.2). RRDE measurements on **UDT-AgNP-BDD** revealed a reduction event at a higher overpotential (0.77 V vs. RHE) that generated peroxide as evidenced by significant ring currents. The overpotential observed with the 2.5 nm **UDT-AgNP-BDD** samples is comparable to previously reported overpotentials of larger monometallic AgNPs.[17] The peroxide intermediate generated by **UDT-AgNP-BDD** was not further reduced until -0.5 V vs. RHE. This indicates that AgNPs alone were only able to catalyze the indirect, two-electron ORR pathway in contrast to the **Ag-AuNP-BDD** samples which were observed to directly reduce oxygen to hydroxide. This suggests that the Ag deposited on the AuNP surface in **Ag-AuNP-BDD** is different in some way (structurally or electronically) than the Ag on the surface of the AgNP cores.

A series of control experiments were performed to determine if the AuNP core was necessary to produce the enhanced ORR activity, or if the deposition process used to fabricate **Ag-AuNP-BDD** might form active Ag catalytic sites on other surfaces. To investigate if active Ag catalytic sites could be deposited on other NP core materials, a **UDT-AgNP-BDD** sample was put through the same process used to deposit silver onto AuNP surface through the UPD method. The ORR activity was unchanged compared to the UDT-AgNPs that had not been treated (Figure C12a). A bare BDD substrate was also put through the process of UPD and galvanic exchange used to fabricate the Ag-AuNP-BDD samples to see if catalytically active silver was deposited on the surface (**BDD-UPD**). Only a very small Ag 3d signal was detected by XPS (Table 5.1), as expected since Cu is not predicted to deposit on BDD at an underpotential, and no significant improvement in the ORR activity was observed with **BDD-UPD** compared to bare BDD (Figure C12b). Finally, while no significant Cu 2p signal was detected by XPS in these samples after galvanic exchange, the potential influence of trace copper remaining from the deposition process on ORR activity was investigated. Copper was deposited on a **UDT-AuNP-BDD** sample using the UPD method resulting in a Cu:Au ratio of 0.022 ± 0.001. No improvement in the ORR activity compared to untreated **UDT-AuNP-BDD** was observed, indicating that trace copper is not responsible for the ORR activity (Figure C13). This set of control experiments suggests that there are unique interactions between the Ag and the 2 nm AuNP core in **Ag-AuNP-BDD** that creates an active ORR catalyst.

If the enhanced ORR catalytic activity observed in **Ag-AuNP-BDD** is simply a result of having Au and Ag atoms near each other, it would be expected that adding Au back to a AgNP core would also result in improved ORR activity. However, adding Au

to AgNPs via galvanic exchange (**Au-AgNP-BDD**) did not result in ORR activity comparable to the **Ag-AuNP-BDD** catalysts. The sample with the higher Au:Ag ratio (~8), while slightly improved from **UDT-AgNP-BDD**, was significantly worse at catalyzing ORR than that of the **Ag-AuNP-BDD** samples (Figure C14). The ring currents were significantly higher than **Ag-AuNP-BDD** and two reduction events were measured. The SEM image of samples with higher Au:Ag ratios (Figure 5.1f) showed that the Ag core was somewhat destabilized during the galvanic exchange process which would prevent a perfect comparison to the **Ag-AuNP-BDD** samples. However, the sample with the smaller Au:Ag ratio (~0.03) demonstrated worse ORR activity than the AgNPs alone with lower disk currents and higher reduction onset potential (Figure C14) despite the preservation of the AgNP spherical morphology (Figure 5.1e). The onset of reduction was shifted ~150 mV more negative than that reported by Chen and co-workers for their ~6 nm Janus Au-AgNPs (AgNP core, Au shell).[17] These results suggest that simply having the Au and Ag atoms in close proximity is not enough to produce the enhanced ORR activity observed in the **Ag-AuNP-BDD** samples.

Examining the structure and composition of the Ag-AuNP-BDD ORR electrocatalysts after electrochemical measurements. Electrochemical measurements can alter the structure and composition of multimetallic nanoparticle catalysts through inducing processes such as etching/dissolution of one of the metals or ligand desorption which can result in rearrangement or core fusion of the nanoparticles on the electrode surface. To determine if Ag is being etched away during electrocatalytic screening, three of the **Ag-AuNP-BDD** samples were examined by XPS after rotating ring disk voltammetry measurements were taken (Table C1). No significant change in the Ag:Au

ratio was observed after electrochemical measurements were performed, suggesting that both Au and Ag were present and involved in ORR electrocatalysis (i.e., Ag was not being etched away). A significant decrease in the S 2p XPS signal suggested that a large portion of the undecenethiolate ligands were lost during electrochemical measurement as well. In all samples, a decrease in the Au:$C_{284.8}$ ratio was observed that suggests that some NPs are being lost during the initial electrochemical measurements. However, the ORR electrocatalytic activity was observed to be stable over many cycles and when held at a constant reducing potential for 30 minutes, indicating that this loss of NPs and ligands likely happened initially during the first cycle, and did not continuously occur.

The structure of the **Ag-AuNP-BDD** catalysts was also examined by SEM after electrochemical measurements. There was an evident change in how the NPs were arranged on the electrode after ORR screening, with the NPs no longer in an evenly dispersed monolayer, but instead were arranged into an elongated nanostructure, approximately ~5-10 nm in width (Figure 5.3a). This rearrangement was also observed with both **UDT-AuNP-BDD** and **UDT-AgNP-BDD**, indicating this effect is not unique to the **Ag-AuNP-BDD** samples (Figure C15). This rearrangement could be induced by the loss of the thiolate ligands during ORR electrocatalytic screening. Due to the resolution limit of the SEM, it is unclear if the NP cores fused or if they simply aggregated together.

To further investigate the effect of NP aggregation into larger structures on ORR performance, a set of larger Ag-AuNPs were deliberately made to investigate their ORR activity. These larger Ag-AuNPs were of similar size to the nanostructures measured by

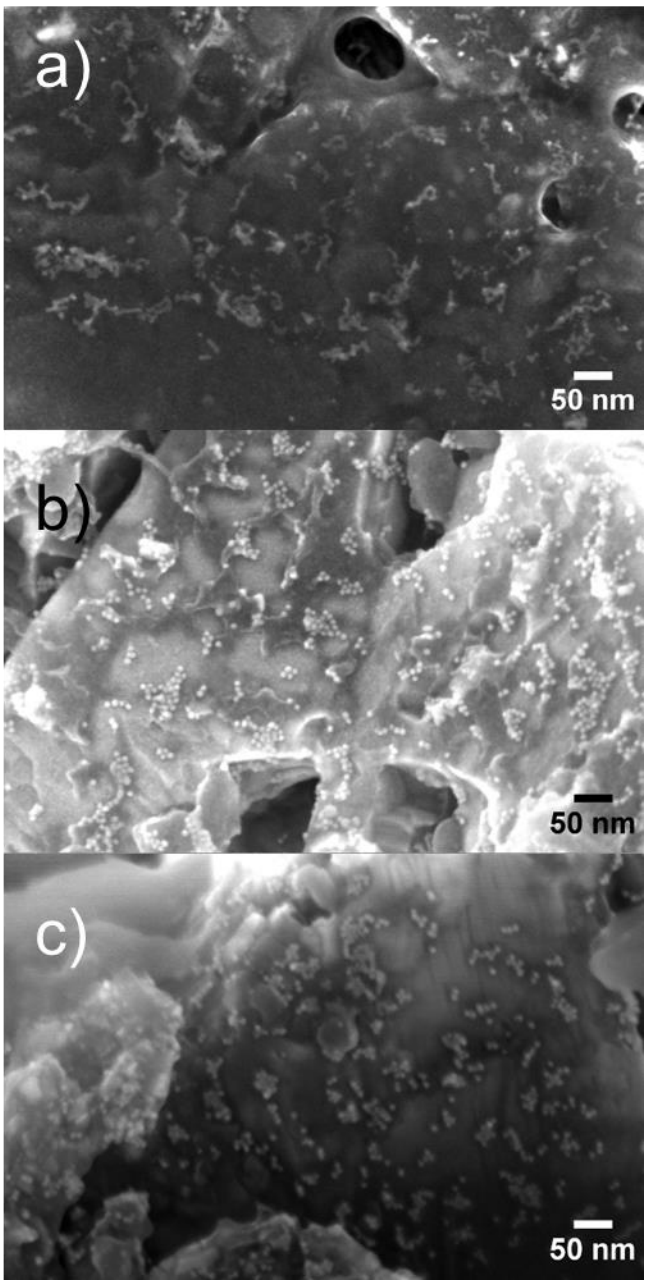

Figure 5.3. SEM images of Ag-AuNP-BDD made with 2 nm AuNP cores after electrochemical measurement (a), Ag-AuNP-BDD made with larger AuNP cores (b), and larger Ag-AuNP-BDD after electrochemical measurement (c), showing similarly sized nanostructures (~5-10 nm in width).

SEM after electrochemistry for the smaller **Ag-AuNP-BDD** samples to determine if larger Ag-AuNPs could efficiently catalyze ORR, or if the smaller 2 nm Ag-AuNPs were needed to maintain effective ORR activity. To fabricate larger Ag-AuNPs, citrate

stabilized AuNPs (~10 nm) were assembled onto heptane-thioacetate-functionalized BDD and then Ag was added to their surface using either the UPD/galvanic exchange method or anti-galvanic reduction method. The ORR activity of the larger Ag-AuNPs was then compared to the smaller Ag-AuNPs that with similar Ag:Au ratios. SEM images showed that the larger AuNPs were also attached to BDD in a submonolayer and retained their spherical morphology upon addition of Ag (Figure 5.3b). The ORR activity of citrate AuNPs alone (Figure 5.4a), and Ag-modified citrate AuNPs with XPS Ag:Au ratios of 0.65 (Figure 5.4b) and 1.0 (Figure 5.4c) were compared to the smaller 2 nm AuNPs with similar Ag:Au ratios. In all cases, the larger AuNPs were worse ORR electrocatalysts than their 2 nm AuNP analogues, indicated by their shifted reduction onset potentials and significant ring currents, even when comparable amounts of Ag were added to their surface (Figure 5.4b, c). Some aggregation of the larger Ag-AuNP cores is observed after electrochemical measurements (Figure 5.3c), similar to that of the 2 nm Ag-AuNPs. These results suggest that despite the aggregation of the smaller Ag-AuNPs into larger nanostructures during ORR electrocatalysis, they possess a uniquely reactive surface.

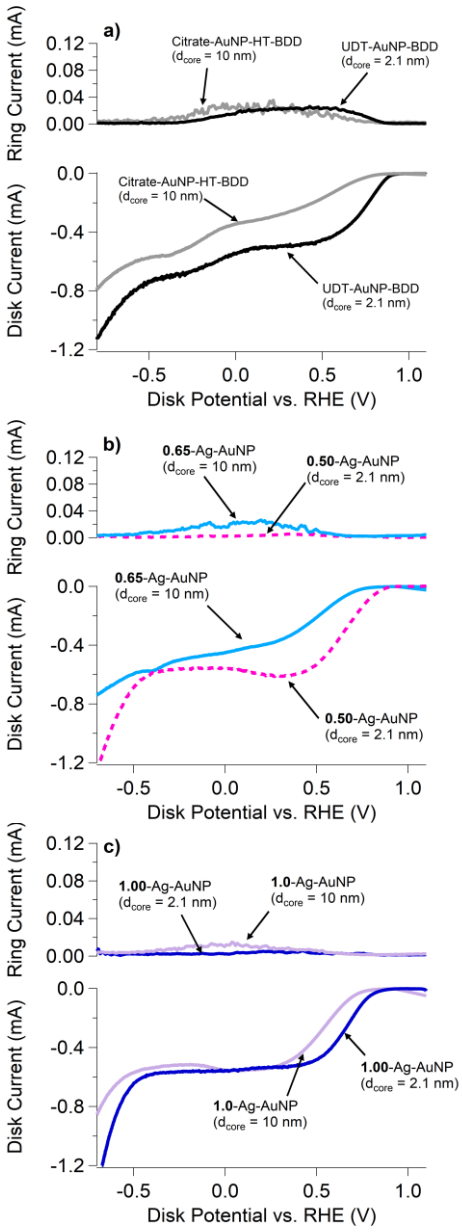

Figure 5.4. Rotating ring disk voltammograms in O_2 saturated 0.1 M KOH used to compare ORR activity between a) smaller (d_{core} = 2.5 nm) and larger (d_{core} = 10 nm) AuNPs with no Ag added, b) Ag:Au ~ 0.5, and c) Ag:Au ~ 1. In all cases, the larger AuNP cores were worse four-electron ORR catalysts than the smaller AuNP cores as seen by larger overpotentials and ring current values, despite having comparable amounts of Ag on the surface. All samples were measured at a scan rate of 20 mV/s while being rotated at 500 rpm.

Hypotheses for the enhanced ORR activity of Ag-AuNP-BDD electrocatalysts in alkaline conditions. While the unique activity of the **Ag-AuNP-BDD** ORR electrocatalyst compared to other Ag and Au structures evaluated in this work is not fully understood at this time, there are several hypotheses that can be considered. In multimetallic catalysts, the catalytic activity is often attributed to synergistic effects between the different metals such as electronic interactions between the metals, the presence of multimetallic active sites, and/or one of the metals acting as a template to structure the other metal(s) in a unique way that renders it more catalytically active. The possible contribution of each of these effects will be discussed below for the **Ag-AuNP-BDD** system in relation to its ORR activity.

Electronic interactions between Ag and Au. The catalytic activity of multimetallic electrocatalysts has been partially attributed to electronic interactions between the different metals.[17,18,29] The binding energy shifts of both Ag and Au observed in the **Ag-AuNP-BDD** samples compared to their monometallic nanoparticle counterparts indicate that there were electronic interactions between the two metals. In general, the Ag 3d binding energy was observed to shift more negative (~0.3 eV) and the Au 4f binding energy was shifted more positive (~0.2 eV), suggesting that Au is acting as an electron donor to Ag. Silver has been previously reported to act as an electron acceptor in other bimetallic NP systems including AuNPs possessing a Ag semi-shell[16] and Pt-AgNPs (alloyed and core-shell structures).[29] The ORR activity of these structures was primarily attributed to this charge transfer from the metallic core to the Ag shell. It is possible that this charge transfer from the AuNP core to the Ag shell is contributing to the enhanced ORR activity in the **Ag-AuNP-BDD** system. However, similar binding

energies were observed with the larger 10 nm Ag-AuNPs indicating that Au was also acting as an electron donor in this system (Figure C8), but these larger Ag-AuNPs did not exhibit the same ORR activity as their smaller analogues (Figure 5.4b, c). Electronic interactions are also evident in the **Au-AgNP-BDD** samples described in this work when higher ratios of Au were used. In those samples, the Au 4f binding energies were shifted more positive (~0.3 eV) and Ag 3d binding energies were shifted more negative (~0.7 eV), still suggesting that Au acts as an electron donor to Au, but these samples were also not active ORR catalysts (Figure C14). This is in contrast to other Janus structured Au-AgNPs (AgNP core, Au semi-shell), where it was reported that Ag acted as an electron donor to Au.[17] This could suggest either that there is an ideal binding energy for both Au and Ag to promote ORR electrocatalysis or that electronic interactions are not solely responsible for the enhanced ORR activity observed with the **Ag-AuNP-BDD** catalysts.

Structural effects: bimetallic active sites or templating effects. Precisely determining the structure of the **Ag-AuNP-BDD** electrocatalyst is limited by the small size of these Ag-AuNPs and the fact that they are tethered to an electrode. However, the probability of these structural attributes influencing the **Ag-AuNP-BDD** system can still be considered. One possibility is that addition of Ag to the AuNP surface produces active bimetallic sites for oxygen to bind. To consider the likelihood of Ag-Au bimetallic sites in this system, one can estimate the amount of Ag that would be needed to form a complete monolayer on the AuNP surface and compare it to the amount of Ag measured by XPS. Assuming all NPs are spherical, monodisperse in core size, and that Ag is able to deposit on the entire AuNP surface, it was calculated that a full monolayer of Ag would yield a Ag:Au ratio of ~0.3. All **Ag-AuNP-BDD** samples measured in this work

had a XPS Ag:Au ratio of close to 0.3 or higher, suggesting that if Ag deposited in a monolayer on the AuNP surface, it is unlikely that there was a large proportion of bimetallic sites that served as ORR active sites and it is more likely that the **Ag-AuNP-BDD** samples possess a core-shell or semi-shell/Janus structure with the portion of ligands that serve as the interface to the BDD electrode protecting a small portion of the AuNP core from modification by Ag. This is further supported by the comparable ORR activity of the **Ag-AuNP-BDD** system to the core-shell and Janus/semi-shell Ag-AuNPs previously reported in literature.[16,17] However, it must be considered that Ag might not have deposited in a monolayer on the AuNP surface, and instead produced Ag clusters or nodules while leaving a portion of the AuNP surface unmodified. It has been reported that when Cu is underpotentially deposited on AuNP surfaces, an incomplete monolayer with evidence of Cu clusters is produced in contrast to the monolayer of Cu that is formed on planar Au surfaces.[26] While no obvious shape changes indicative of larger Ag clusters/nodules on the AuNP surface were observed in the SEM images of the nanoparticles before (Figure 5.1a) and after Ag deposition (Figure 5.1c, d), further structural analysis would be needed to determine if Ag is completely coating the nanoparticle surface or if it is depositing in clusters in the **Ag-AuNP-BDD** system providing potential bimetallic active sites.

From this work, it seems probable that the small AuNP core is facilitating the formation of a catalytically active Ag shell on its surface. The lack of ORR activity of both **UDT-AgNP-BDD** as well as a **UDT-AgNP-BDD** sample put through the Ag deposition process used to modify the AuNPs suggests the necessity of the 2 nm AuNP core to produce the ORR active catalyst. The lack of ORR activity with the **Au-AgNP-**

BDD system demonstrates that simply having Ag and Au in close proximity is not enough to produce good ORR activity. The enhanced ORR activity observed when adding Ag to the surface of 2 nm AuNPs compared to 10 nm AuNPs suggests that the smaller AuNP core allows Ag to be structured in a more catalytically active form. While the electronic interactions between Ag and Au are clearly present and cannot be completely disregarded, this work has shown that they are unlikely solely responsible for the enhanced ORR activity. Further work would need to be done to fully elucidate the structure of the catalytically active sites.

Conclusions

A series of silver-gold bimetallic nanoparticles bound to boron doped diamond electrodes through an alkanethiolate interface were evaluated for their electrocatalytic performance for ORR in alkaline conditions. Silver deposited onto the surface of 2 nm undecenethiolate stabilized-AuNPs tethered to BDD (**Ag-AuNP-BDD**) were significantly better catalysts for the direct, four-electron ORR pathway compared to grafted monometallic UDT-AuNPs or UDT-AgNPs or than gold added to grafted 2 nm UDT-AgNPs (**Au-AgNP-BDD**). From the amount of silver measured by XPS on **Ag-AuNP-BDD**, it seems probable that the AuNP core is completely covered by silver, suggesting that the gold core is not directly involved in catalysis, but is influencing the electronic and structural properties of the silver creating an efficient catalyst. However, larger 10 nm AuNPs with silver deposited on their surface were not as effective ORR catalysts indicating that a smaller AuNP core is required to create an active bimetallic catalyst and that electronic interactions are not solely responsible for the observed ORR activity in these Ag-Au bimetallic NP systems.

These methods to fabricate Ag-AuNPs allowed for a series of compositions to be rapidly made and evaluated, while preserving a defined NP-electrode structure, namely keeping the NP core size and shape intact across compositions while maintaining the molecular interface between the NP and the boron doped diamond electrode. The use of boron doped diamond, a catalytically inert electrode support, allowed for the ORR catalytic activity of the Ag-AuNPs to be measured without any competing effects from the support. This approach can be considered an alternative method to creating core-shell or semi-shell/Janus nanoparticle catalysts comparable to the best Ag-Au nanostructured ORR catalysts reported in the literature. From this work, further insight into the influence of metallic placement and core size on the ORR electrocatalytic properties of bimetallic Ag-AuNPs was gained. This work demonstrates that simply having two elements in close proximity is not enough to induce catalytic activity and highlights the importance of considering the structure of multimetallic NP catalysts. Furthermore, the observation of change in morphology of the NP-functionalized electrode after electrocatalytic screening indicates that the interactions between nanoparticles and the influence of electrochemistry on nanomaterials should be taken into account when determining the catalytically active structure.

These results demonstrate the importance of considering the subnanometer NP structure and composition, the NP core size and interface to the electrode, and the influence of electrochemistry on the overall NP catalyst structure when designing new multimetallic nanoparticle electrocatalysts. This platform provides the opportunity to study other well-defined multimetallic NP electrocatalysts with the numerous other

metals that are reported to be compatible with underpotential deposition, galvanic replacement, and/or anti-galvanic reduction.

Bridge to Chapter VI

Chapter V demonstrated how this platform can be used to incorporate multimetallic nanoparticles and gain insight into how the subnanometer structure and composition of the nanocatalyst influences its electrocatalytic activity. Chapter VI summarizes the key findings of this dissertation and provide an outlook to future applications of this work towards designing improved nanoparticle-functionalized electrodes for important applications.

CHAPTER VI

CONCLUSION

Note: Portions of this chapter are expected to appear in an upcoming publication co-authored by Samantha L. Young, Jaclyn E. Kellon, Tawney A. Knecht, and James E. Hutchison. J.E.K. and I equally contributed to the writing of this chapter. T.A.K. provided assistance in compiling references and editorial support. J.E.H. provided editorial support and advice in conceptualizing this work.

Outlook

Advances in the synthesis and characterization of nanomaterials, as well as the development of more efficient reaction chemistry, have provided the opportunity to create advanced nanomaterial-functionalized surfaces. As this field continues to develop, there are several areas that will likely be important. While much of the work so far has been focused on tethering noble metal NPs or semiconductor quantum dots, there is interest in investigating more earth abundant materials for applications such as electrocatalysis and photochemical energy conversion. Development of new tethering chemistries to couple materials such as metal oxide nanoparticles to electrodes while maintaining efficient electronic communication will be a next step in the field as precision syntheses of these materials are being established.[1]

While synthetic techniques to create advanced nanomaterials is being developed, another opportunity to access these structures is through modification of nanomaterials after attachment to electrode surfaces. Methods such as underpotential deposition, galvanic exchange, and anti-galvanic reduction that have previously been studied

extensively with planar electrode surfaces are beginning to be used to modify NP surfaces to create multimetallic NPs.[2–4] This approach allows for the quick screening of different elemental compositions and potential access to nanomaterials that may be challenging to synthesize through traditional synthetic methods. Another approach to access nanomaterials that are challenging to synthesize through traditional batch chemistry methods is the electrodeposition of nanomaterials onto a molecularly functionalized electrode. While traditional electrodeposition syntheses of NPs onto unfunctionalized electrodes can suffer from disperse core sizes and an ill-defined interface, deposition onto a molecular monolayer could provide more control over these variables. Currently, this method is mostly used to produce noble metal nanomaterials such as AuNPs[5,6] and bimetallic Ag/AuNPs.[7] By modifying existing methods that yield a defined NP-electrode interface for the electrodeposition of other nanomaterials, a new class of nanomaterials could be more precisely synthesized and studied for their electrochemical properties.

In addition to creating new nanomaterials, methods to precisely control the coverage of nanoparticles on an electrode surface will be important. The loading of a nanomaterial on an electrode substrate has been observed to influence product selectivity for electrocatalytic reactions.[8,9] By increasing the NP coverage, the probability of reaction intermediates to diffuse to a neighboring nanoparticle and be further transformed is also increased. Incorporating multiple types of NPs on the surface can be a strategy to efficiently access products that would be challenging with a single catalyst. Improved methods to precisely control the nanomaterial coverage and construct mixed nanoparticle surface will be useful as more efficient and selective catalysts for complex reactions such

as carbon dioxide electroreduction are being developed. Beyond use of only NP(s) in the electrochemical processes, design of hybrid and nanocomposite systems that can take advantage of the functionality of the NP ligand shell and the molecular functionalization on the surface is another approach that will become more possible as this field advances.

As these synthetic and electrode fabrication methods are employed, more sophisticated analytical techniques will also be needed to continue to inform design of these materials. *In operando* x-ray techniques such as absorption spectroscopy,[10] scattering/diffraction,[11] and pair distribution function analysis[12] are helping identify catalytically active sites and structural changes in materials during electrochemistry which may not be apparent during standard ex situ measurements. Ambient pressure x-ray photoelectron spectroscopy is allowing the surfaces of materials to be observed in their operating conditions which is important for materials where typical ultra-high vacuum conditions may alter their surface chemistry.[13] Electron microscopy techniques will also be useful in assessing the nanoparticle structure. As liquid transmission electron microscopy (TEM) cells are becoming more available, electrochemical TEM measurements are being used to visualize the structure of battery materials *in operando*.[14] Through functionalization of a TEM electrode with a molecular tether that can bind NPs, multi-modal analysis can be performed for NP-functionalized electrodes.

The future is promising for the field of NP-functionalized electrodes. Significant progress has been made over the past forty years since the field of chemically modifying electrodes emerged. Through the incredible advancement of precision nanomaterial synthesis, development of tethering chemistries, understanding of electronic processes, and advancement of multi-modal analytical techniques, this interdisciplinary effort has

opened up the opportunities to create materials that will make an important impact on the technological needs of society.

APPENDIX A

SUPPORTING INFORMATION FOR CHAPTER III: SMALL GOLD NANOPARTICLES INTERFACED TO ELECTRODES THROUGH MOLECULAR LINKERS: A PLATFORM TO ENHANCE ELECTRON TRANSFER AND INCREASE ELECTROCHEMICALLY ACTIVE SURFACE AREA

Synthesis of 6-ferrocenyl(carbonyloxy)hexanethiol.

Ferrocene carboxylic acid (2.3 g, 0.01 mol) and oxalyl chloride (4.3 mL, 0.05 mol) were dissolved in 50 mL heptane. The cloudy orange solution turned a deep brown with a small amount of white precipitate after stirring for an hour. The reaction was heated to 80°C to dissolve the remaining ferrocene carboxylic acid and stirred for an additional 30 minutes. The reaction was filtered and the filtrate condensed. Unreacted oxalyl chloride was dissolved in 40 mL heptane and removed via evaporation. The resulting ferrocene acyl chloride was combined with 6-bromohexanol (1.18 g, 0.01 mol), triethylamine (2.0 g, 0.02 mol) and 75 mL dichloromethane and stirred under nitrogen for 48 hours. The crude product was purified via column chromatography using dichloromethane as the eluent. The target compound was in the second colored, fraction (0.93 g, 25% yield).

6-(ferrocenylcarbonyloxy)hexyl bromide (0.459 g, 1.2 mmol) was dissolved in 250 mL acetone. Potassium thioacetate (0.229 g, 2.0 mmol) was added to the reaction solution and the resulting suspension was stirred for 15 hours under nitrogen. The volume of acetone was reduced and the crude compound was dissolved in 80 mL of dichloromethane. The organic layer was washed with water and brine and dried over sodium sulfate. The solvent was removed via rotary evaporation to yield 6-(ferrocenylcarbonyloxy)hexyl thioacetate (0.42 g, 90% yield).

Potassium carbonate (0.327 g, 2.3 mmol) was suspended in 15 mL methanol and stirred under nitrogen for 15 minutes. A portion of 6-(ferrocenylcarbonyloxy) hexyl thioacetate (0.42 g, 1 mmol) was dissolved in 10 mL methanol and sparged with nitrogen before adding to the potassium carbonate suspension. The reaction was allowed to stir under argon for 90 minutes. Nitrogen sparged HCl (0.2 M, 20 mL) was added to the reaction and allowed to stir for 5 minutes. The crude compound was extracted into dichloromethane. The organic layer was washed with water and brine and dried over sodium sulfate. The crude compound was purified via flash column chromatography using dichloromethane as the eluent. The target compound was in the second colored fraction (red oil) (0.075g, 20% yield). ^{1}H NMR (300 MHz), $CDCl_3$ δ 4.81 (broad, 2H),

4.40 (broad, 2H), 4.20 (broad, 7H), 2.55 (q, 2H), 1.75-1.62 (broad , 4H), 1.55-1.40 (broad, 4H), 1.35 (t, 1H).

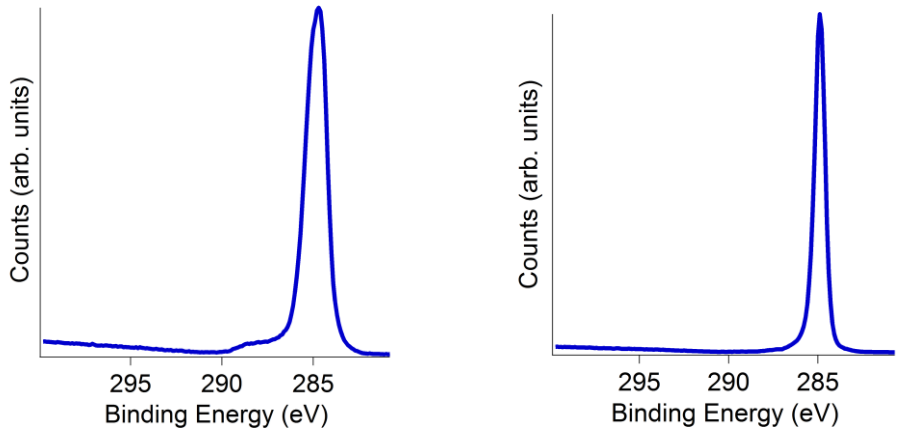

Figure A1. XPS C1s spectra of BDD before hydrogen termination (left) and after hydrogen termination (right). The sharpening of the peak at 284.8 eV and the loss of the shoulder at 288.6 eV was indicative of successful hydrogen termination of the BDD substrate.

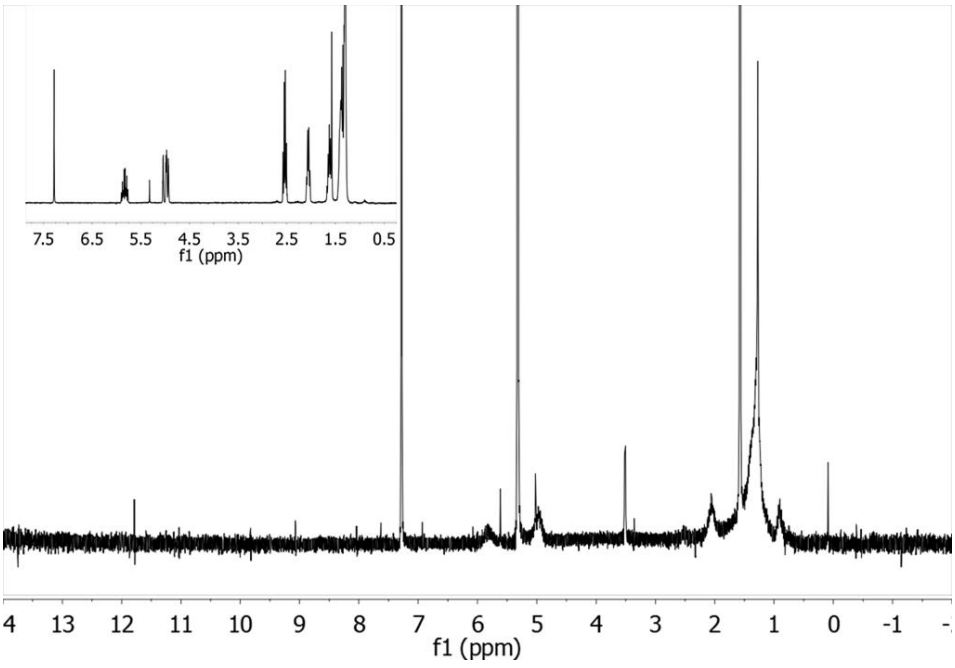

Figure A2. ^{1}H NMR of UDT-AuNPs in $CDCl_3$. Inset shows the free 10-undecene-1-thiol ligand in $CDCl_3$.

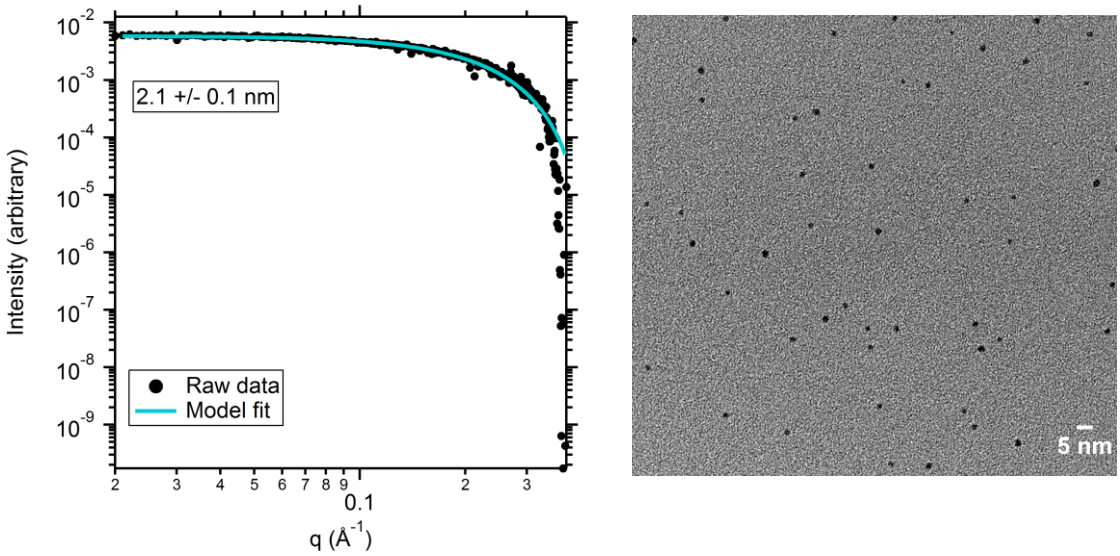

Figure A3. SAXS pattern and model fit of UDT-AuNPs dispersed in heptane (left). Bright field TEM image of UDT AuNPs to corroborate the SAXS data (right).

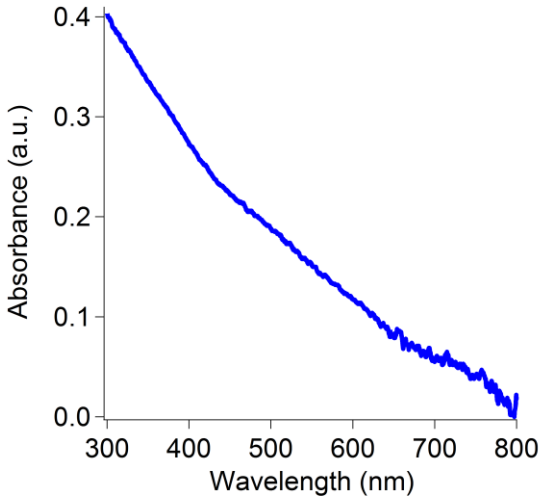

Figure A4. UV-Vis spectrum of UDT-AuNPs dispersed in heptane at the concentration used for grafting experiments, showing the absence of a sharp plasmon feature.

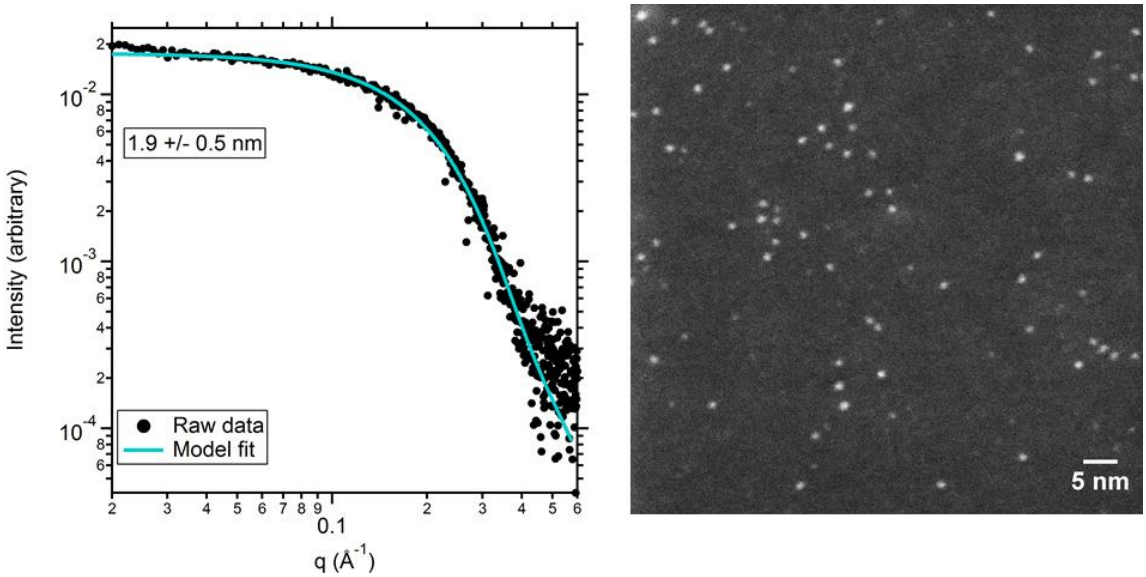

Figure A5. SAXS pattern and model fit of $Au_{101}(PPh_3)_{21}Cl_5$ dispersed in THF (left). STEM image of $Au_{101}(PPh_3)_{21}Cl_5$ to corroborate the SAXS measurement (right).

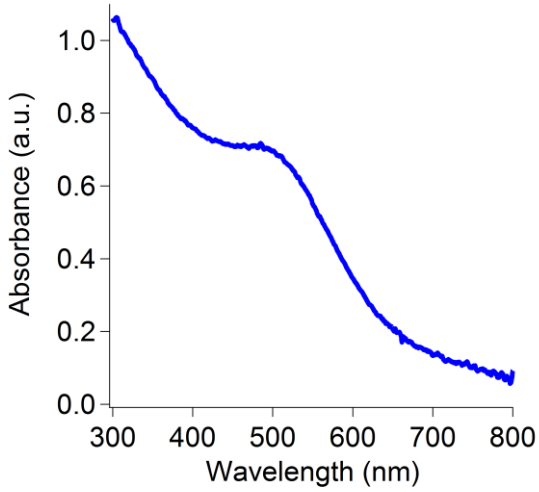

Figure A6. UV-Vis spectrum of $Au_{101}(PPh_3)_{21}Cl_5$ dispersed in CH_2Cl_2.

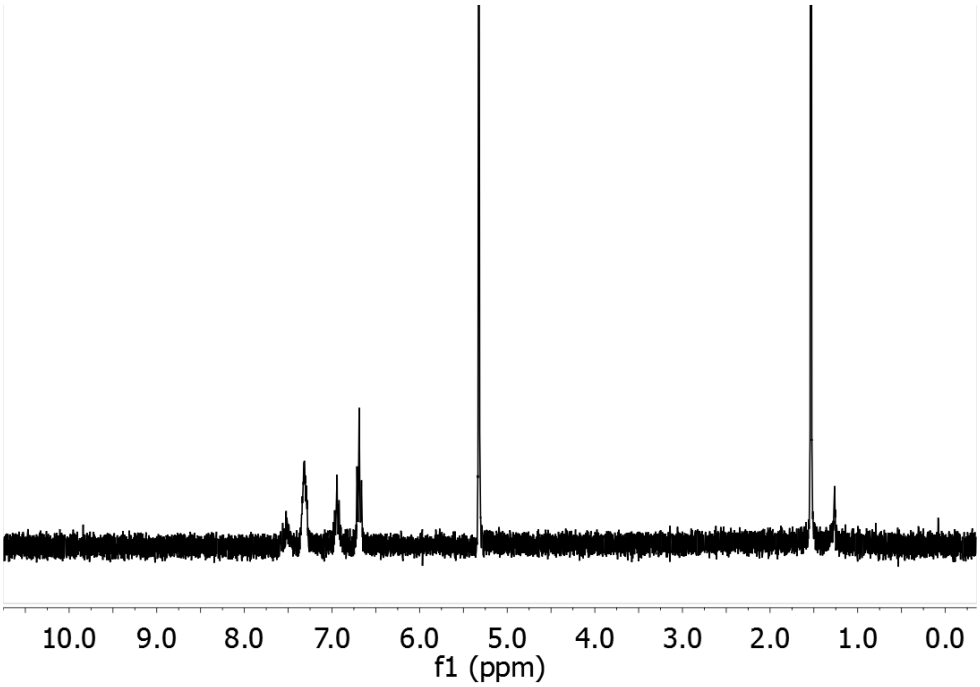

Figure A7. ^{1}H NMR of $Au_{11}(PPh_3)_8Cl_3$ in CD_2Cl_2.

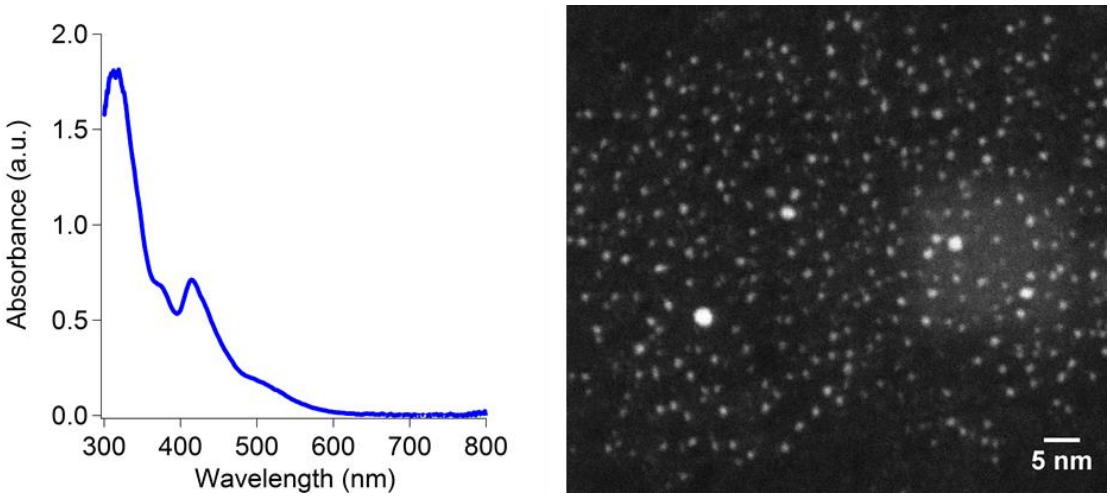

Figure A8. UV-Vis spectrum of $Au_{11}(PPh_3)_8Cl_3$ dispersed in CH_2Cl_2 (left). STEM image of $Au_{11}(PPh_3)_8Cl_3$ (right).

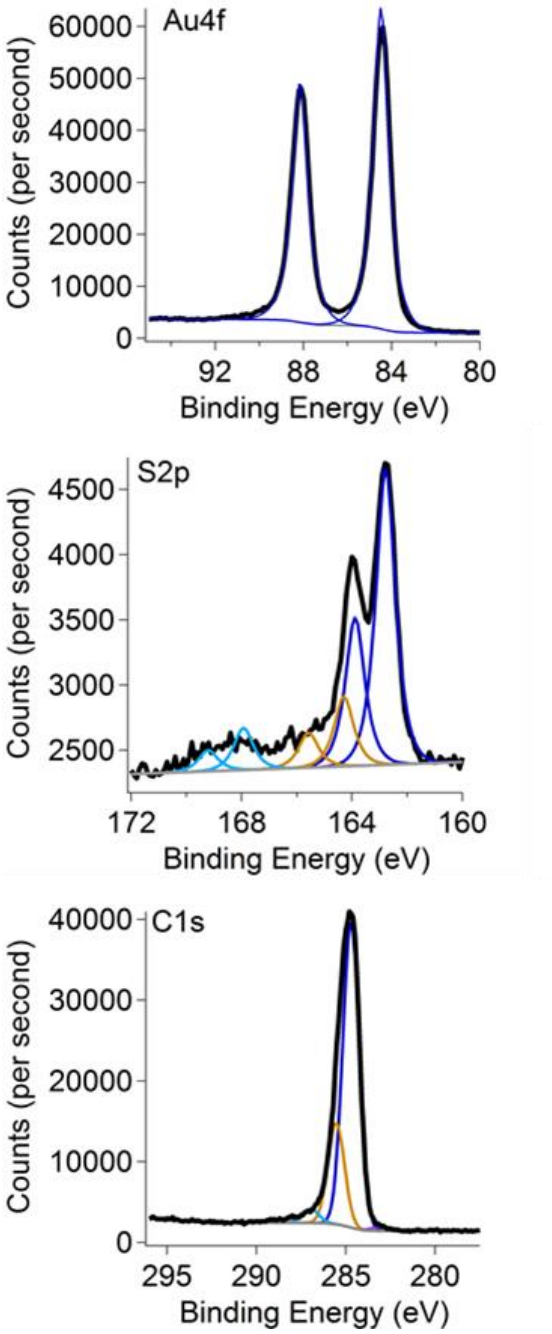

Figure A9. XPS elemental spectra (Au4f, S2p, and C1s) of **Graft-UDT-AuNP**, black trace is the experimental data and the other colored traces show the peak fitting.

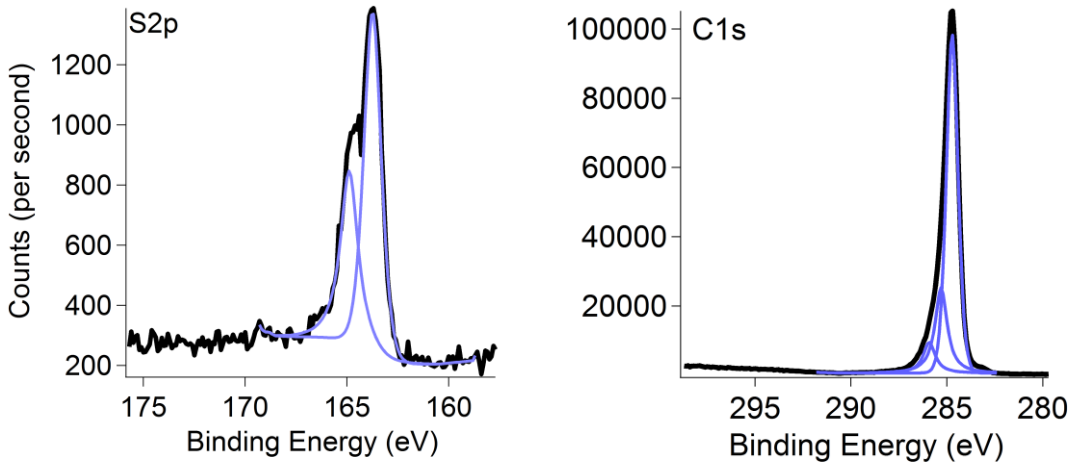

Figure A10. XPS elemental spectra (S2p and C1s) **UDTA-BDD**, black trace is the experimental data and the other colored traces show the peak fitting.

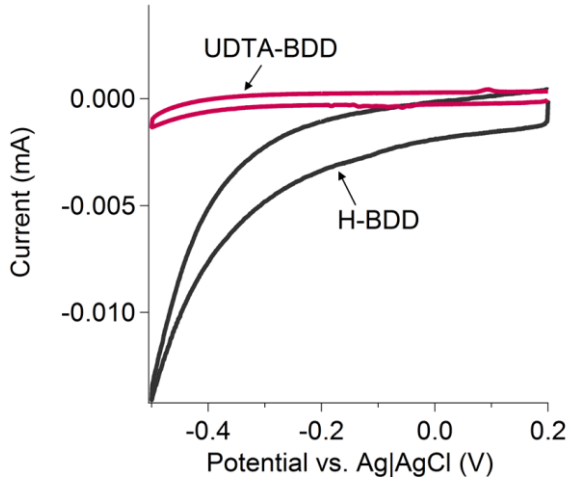

Figure A11. Cyclic voltammograms of hydrogen terminated BDD (H-BDD) and **UDTA-BDD** in 1 M KCl. The reduction in the capacitive current and suppression of the oxygen reduction current indicated that the BDD surface was functionalized by a molecular monolayer. All scans taken at 100 mV/s.

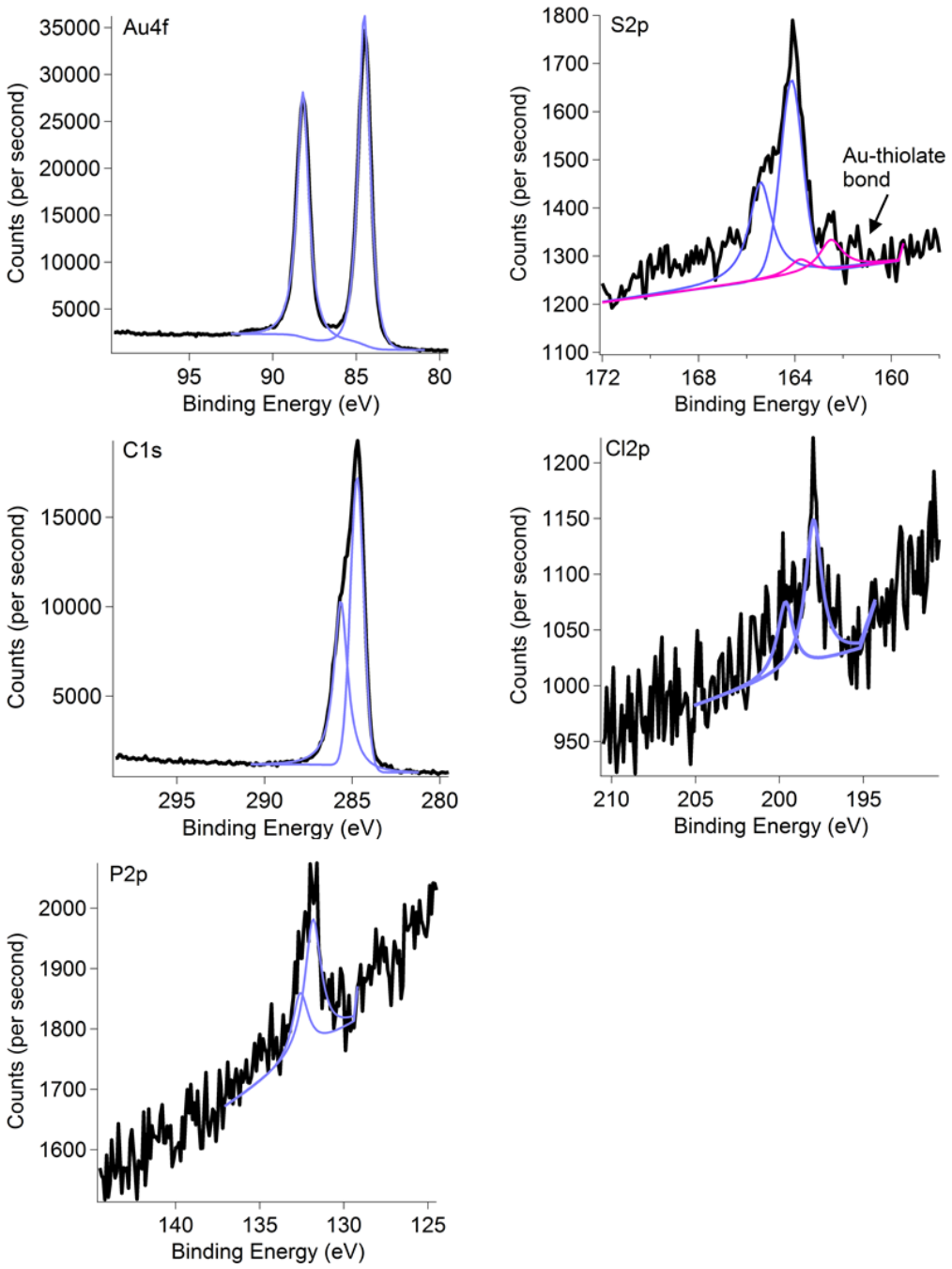

Figure A12. XPS elemental spectra (Au4f, C1s, S2p, P2p, and Cl2p of **TPP-Au$_{101}$-UDT**, black trace is the experimental data and the other colored traces show the peak fitting. The main S2p peak at 164.3 eV arises from thioacetate while the small broad hump at higher binding energy are due to a small amount of oxidized sulfur. The S2p peak could not be appropriately fit without the incorporation of the pink trace at 162.8 eV, which is indicative of a gold-thiolate bond.

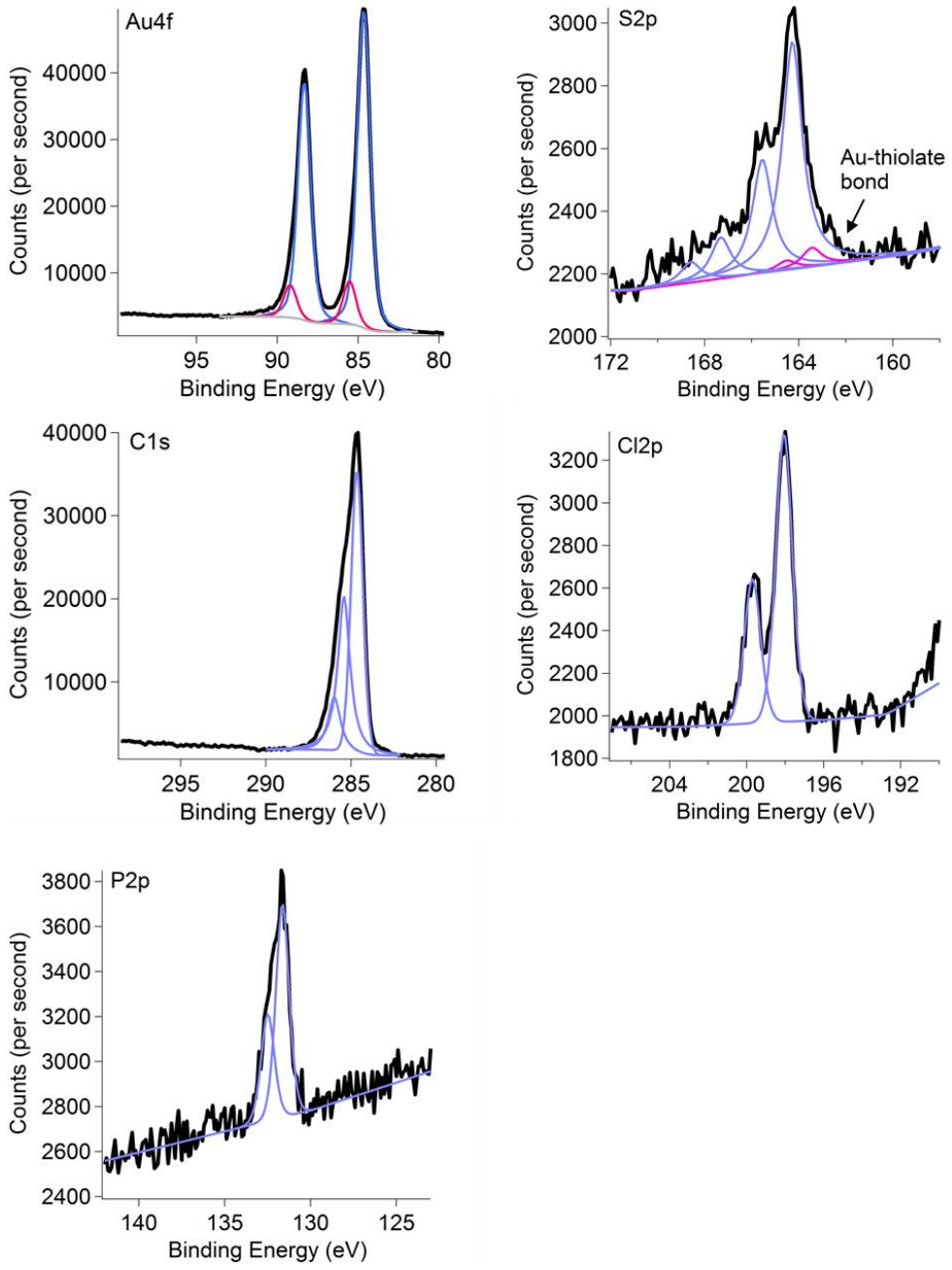

Figure A13. XPS elemental spectra (Au4f, S2p, C1s, P2p, and Cl2p) of **TPP-Au$_{11}$-UDT**, black trace is the experimental data and the other colored traces show the peak fitting. The main S2p peak at 164.3 eV arises from thioacetate while the small peaks at higher binding energy are due to a small amount of oxidized sulfur. The S2p peak could not be appropriately fit without the incorporation of the pink trace at 163.8 eV, which is indicative of a gold-thiolate bond.

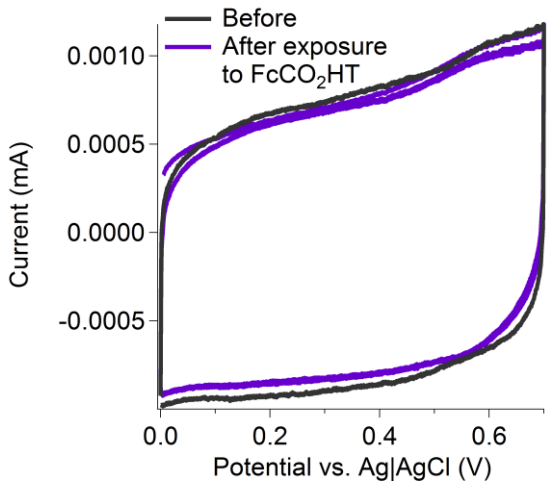

Figure A14. Cyclic voltammogram of a bare BDD substrate before (purple trace) and after treatment with dilute ozone and exposure to 1 mM $FcCO_2HT$ (gray trace), showing that $FcCO_2HT$ is not physiadsorbed to BDD. Scans in 0.1 M $HClO_4$ at 100 mV/s.

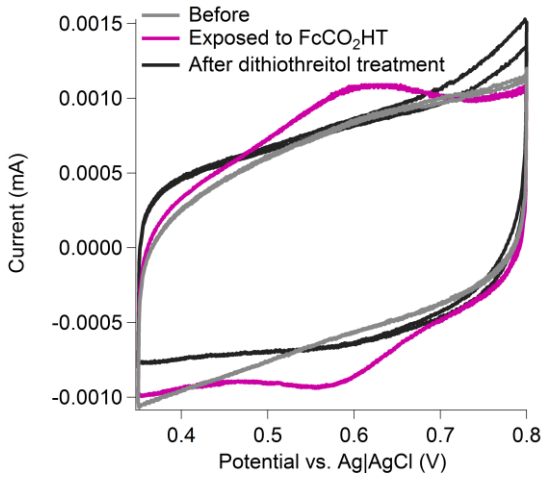

Figure A15. Cyclic voltammograms of **UDTA-BDD** (gray), after exposure to $FcCO_2HT$ (purple), then after exposing that sample to dithiothreitol (black). The small current observed after **UDTA-BDD** was exposed to $FcCO_2HT$ (purple trace), presumably due to formation of disulfide bonds between the thioacetate and the ferrocenated thiol. This hypothesis was supported by treating the sample with dithiothreitol, a disulfide reducing agent, which resulted in the suppression of the $FcCO_2HT$ current (black trace). All scans taken in 0.1 M $HClO_4$ at 100 mV/s.

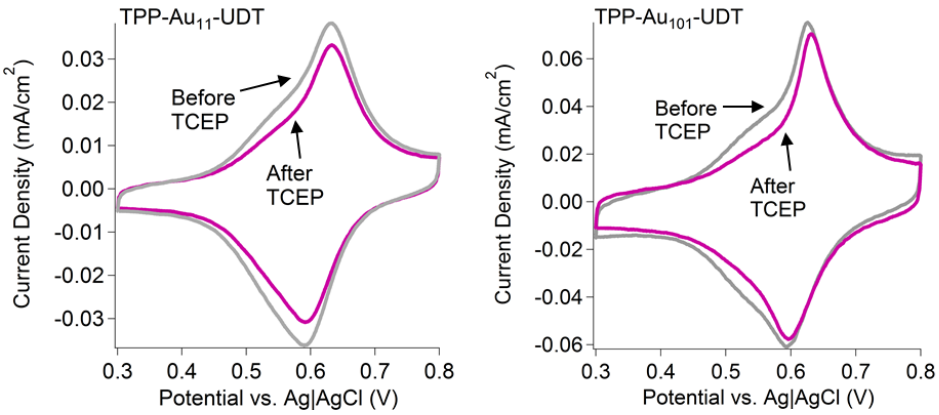

Figure A16. Cyclic voltammograms of **TPP-Au$_{11}$-UDT** (left) and **TPP-Au$_{101}$-UDT** (right) before and after treatment with TCEP. The suppression of the anodic shoulder and narrowing of the redox peaks after treatment with TCEP suggests that disulfide bonds that formed between $FcCO_2HT$ and the UDT monolayer were responsible for those features in the initial CVs.

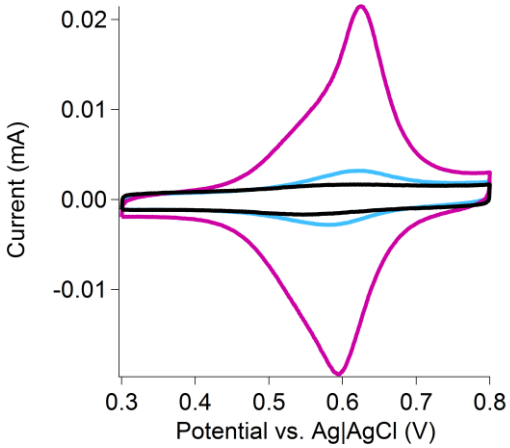

Figure A17. Overlay of cyclic voltammograms of **Graft-UDT-AuNP** as the sample went through treatments with 0.1 M KCN to decompose the AuNPs and dithiothreitol to reduce the resulting disulfide bonds. The $FcCO_2HT$ signal of the initial **Graft-UDT-AuNP** sample (purple trace) was mostly lost after treatment with 0.1 M KCN (blue trace) which indicated that the majority of the $FcCO_2HT$ is bound to the AuNP surface. The further loss of $FcCO_2HT$ signal after treatment with dithiothreitol (black trace) suggested that the signal remaining after cyanide treatment originated from disulfide bonds formed between the thiol redox probe and the undecanethiol monolayer, presumably a product of the cyanide decomposition. All scans in 0.1 M $HClO_4$ at 100 mV/s.

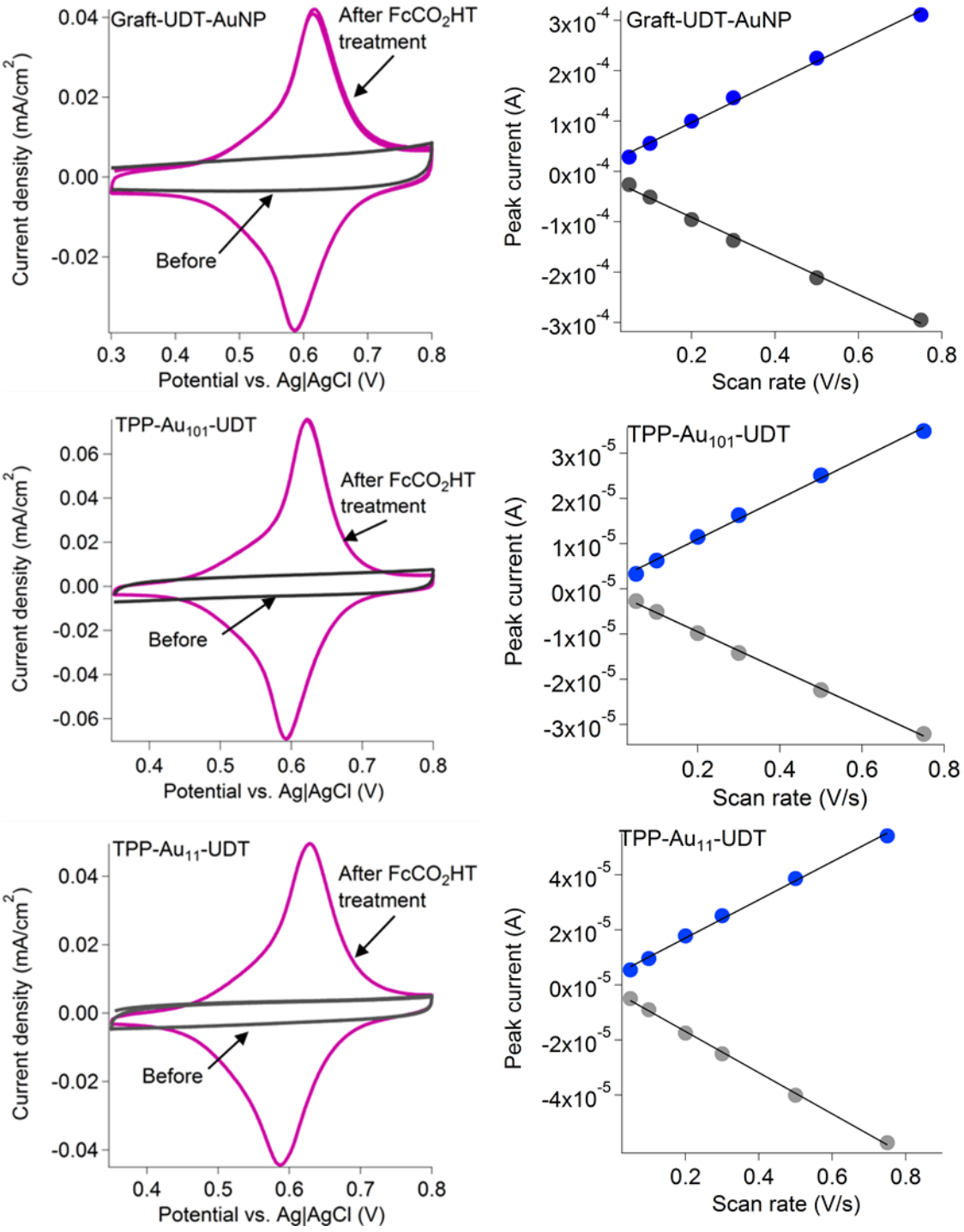

Figure A18. (Left column) Cyclic voltammograms of **Graft-UDT-AuNP**, **TPP-Au$_{101}$-UDT** and **TPP-Au$_{11}$-UDT** before (gray trace) and after attaching $FcCO_2HT$ (purple trace). Scans in 0.1 M $HClO_4$ at 100 mV/s. (Right column) Plot of the peak current as a function of scan rate for the AuNP samples treated with $FcCO_2HT$, anodic peak current (blue), cathodic peak current (gray). The linear fit is indicative of a surface bound redox probe.

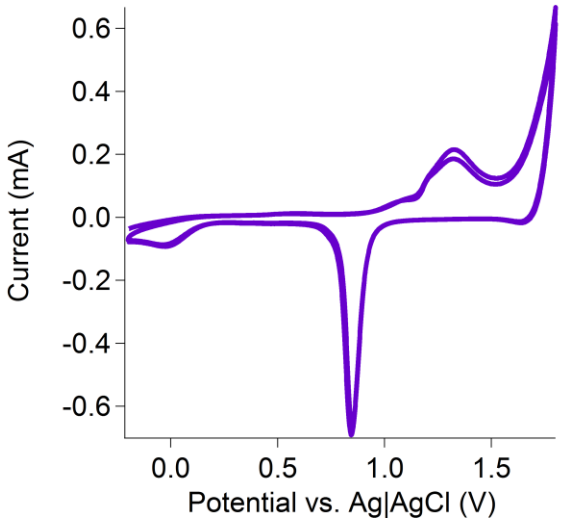

Figure A19. Representative cyclic voltammogram used to determine electrochemically active gold surface area. Scan taken in 0.5 M H_2SO_4 at 100 mV/s.

APPENDIX B

SUPPORTING INFORMATION FOR CHAPTER IV: ATOMICALLY PRECISE GOLD CLUSTERS TETHERED TO BORON DOPED DIAMOND THROUGH MOLECULAR LINKERS: INFLUENCE OF CORE SIZE AND CATALYST COVERAGE ON OXYGEN ELECTROREDUCTION ACTIVITY

Experimental details

Materials and characterization. Water (18.2 MΩ·cm) was obtained from a Barnstead Nanopure Diamond system. Hydrogen tetrachloroaurate was purchased from Strem Chemicals. Potassium hydroxide (99.99%, semi-conductor grade) was obtained from Aldrich. Chloroform was filtered over alumina before use to remove acidic impurities. All other reagents were used without further purification. Free-standing, electrochemical grade boron doped diamond (Element Six, 0.6 mm thick) was laser cut into round disks (0.78 cm^2) to be compatible with the rotating ring disk electrode setup.

Nuclear magnetic resonance spectroscopy (^1H and ^{31}P) was performed on either a Varian Inova 300 MHz or 500 MHz spectrometer or a Bruker Avance III-HD 500 MHz spectrometer to assess the purity of the compounds. Diffusion ordered spectroscopy (^1H DOSY) were collected on a Varian Inova 500 MHz spectrometer using the Doneshot sequence. UV-Vis spectra were measured on an Ocean Optics USB2000 spectrometer in a quartz cuvette (1 cm path length). X-ray photoelectron spectroscopy (XPS) was done on a ThermoScientific ESCALAB 250 X-ray Photoelectron Spectrometer using an Al Kα monochromated source (150 W, 20 eV pass energy, 500 μm spot size). Peak fitting was performed using ThermoScientific Avantage 4.75 software. A Smart background was

used during spectra analysis, and all peaks were referenced to the C1s hydrocarbon peak (284.8 eV).

Rotating ring disk electrode measurements were made on a Bio-Logic SP-300 potentiostat. The NP-functionalized BDD electrode was incorporated into a ChangeDisk rotating ring disk electrode tip (Pine Research, Pt ring, PTFE shroud) for all measurements (except the solution deposited AuNPs), using a glassy carbon support disk to make electrical contact between the ChangeDisk tip and BDD disk electrode. The ChangeDisk rotating ring disk electrode tip was attached to a Pine Research MSR rotator. Cyclic voltammetry of solution deposited TPP-Au_{101} was measured using a BAS 100B Electrochemical Analyzer (Bioanalytical Systems).

Synthesis and characterization of gold cluster/nanoparticle materials and molecular tethers. *Synthesis of 6-heptene-1-thioacetate (HTA).* Potassium thioacetate (0.012 mol, 1.37 g) was dissolved in 100 mL of acetone and sparged with nitrogen while stirring. 7-bromo-1-heptene (0.012 mol, 1.82 mL) was added to this solution and it was allowed to stir overnight under nitrogen. The white solid was removed via filtration and the compound was purified with silica gel chromatography (eluent: 1:9 dichloromethane/hexanes). The colorless oil was present in the second spot in 66% yield. ^{1}H NMR (300 MHz, CD_2Cl_2), δ 5.83 (m, 1H), 5.00 (m, 2H), 2.85 (t, 2H), 2.33 (s, 3H), 2.06 (m, 2H), 1.59 (m, 2H), 1.40 (m, 4H).

*Synthesis of $Au_8(PPh_3)_8(NO_3)_2$ (**TPP-Au_8**).* **TPP-Au_8** was synthesized using a previously reported method.[1] The compound was washed with toluene (2 x 30 mL) and hexanes (2 x 20 mL) in centrifuge tubes to remove excess ligand. The compound was then crystallized from a dichloromethane solution by diffusion of diethyl ether in a

freezer over five days to produce dark red crystals. The crystallized product was used for all studies. ^{1}H NMR (500 MHz, CD_2Cl_2) δ 7.07 (d, 71H), 6.67 (t, 49H) referenced to residual non-deuterated dichloromethane (δ 5.32). ^{31}P NMR (202 MHz, CD_2Cl_2), δ 55.02 referenced to H_3PO_4.

*Synthesis of $Au_9(PPh_3)_8(NO_3)_3$ (**TPP-Au_9**)* **TPP-Au$_9$** was synthesized following a literature preparation.[1] The compound was crystallized from a methanol solution by diffusion of diethyl ether in a freezer over five days to produce dark green crystals. The crystallized product was used for all studies. ^{1}H NMR (500 MHz, CD_2Cl_2) δ 7.16 (m, 72H, 6.73 (t, 48H) referenced to residual non-deuterated dichloromethane (δ 5.32). ^{31}P NMR (202 MHz, CD_2Cl_2), δ 56.9 referenced to H_3PO_4.

*Synthesis of $Au_{11}(PPh_3)_8Cl_3$ (**TPP-Au_{11}**).* **TPP-Au$_{11}$** was synthesized from a previously published procedure.[2] The compound was crystallized from a dichloromethane solution by slow diffusion of hexanes in a freezer over five days to produce red crystals. The crystallized product was used for all studies. The compound was characterized with NMR and UV-Vis spectroscopy. ^{1}H NMR (300 MHz, CD_2Cl_2), δ 7.30 (br t), 6.93 (t), 6.68 (t).

*Synthesis of $Au_{101}(PPh_3)_{21}Cl_5$ (**TPP-Au_{101}**).* **TPP-Au$_{101}$** was synthesized using a previously published literature preparation.[3] The product was purified by a series of precipitation/centrifugation steps with hexanes, pentane, 3:1 pentane/dichloromethane (3x), 2:1 pentane/dichloromethane (3x), and 1:1 pentane/chloroform (2x). The compound was characterized with NMR and UV-Vis spectroscopy. A broad peak between 7-8 ppm was observed in the ^{1}H NMR spectrum indicating that the triphenylphosphine ligands were bound to the nanoparticle surface.

Assembly of triphenylphosphine AuNPs onto heptane-thioacetate functionalized boron doped diamond. (TPP-Au$_x$-HTA-BDD). Heptane-thioacetate functionalized boron doped diamond (HTA-BDD) was fabricated using a previously reported procedure.[4] Briefly, boron doped diamond was hydrogen terminated by heating in a quartz tube furnace under hydrogen at 850°C for 20 minutes before cooling the sample back down to room temperature under hydrogen. 6-heptene-1-thioacetate (~1 μL) was placed on the surface of a hydrogen terminated boron doped diamond substrate and covered by a quartz slide to make a thin film of the thioacetate on the BDD surface. The sample was irradiated with 254 nm light under argon for 5 hours in a Novascan PSD Pro Series Digital UV Ozone System. The sample was cleaned by sonication in toluene (2x, 5 min) and chloroform (2x, 5 min) to remove physiadsorbed material. The samples were used relatively soon after functionalization to prevent oxidation of the thioacetate.

*Assembly of **TPP-Au$_8$** and **TPP-Au$_9$** onto HTA-BDD.* **HTA-BDD** was placed into a solution of **TPP-Au$_8$** or **TPP-Au$_9$** (argon sparged, ~0.2 mg/mL) in a capped scintillation vial and allowed to sit overnight in a closed drawer. The samples were rinsed with dichloromethane (3x) before further characterization was performed.

Assembly of TPP-Au$_{11}$ onto HTA-BDD. HTA-BDD was placed in a solution of **TPP-Au$_{11}$** in DCM (~0.2 mg/mL, argon sparged) in a capped scintillation vial and allowed to sit overnight in a closed drawer. To examine samples with higher coverage, HTA-BDD was placed into a solution of **TPP-Au$_{11}$** in chloroform (~1 mg/mL) and heated at 50°C overnight under nitrogen, conditions previously reported for ligand exchange reactions of this material.[2,5] The sample was rinsed with dichloromethane (3x) before further characterization.

Assembly of TPP-Au_{101} onto HTA-BDD. HTA-BDD was placed into a solution of TPP-Au_{101} in THF (~1 mg/mL) in a capped scintillation vial and allowed to sit overnight. The sample was rinsed with dichloromethane (3x) before further characterization.

Assessing the electrocatalytic activity of TPP-Au_x towards oxygen electroreduction. The TPP-Au_x-HTA-BDD samples were placed into the RRDE tip and rotated at 500 rpm for all measurements. The electrochemical cell was a 125 mL Nalgene container. The electrolyte was sparged with oxygen or argon for at least 10 minutes before measurements were taken. For measurements in alkaline conditions (0.1 M KOH), a Hg|HgO (1 M KOH) reference electrode was used, and the Pt ring electrode was held at 0.2 V vs. Hg|HgO. Glass components were avoided to prevent contamination by base etching. For measurements in acidic conditions (0.5 M H_2SO_4), a Ag|AgCl (3 M NaCl) was used, and the Pt ring electrode was held at 0.8 V vs. Ag|AgCl. The counter electrode was a coiled platinum wire for all measurements. All samples were measured at 500 rpm at a scan rate of 20 mV/s while oxygen was bubbling through the electrolyte. Several control measurements were also performed with argon bubbling. Potentials are plotted versus the reference hydrogen electrode (RHE) to simplify comparisons to existing literature. The TPP-Au_{101} samples deposited on a glassy carbon electrode (3 mm in diameter) were measured in O_2 sparged 0.1 M NaOH at a scan rate of 100 mV/s in a 20 mL glass cell with a Ag|AgCl reference electrode and a Pt wire counter electrode. The NPs were deposited onto the GC surface through drop-casting or adsorption of a crude monolayer formed through assembly of NPs at the air/water interface.

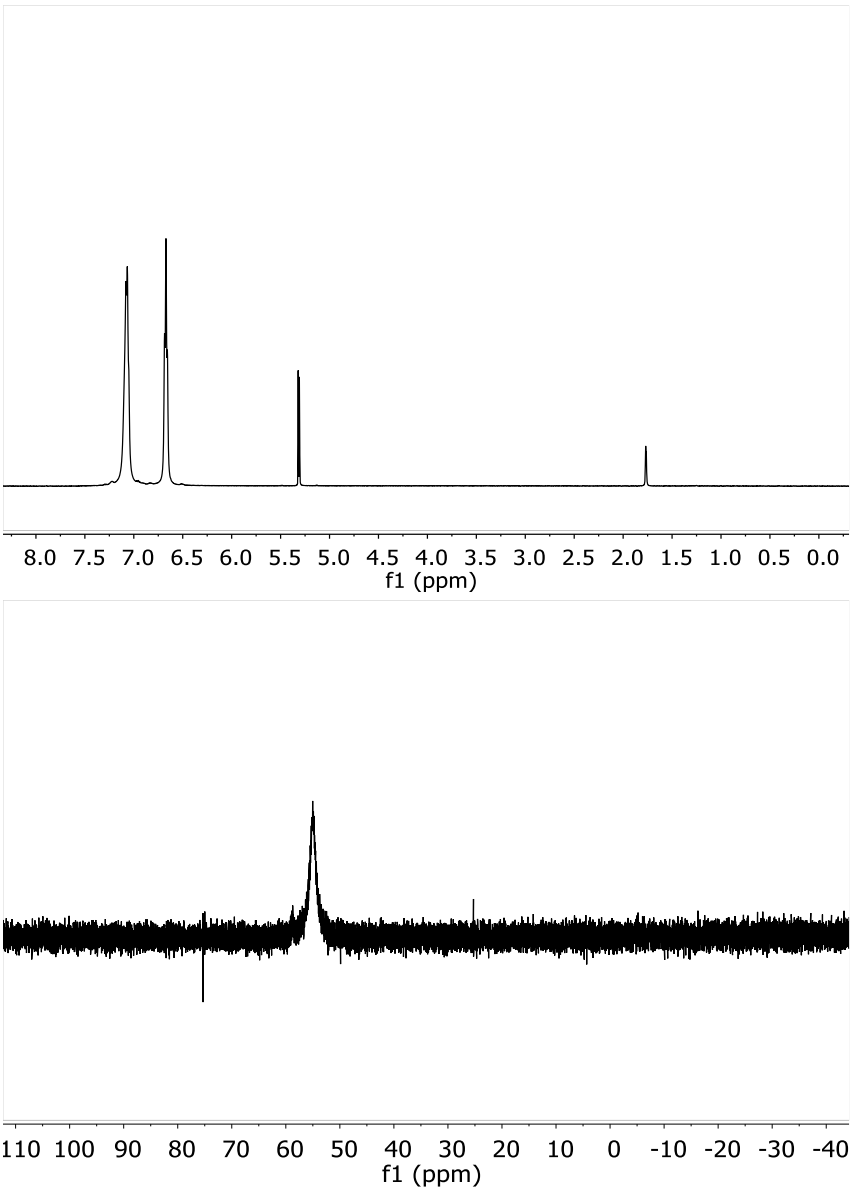

Figure B1. ^{1}H NMR (top) and ^{31}P NMR (bottom) spectra of $Au_8(PPh_3)_8(NO_3)_2$ dispersed in CD_2Cl_2.

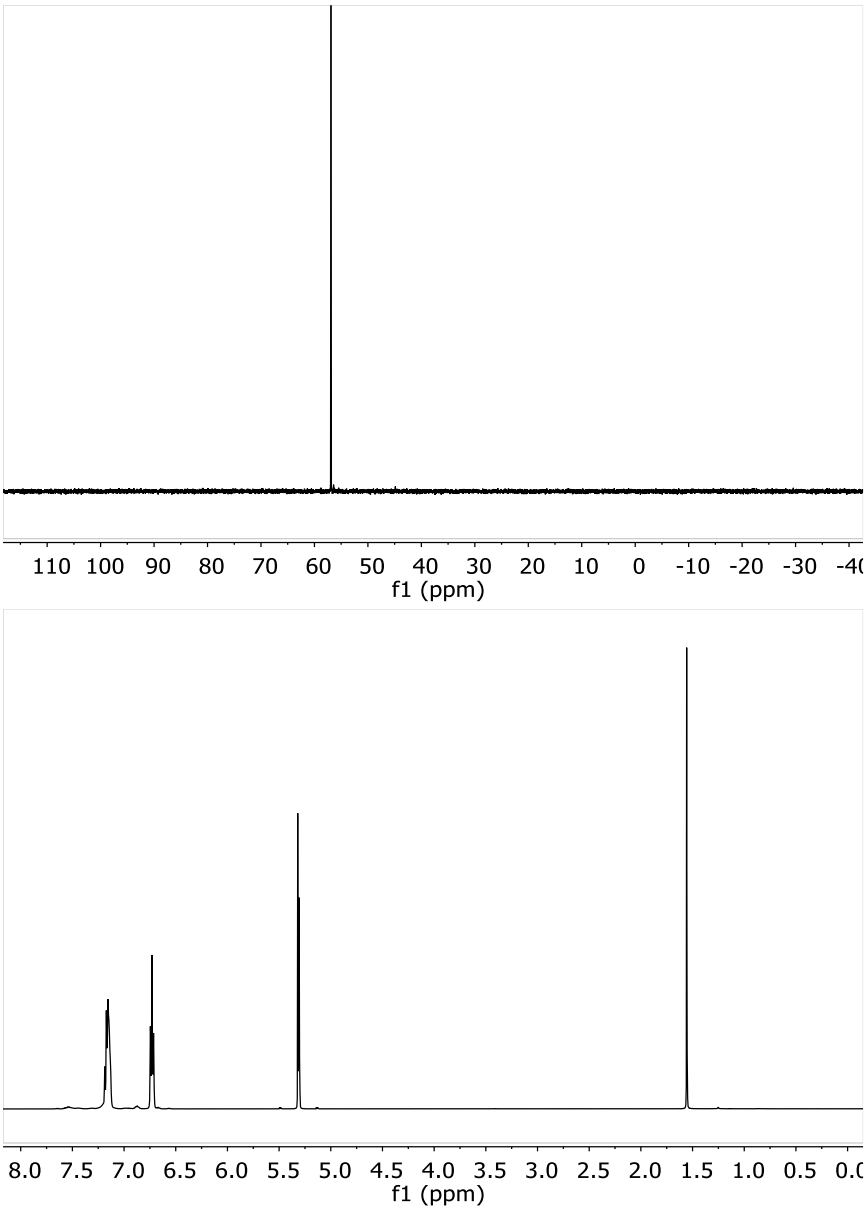

Figure B2. ^{1}H NMR spectrum (top) and ^{31}P NMR (bottom) of $Au_9(PPh_3)_8(NO_3)_3$ dispersed in CD_2Cl_2.

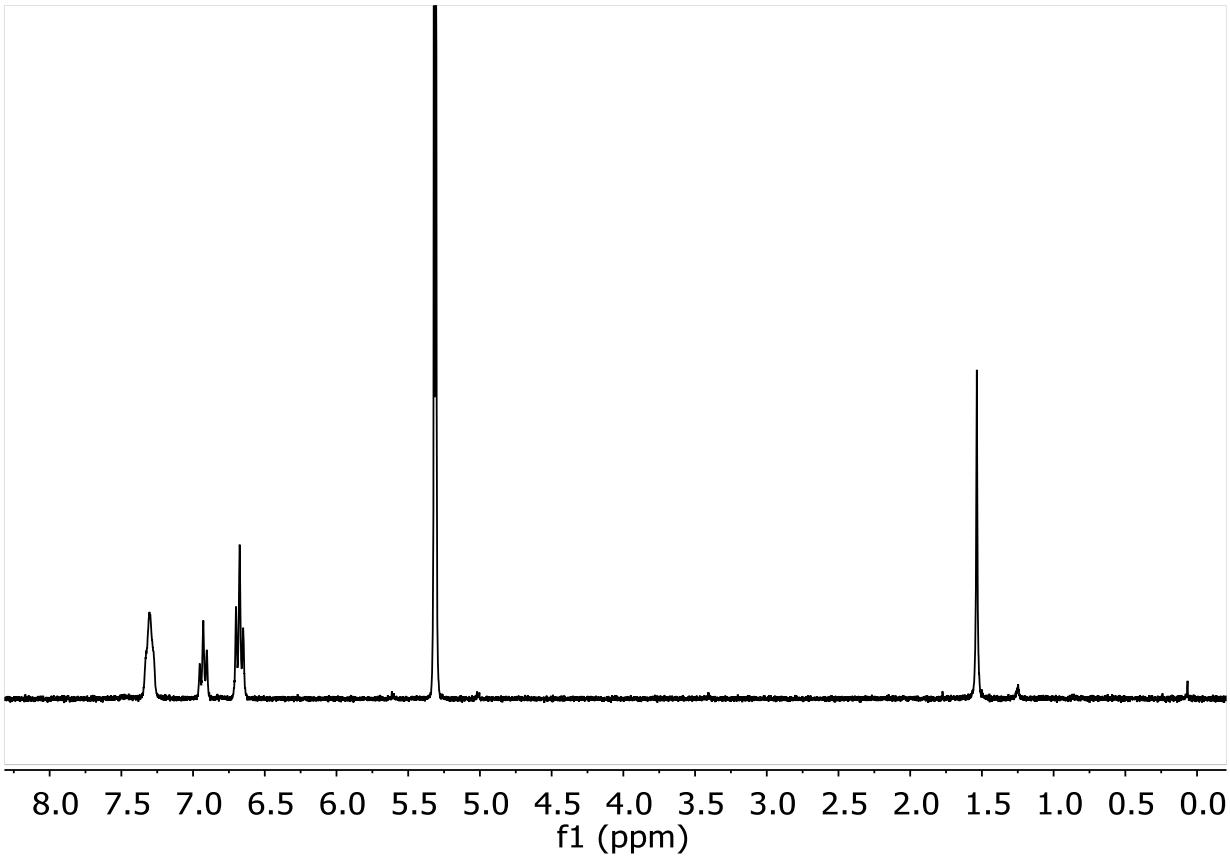

Figure B3. ^{1}H NMR spectrum of $Au_{11}(PPh_3)_8Cl_3$ dispersed in CD_2Cl_2.

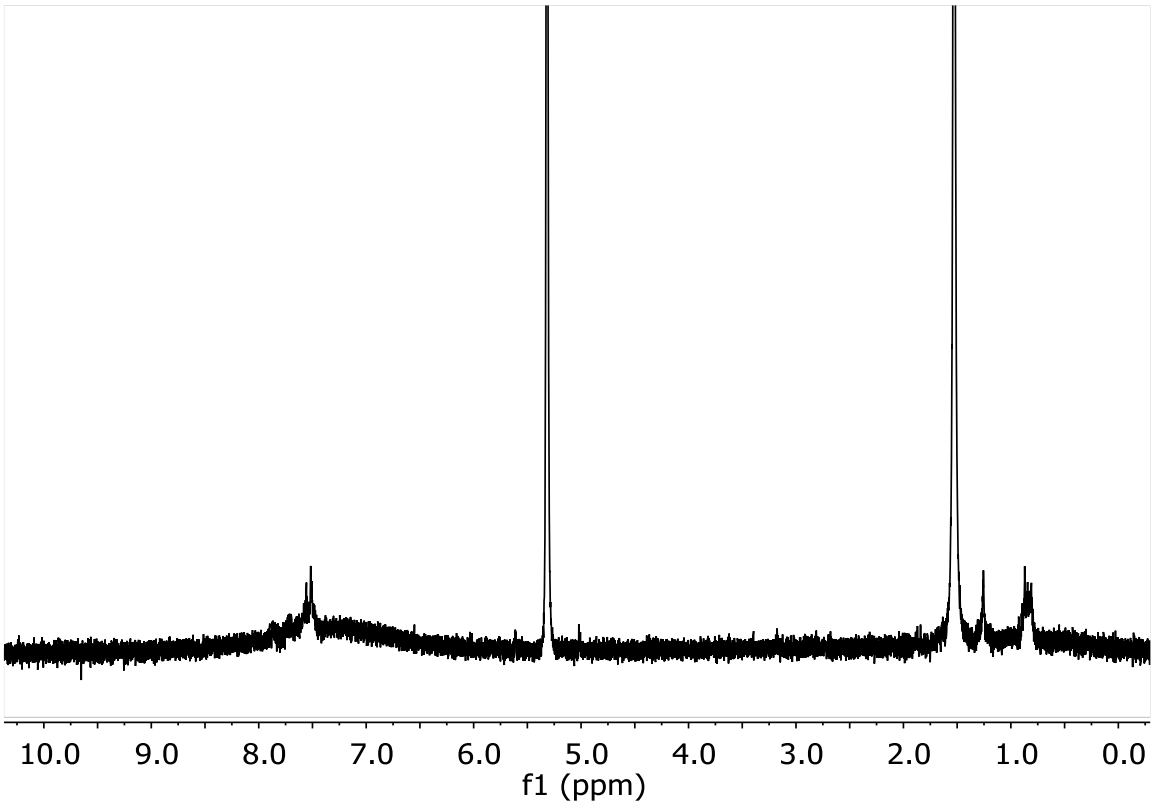

Figure B4. ^{1}H NMR spectra of $Au_{101}(PPh_3)_{21}Cl_5$ dispersed in CD_2Cl_2..

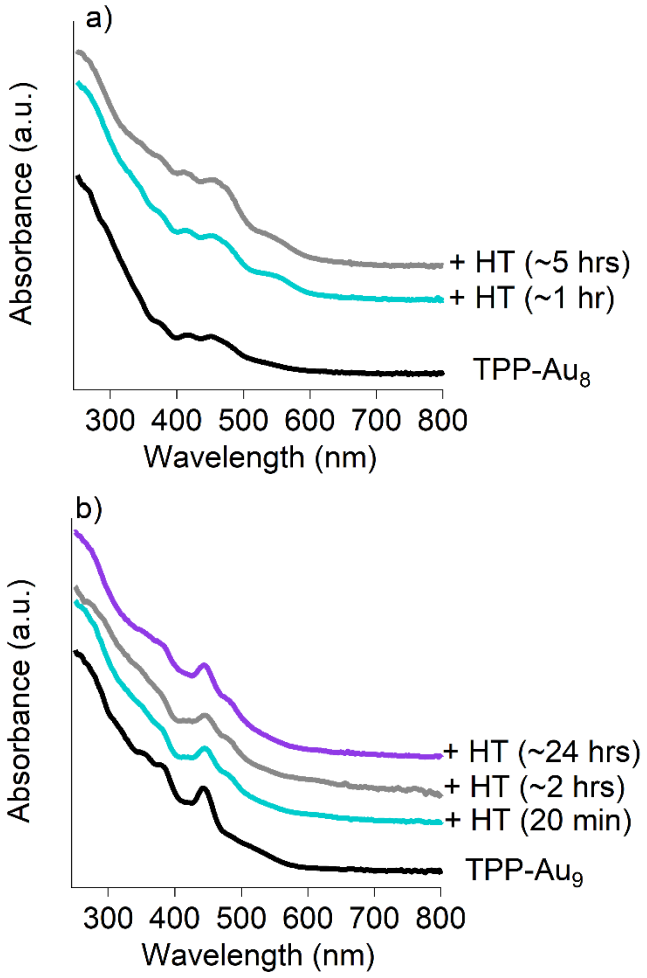

Figure B5. UV-Vis spectra of a) $Au_8(PPh_3)_8(NO_3)_2$ and b) $Au_9(PPh_3)_8(NO_3)_3$ in CD_2Cl_2 before and after reacting with 1 eq hexanethiol at room temperature. The spectra are offset on the y axis for clarity. The spectra remain largely unchanged after reacting with the hexanethiol indicating that the cluster core remains stable in conditions similar to those when assembling onto the thiol-functionalized BDD surface.

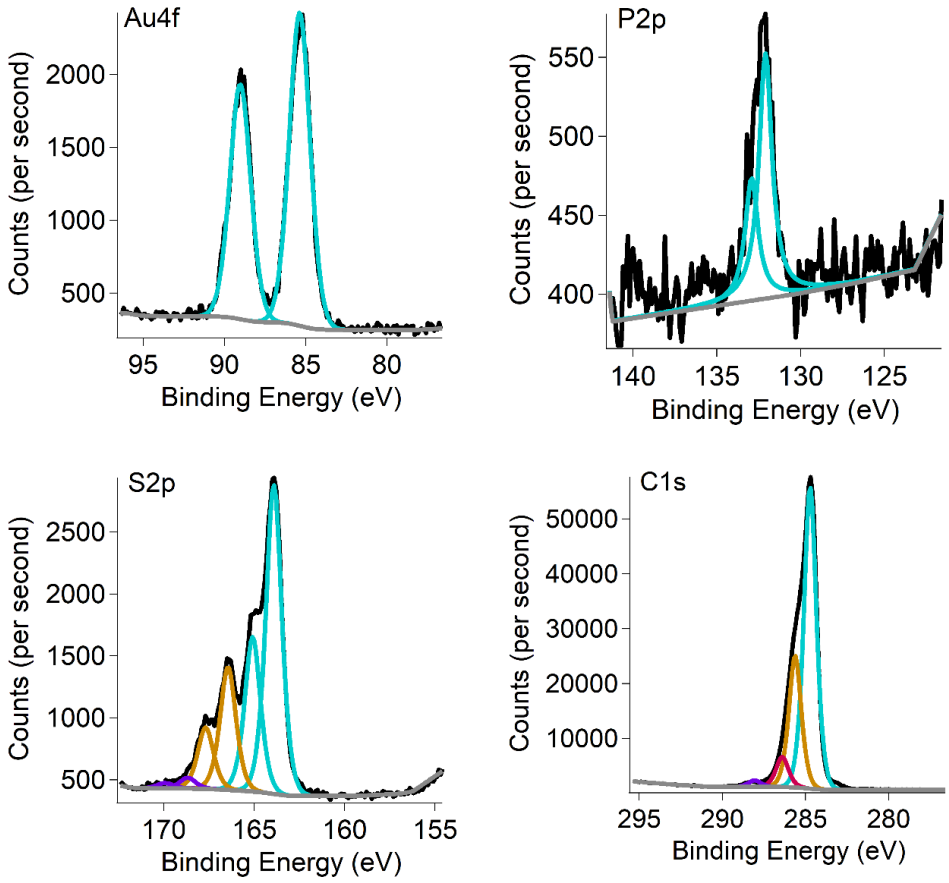

	XPS Au:$C_{284.8}$ ratio
HTA-BDD	0.0072 ± 0.0005
Bare BDD (control)	0.0024 ± 0.0005

Figure B6. XPS elemental spectra (Au 4f, P 2p, S 2p, and C 1s) of TPP-Au_8-HTA. The black trace shows the raw data and the colored traces are the peak fitting. Table shows XPS Au:$C_{284.8}$ ratios for TPP-Au_8 assembly on HTA-BDD compared to physiadsorption on bare BDD indicating successful assembly.

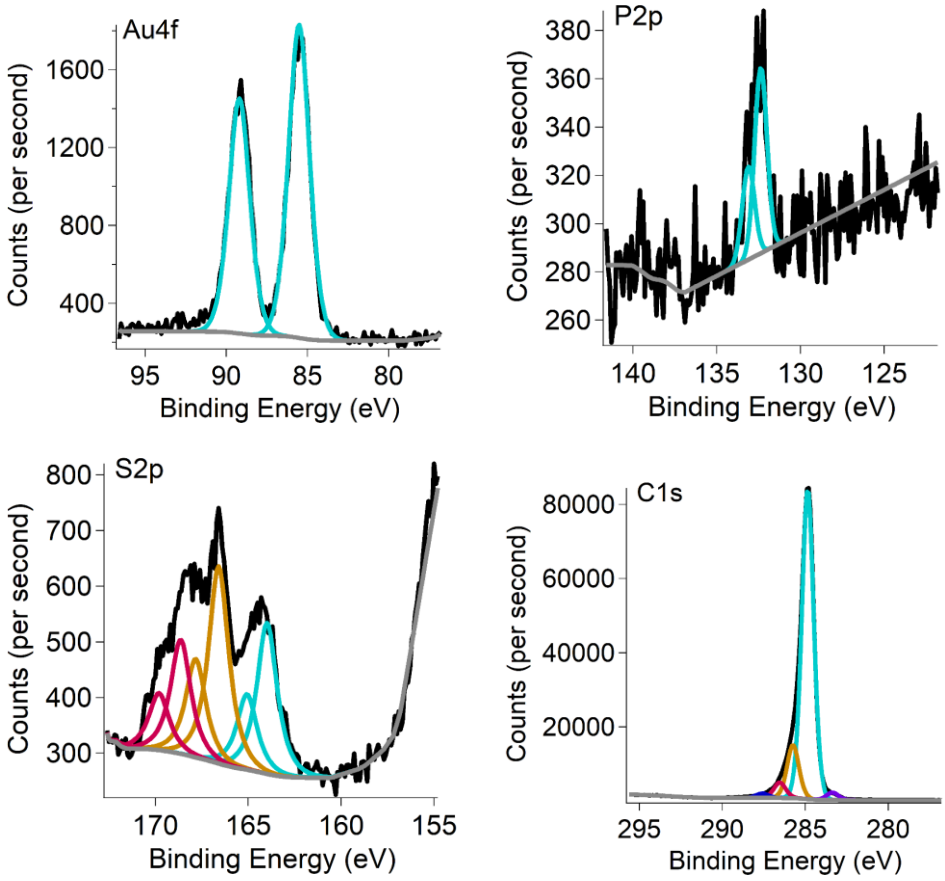

Electrode	**XPS Au:$C_{284.8}$ ratio**
HTA-BDD	0.005 ± 0.002
Bare BDD (control)	0.0004 ± 0.0001

Figure B7. XPS elemental spectra (Au 4f, P 2p, S 2p, and C 1s) of TPP-Au_9-HTA. The black trace shows the raw data and the colored traces are the peak fitting. Table shows XPS Au:$C_{284.8}$ ratios for TPP-Au_9 assembly on HTA-BDD compared to physiadsorption on bare BDD indicating successful assembly.

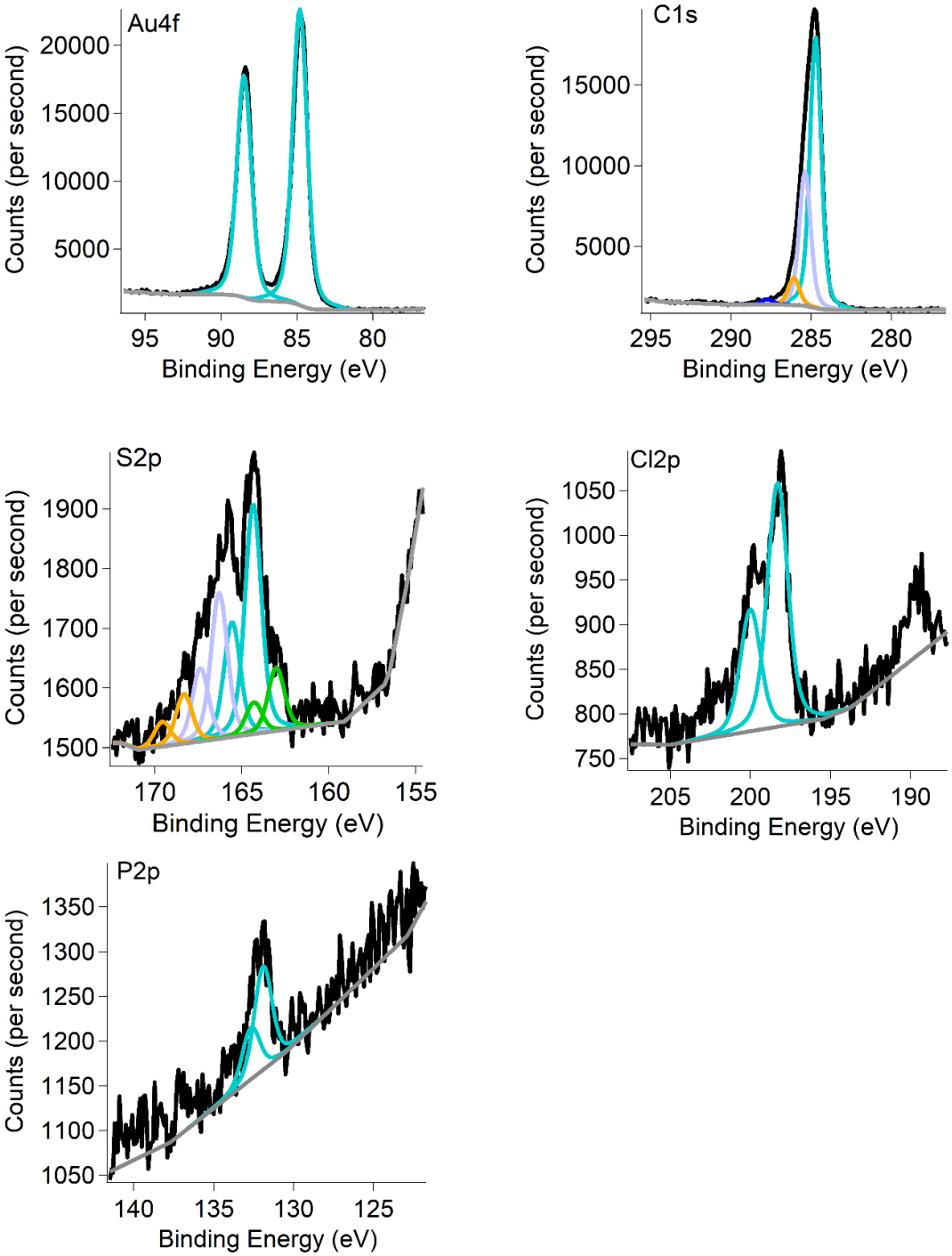

Figure B8. XPS elemental spectra (Au 4f, P 2p, C1 2p, S 2p, and C 1s) of TPP-Au_{11}-HTA. The black trace shows the raw data and the colored traces are the peak fitting.

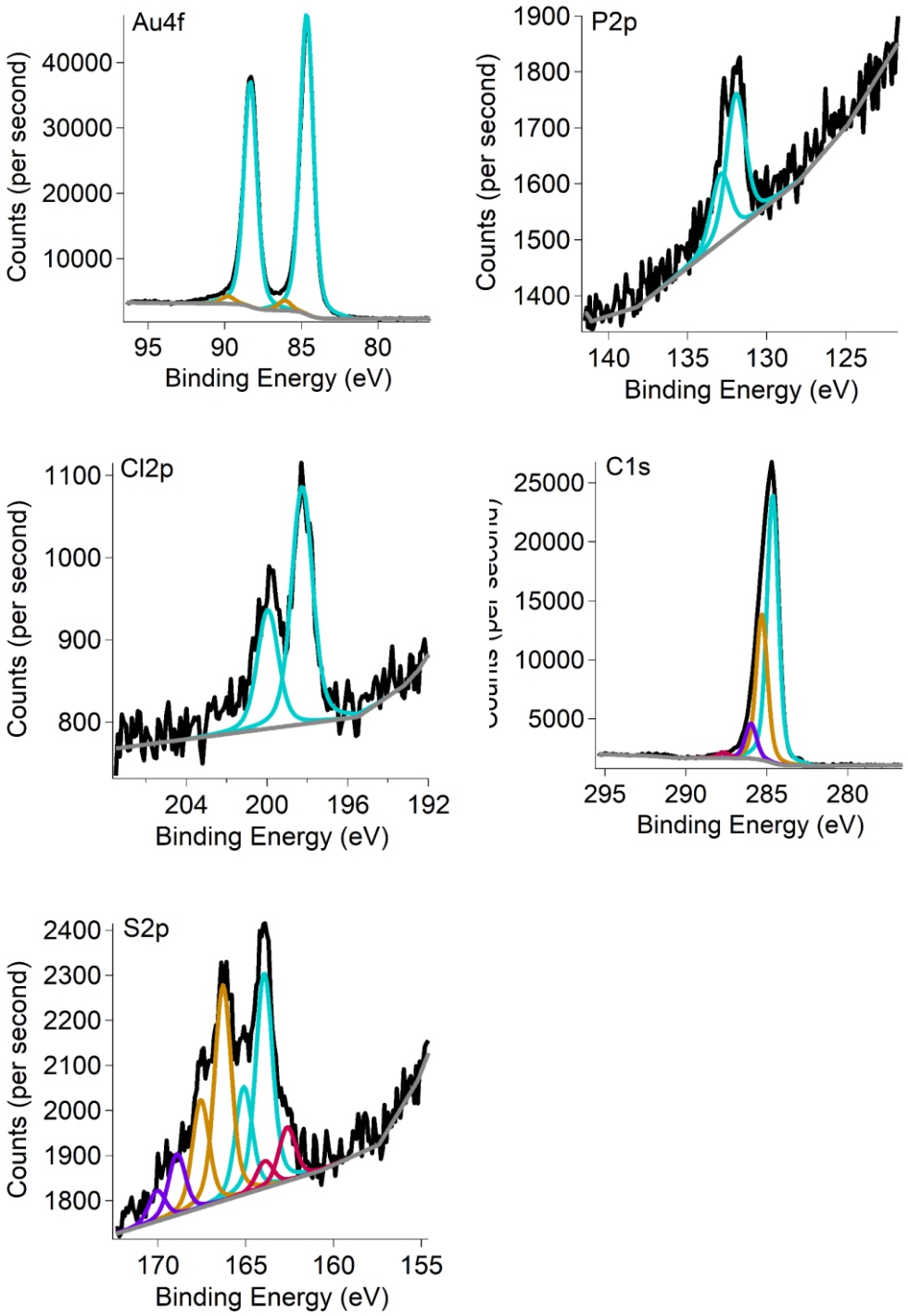

Figure B9. XPS elemental spectra (Au 4f, P 2p, C1 2p, S 2p, and C 1s) of TPP-Au_{101}-HTA. The black trace shows the raw data and the colored traces are the peak fitting.

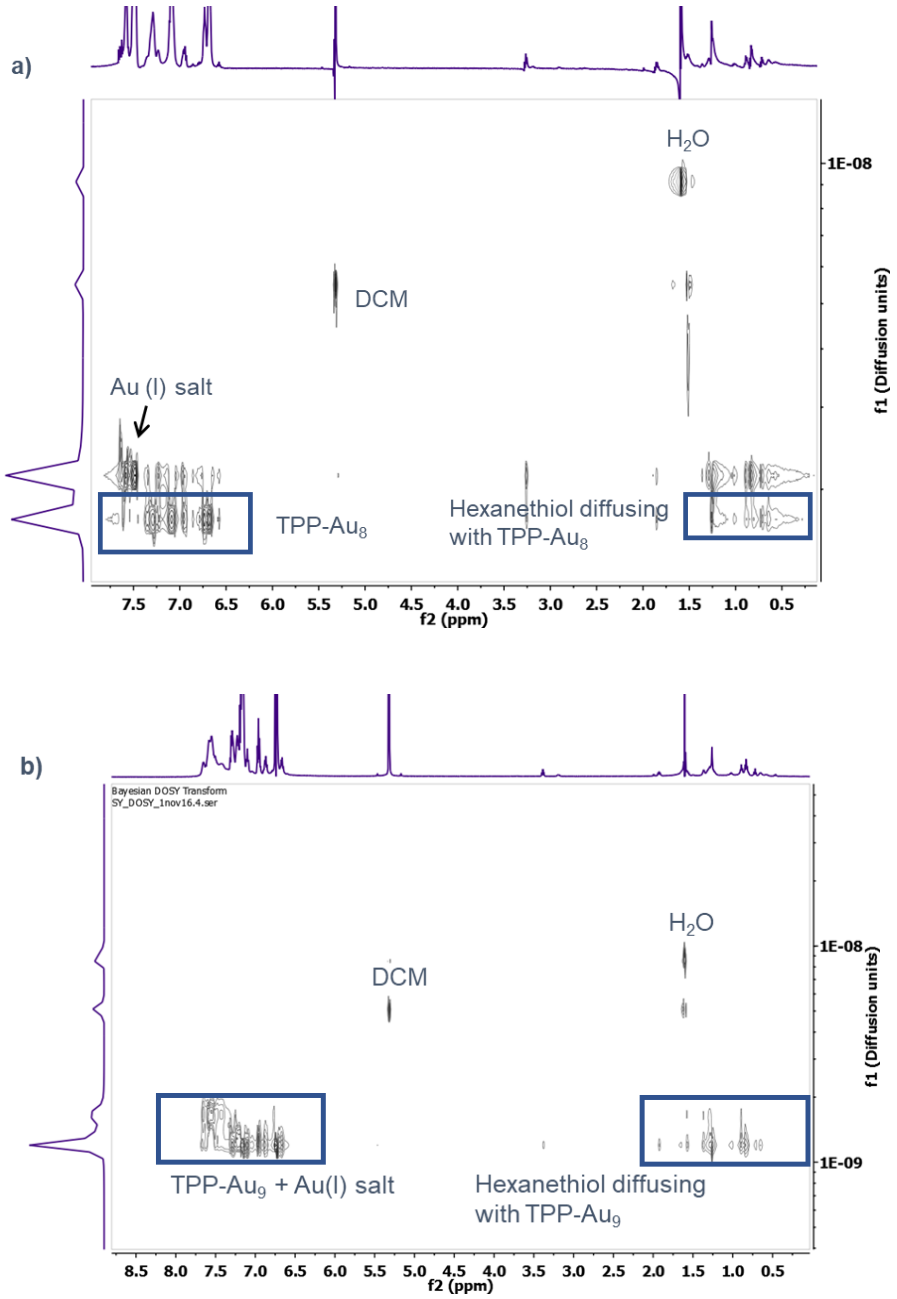

Figure B10. ^{1}H DOSY spectrum of a) $Au_8(PPh_3)_8(NO_3)_2$ and b) $Au_9(PPh_3)_8(NO_3)_3$ mixed with 1 eq hexanethiol in CD_2Cl_2. The presence of hexanethiol peaks diffusing at the same diffusion coefficient as the Au cluster indicates that ligand exchange occurs. The presence of the peaks associated with the original clusters are still present indicating that the cluster remains largely intact during ligand exchange with a small equivalent of a thiol.

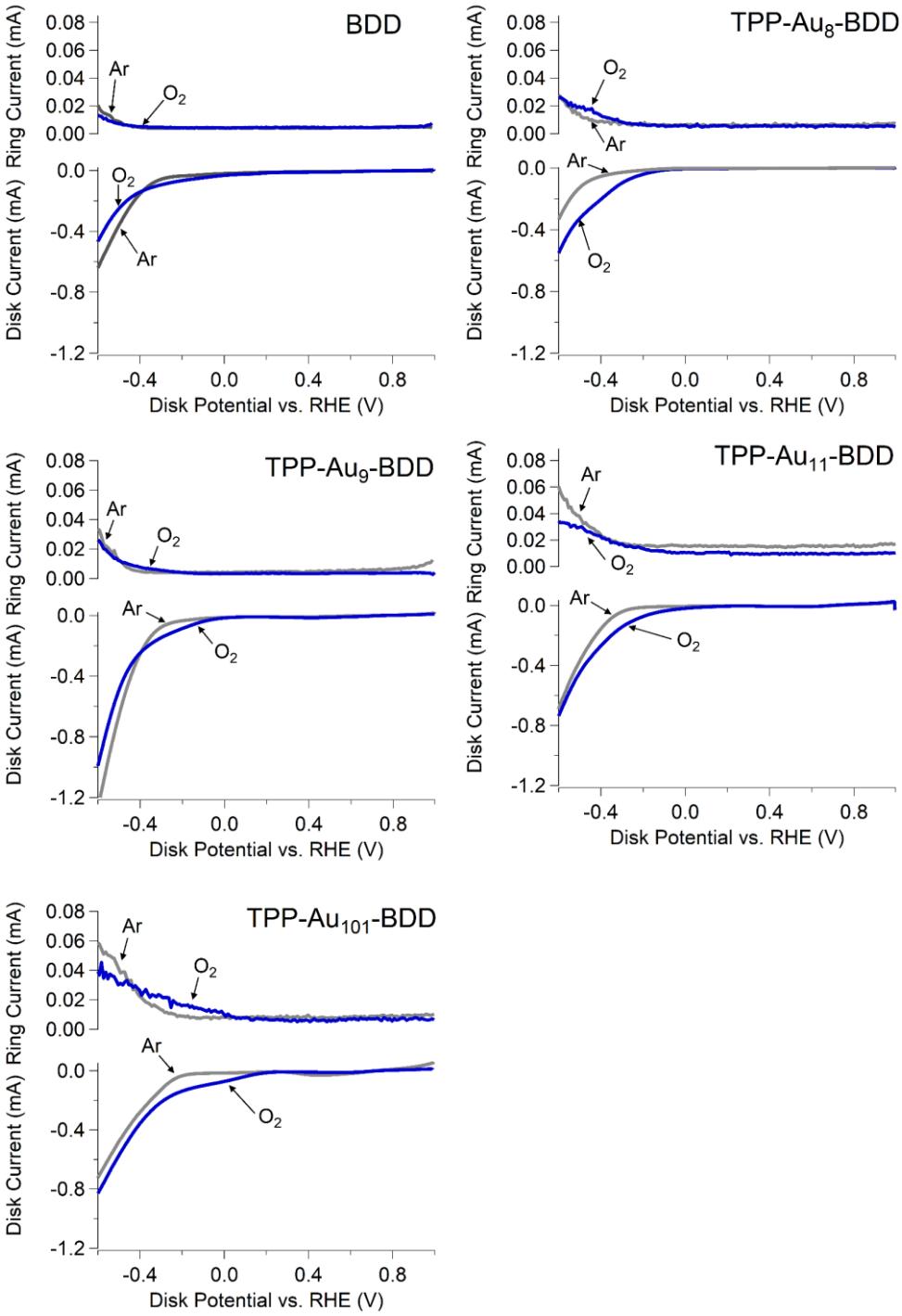

Figure B11. Rotating ring disk voltammograms of BDD and TPP-Au_x-BDD in O_2 sparged (blue traces) or argon sparged (gray traces) 0.5 M H_2SO_4. Samples were measured at 20 mV/s while the electrode was rotated at 500 rpm.

Table B1: XPS P:Au ratios before and after electrochemistry		
Sample	*Before*	*After*
TPP-Au_{11}-HTA	0.15 ± 0.02	0.0997 ± 0.0006
TPP-Au_{101}-HTA	0.140 ± 0.006	no signal detected

APPENDIX C

SUPPORTING INFORMATION FOR CHAPTER V: SMALL SILVER-GOLD NANOPARTICLE ELECTROCATALYSTS MOLECULARLY INTERFACED TO BORON DOPED DIAMOND: ASSESSING THE INFLUENCE OF CORE SIZE, STRUCTURE, AND COMPOSITION ON OXYGEN ELECTROREDUCTION IN ALKALINE CONDITIONS

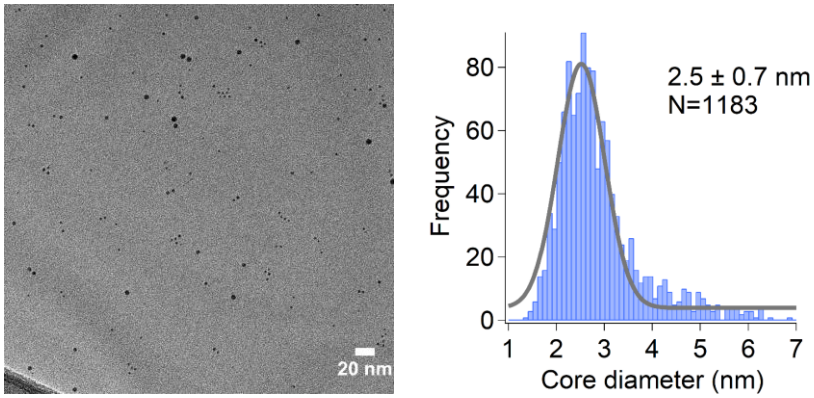

Figure C1. Representative TEM image of UDT-AgNPs (left). The size distribution of the UDT-AgNPs was determined by fitting a Gaussian curve to a histogram plot (right) generated from measurement of 1183 nanoparticles.

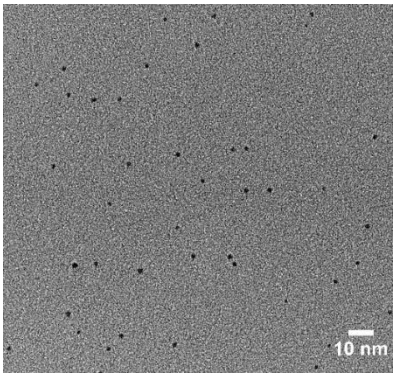

Figure C2. Representative TEM image of UDT-AuNPs drop-cast on a lacey carbon grid.

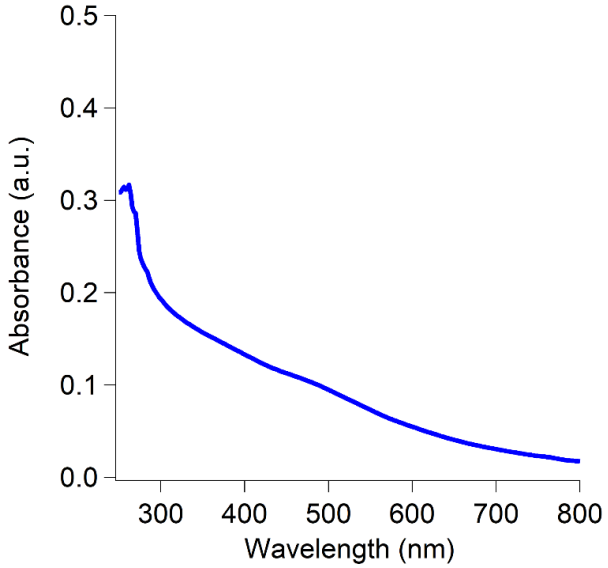

Figure C3. UV-Vis spectrum of UDT-AuNPs dispersed in heptane at concentration used for grafting experiments. The broad plasmon ~500 nm is further evidence that the AuNP cores are small (d_{core} < 2.5 nm).

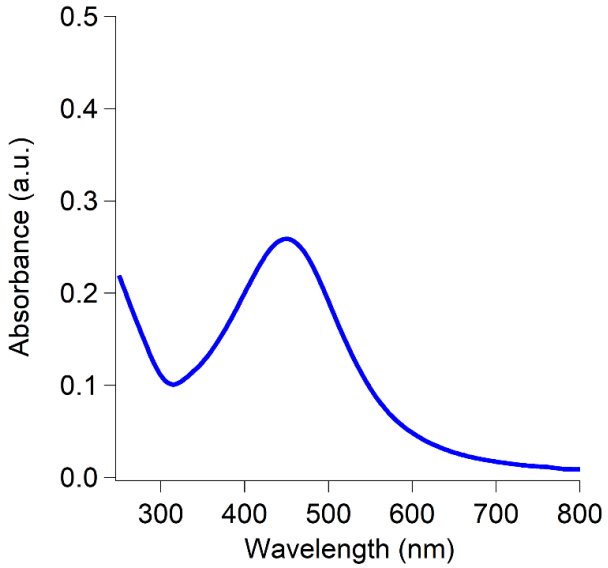

Figure C4. UDT-AgNPs dispersed in heptane at concentration used for grafting experiments. The presence of a plasmon at ~460 nm is characteristic of AgNPs in this size regime (d_{core} < 3 nm).

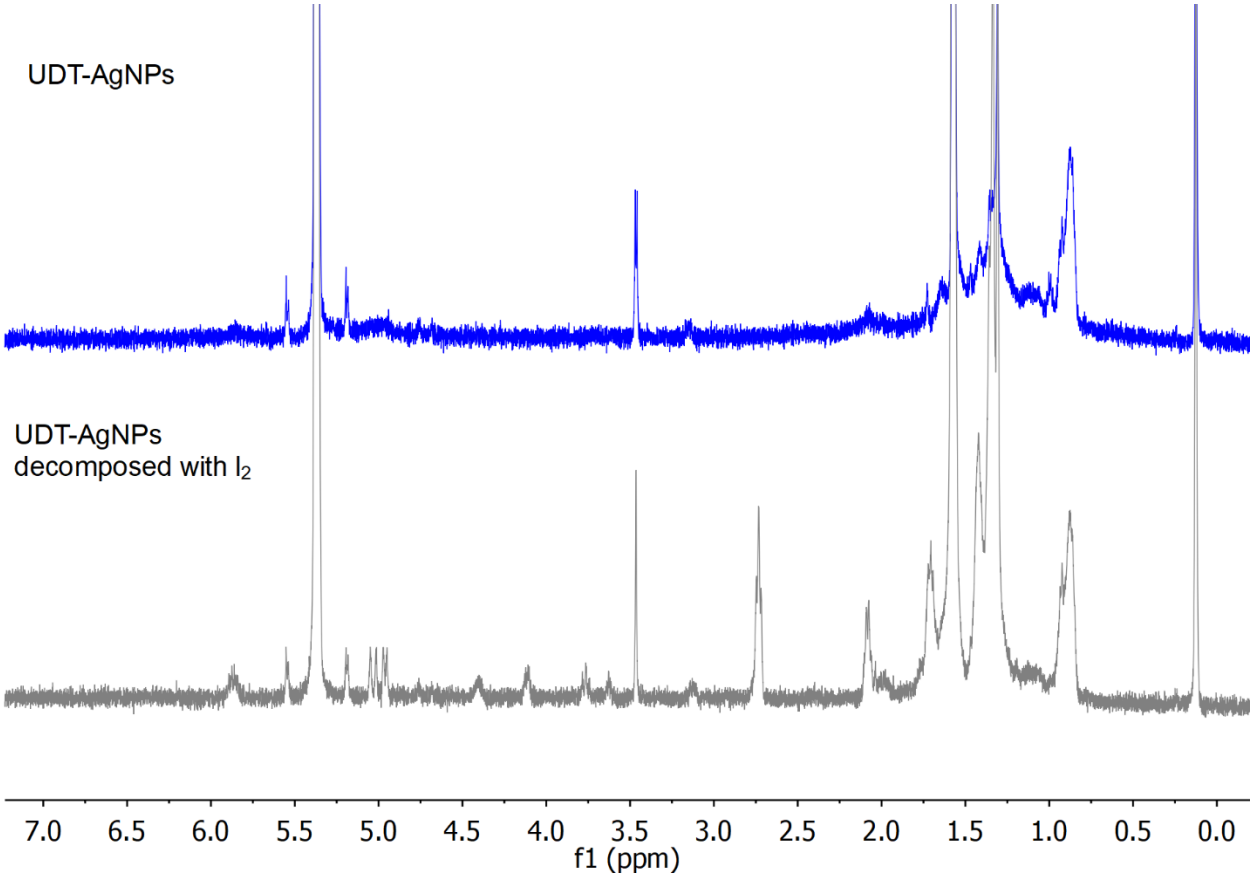

Figure C5. ^{1}H NMR spectrum of UDT-AgNPs in CD_2Cl_2 (top) and after decomposition with iodine (bottom). The absence of any sharp peaks indicates that all free undecenethiol was removed during purification. The presence of sharp peaks characteristic of undecenyl disulfide in the spectrum after iodine decomposition is further evidence that the AgNP is stabilized by a undecenethiolate ligand shell. The sharp peak at 3.4 ppm is residual methanol from purification.

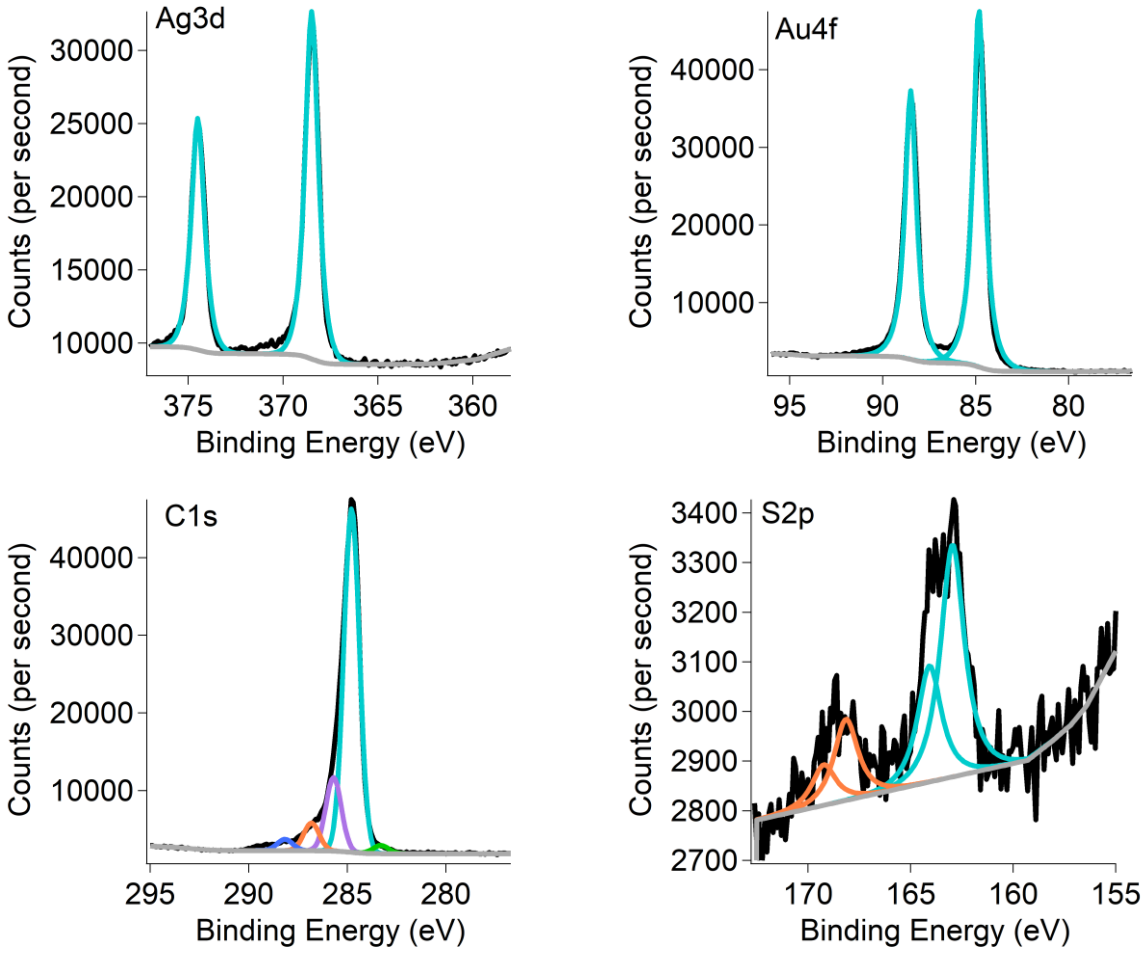

Figure C6. XPS regional spectra of Ag-AuNP-BDD showing the presence of silver on the AuNPs after galvanic exchange. The black traces are the raw data and the colored traces are the peak fittings. The presence of thiolate sulfur (~163 eV) indicates a portion of the undecenethiolate ligand shell is still present after the galvanic exchange process.

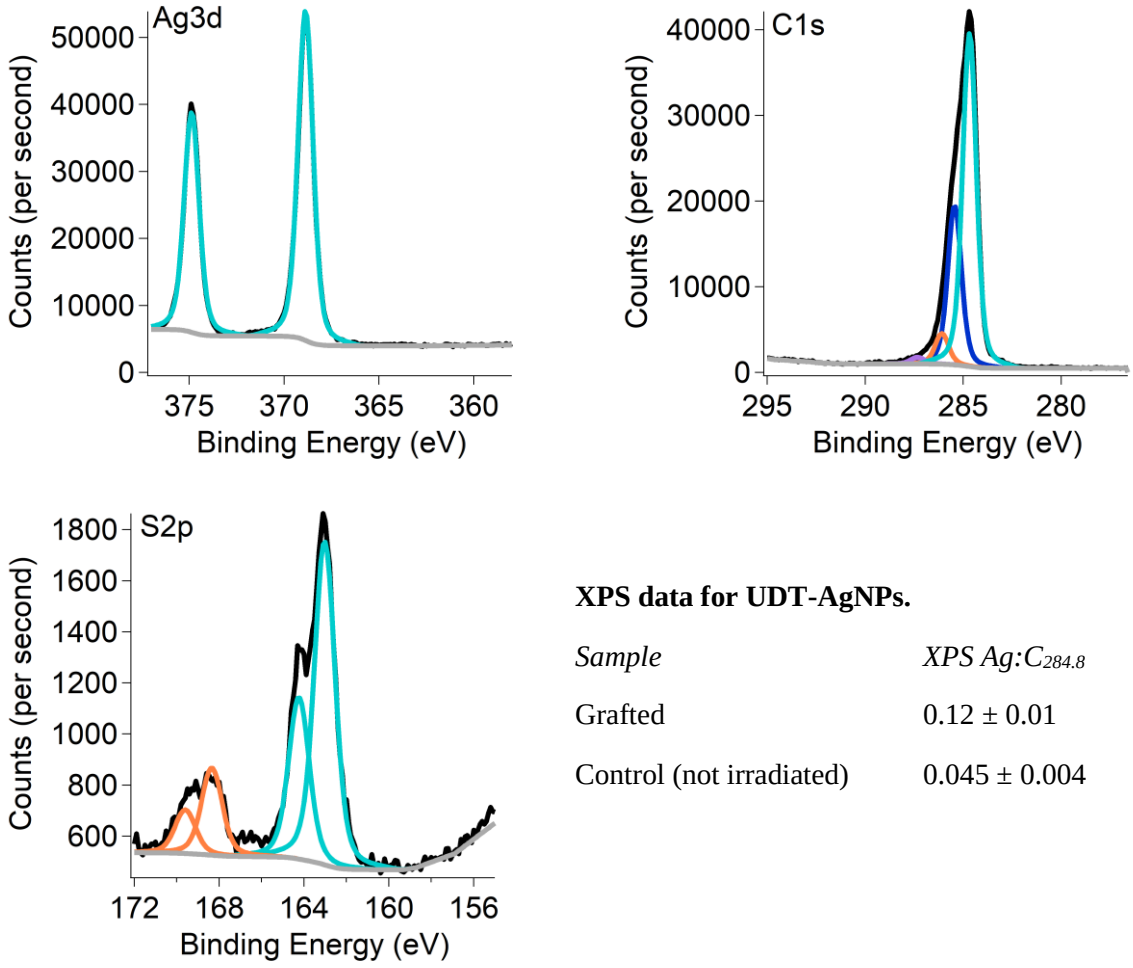

XPS data for UDT-AgNPs.

Sample	*XPS Ag:$C_{284.8}$*
Grafted	0.12 ± 0.01
Control (not irradiated)	0.045 ± 0.004

Figure C7. XPS regional spectra of UDT-AgNP-BDD. The black traces are the raw data and the colored traces are the peak fittings. The higher Ag:$C_{284.8}$ ratio of the irradiated sample compared to the control (not irradiated) UDT-AgNPs indicates that the AgNPs are grafted to the BDD surface and are not simply physiadsorbed.

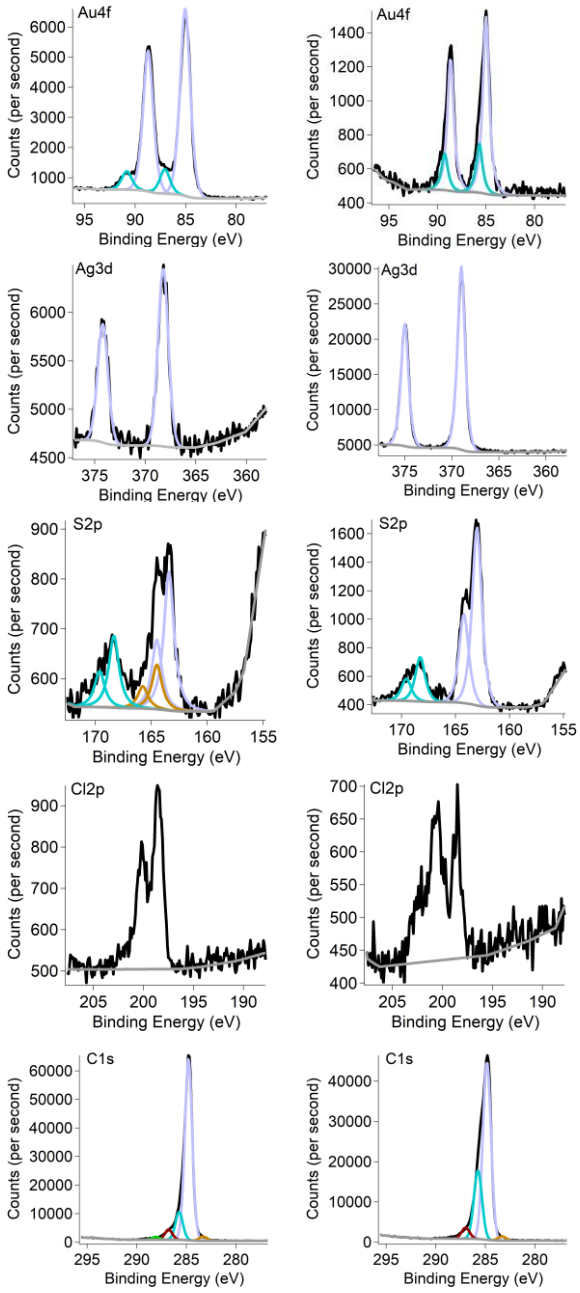

XPS binding energies for Au-AgNP-BDD samples

Sample	*Ag 3d$_{5/2}$ binding energy (eV)*	*Au 4f$_{7/2}$ binding energy (eV)*
Au-AgNP-BDD (more Au)	368.19 ± 0.03	85.04 ± 0.03
Au-AgNP-BDD (less Au)	368.93 ± 0.05	84.97 ± 0.03

Figure C8. XPS regional spectra of Au-AgNP-BDD. The left column is a sample with a higher Au:Ag ratio and the right column is a sample with a lower Au:Ag ratio. The black traces are the raw data and the colored traces are the peak fittings. The table shows the Au:Ag XPS binding energies for these samples.

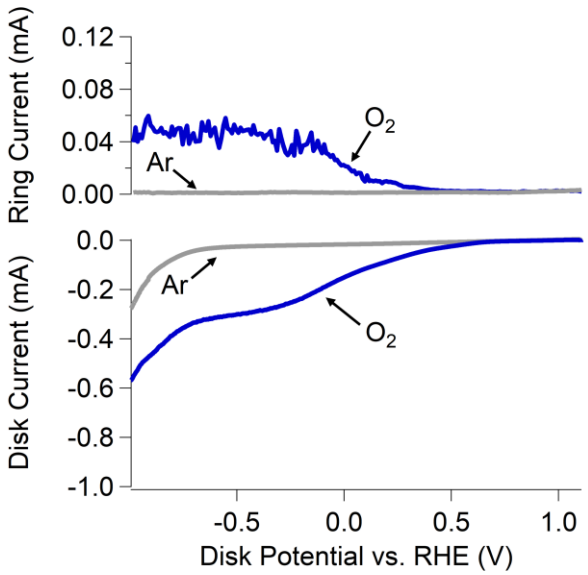

Figure C9. Rotating ring disk voltammetry of boron doped diamond in 0.1 M KOH with O_2 bubbling (blue traces) or argon bubbling (gray traces) in the same potential window used to evaluate the NP electrocatalysts showing its poor ORR electrocatalytic activity. All scans were performed at 20 mV/s while the electrode was rotated at 500 rpm.

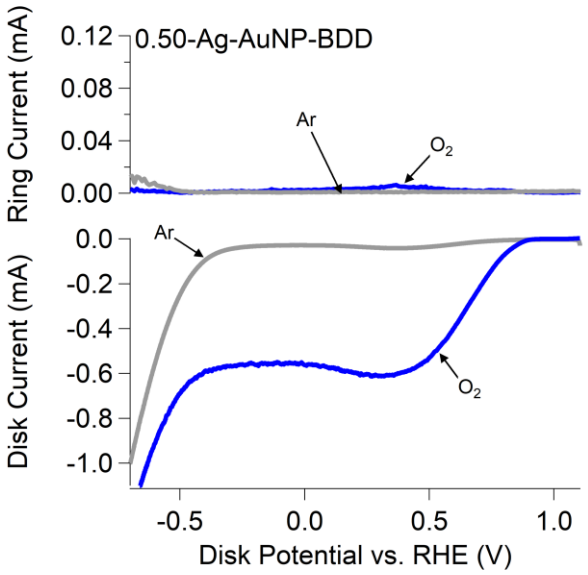

Figure C10. Representative rotating ring disk voltammetry of Ag-AuNP-BDD in 0.1 M KOH with O_2 bubbling (blue traces) or argon bubbling (gray traces). The lack of reduction current in the sample with the argon sparged electrolyte indicates that the current observed in the oxygen sparged electrolyte is a result of oxygen reduction. All scans were performed at 20 mV/s while the electrode was rotated at 500 rpm.

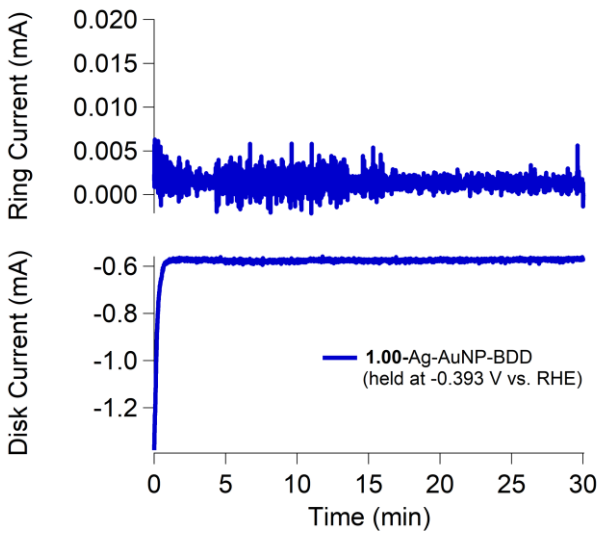

Figure C11. Chronoamperometry of a Ag-AuNP-BDD sample over 30 minutes used to assess catalyst stability at a relevant reducing potential for ORR where no ring current indicative of peroxide intermediate products is observed (-393 mV vs. RHE). The constant disk current and ring current over the course of 30 minutes indicates that no degradation of catalyst performance occurred.

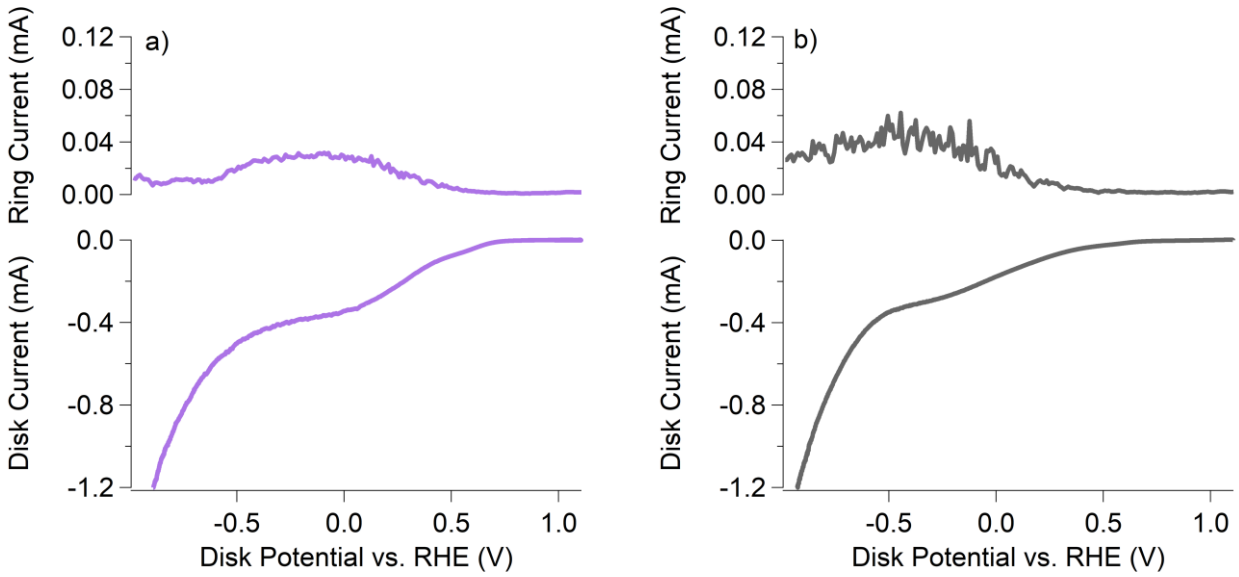

Figure C12. Rotating ring disk voltammogram of UDT-AgNP-BDD (a) and BDD (b) after going through the procedure used to deposit silver on the surface of the Ag-AuNP-BDD samples through the Cu UPD/galvanic exchange method. The lack of direct four-electron O_2 reduction compared to the Ag-AuNP-BDD samples suggests that the silver deposition method does not solely produce the ORR active sites. All scans were performed at 20 mV/s while the electrode was rotated at 500 rpm in 0.1 M KOH while O_2 was bubbling.

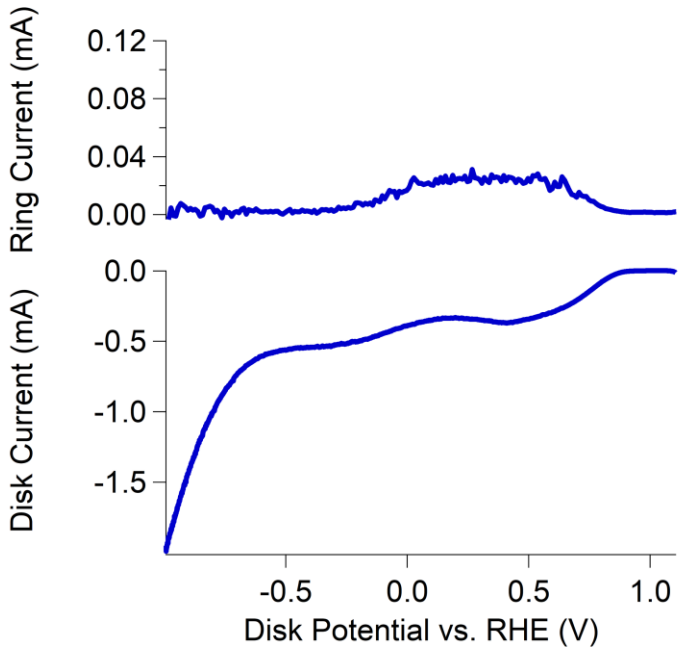

Figure C13. Rotating ring disk voltammogram of a UDT-AuNP-BDD sample with a small amount of Cu (Cu:Au ratio = 0.022 ± 0.001) on the AuNP surface used to assess ORR activity. The similar shape and ring current compared to UDT-AuNP alone indicates that trace copper possibly remaining after the galvanic replacement procedure used to install Ag on the AuNP surface is not responsible for the enhanced ORR activity observed in Ag-AuNP-BDD. Scan was performed at 20 mV/s while the electrode was rotated at 500 rpm in 0.1 M KOH while O_2 was bubbling.

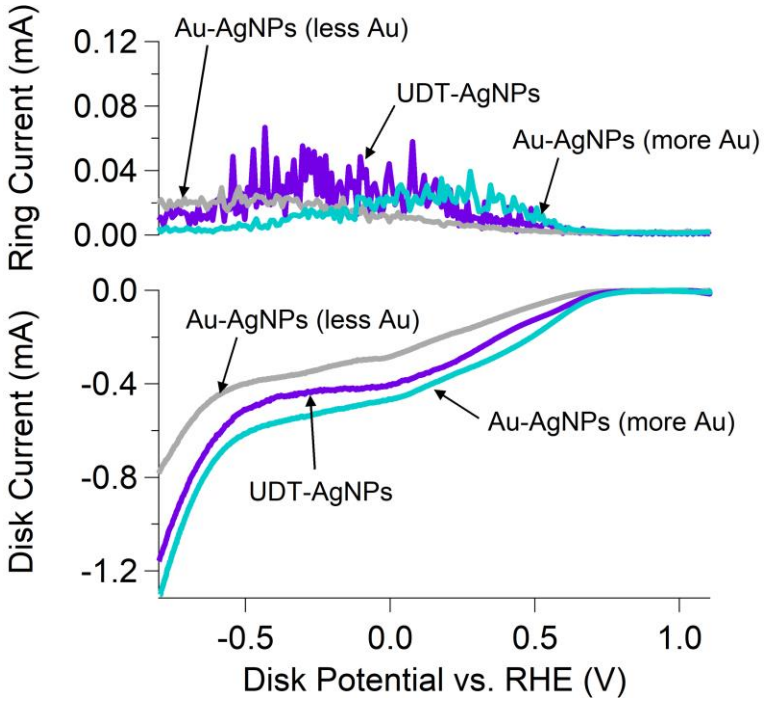

Figure C14. Rotating ring disk voltammograms of Au-AgNP-BDD with varying amounts of Au compared to UDT-AgNP-BDD. The significant ring currents and higher overpotentials compared to Ag-AuNP-BDD indicates that the addition of Au to AgNP cores did not induce ORR activity. All scans were performed at 20 mV/s while the electrode was rotated at 500 rpm in 0.1 M KOH while O_2 was bubbling.

Sample	*XPS Ag:Au (before)*	*XPS Ag:Au (after)*	*XPS Au:$C_{284.8}$ (before)*	*XPS Au:$C_{284.8}$ (after)*
0.50-Ag-AuNP-BDD	0.50 ± 0.01	0.53 ± 0.05	0.08 ± 0.02	0.023 ± 0.004
0.25-Ag-AuNP-BDD	0.25 ± 0.02	0.23 ± 0.01	0.08 ± 0.01	0.0230 ± 0.0003
0.48-Ag-AuNP-BDD	0.48 ± 0.05	0.39 ± 0.02	0.068 ± 0.004	0.022 ± 0.002

Table C1. XPS elemental ratios after electrochemical measurements to assess ORR activity.

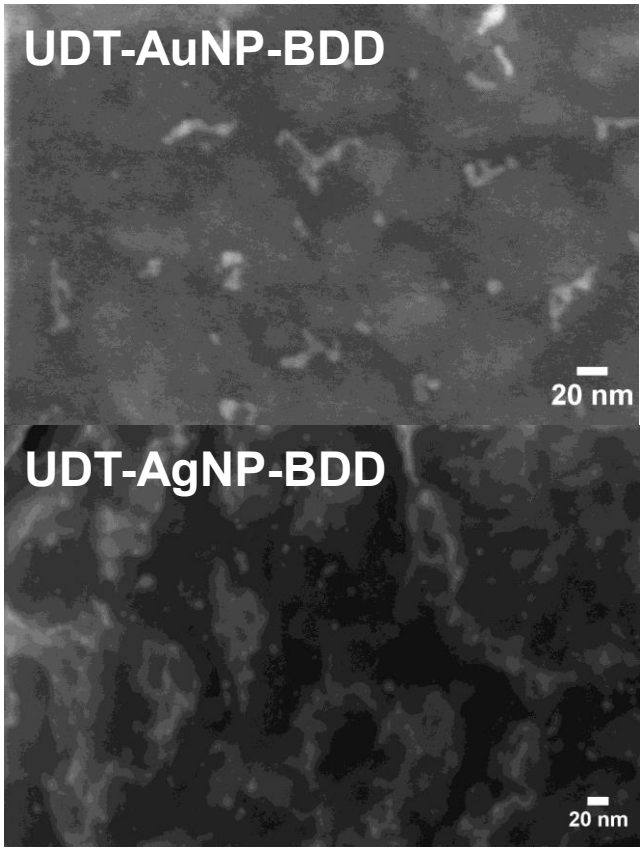

Figure C15. SEM images of **UDT-AuNP-BDD** (left) and **UDT-AgNP-BDD** (right) after rotating ring disk voltammetry measurements were taken showing some aggregation of the NPs on the BDD surface.

REFERENCES CITED

Chapter I

(1) Murray, R. W. *Acc. Chem. Res.* **1980**, *13* (5), 135.

(2) Xiao, W.; Lei, W.; Gong, M.; Xin, H. L.; Wang, D. *ACS Catal.* **2018**, *8* (4), 3237.

(3) Tang, Z.; Ma, Z. *Biosens. Bioelectron.* **2017**, *98* (June), 100.

(4) Cardoso, D. S. P.; Šljukić, B.; Santos, D. M. F.; Sequeira, C. A. C. *Org. Process Res. Dev.* **2017**, *21* (9), 1213.

(5) Mistry, H.; Reske, R.; Zeng, Z.; Zhao, Z.-J.; Greeley, J.; Strasser, P.; Cuenya, B. R. *J. Am. Chem. Soc.* **2014**, *136* (47), 16473.

(6) Seidel, Y. E.; Schneider, A.; Jusys, Z.; Wickman, B.; Kasemo, B.; Behm, R. J. *Faraday Discuss.* **2009**, *140*, 167.

(7) Mistry, H.; Behafarid, F.; Reske, R.; Varela, A. S.; Strasser, P.; Roldan Cuenya, B. *ACS Catal.* **2016**, *6* (2), 1075.

(8) Young, S. L.; Kellon, J. E.; Hutchison, J. E. *J. Am. Chem. Soc.* **2016**, *138* (42), 13975.

(9) Diao, P.; Zhang, D.; Wang, J.; Zhang, Q. *Electrochem. Commun.* **2010**, *12* (11), 1622.

Chapter II

(1) Kissling, G. P.; Miles, D. O.; Fermín, D. J. *Phys. Chem. Chem. Phys.* **2011**, *13* (48), 21175.

(2) Adams, D.; Brus, L.; Chidsey, C.; Creager, S.; Creutz, C.; Kagan, C.; Kamat, P.; Lieberman, M.; Lindsay, S.; Marcus, R.; Metzger, R.; Michel-Beyerle, M.; Miller, J.; Newton, M.; Rolison, D.; Sankey, O.; Schanze, K.; Yardley, J.; Zhu, X. *J. Phys. Chem. B* **2003**, *107* (28), 6668.

(3) Liu, F.; Khan, K.; Liang, J.-H.; Yan, J.-W.; Wu, D.-Y.; Mao, B.-W.; Jensen, P. S.; Zhang, J.; Ulstrup, J. *ChemPhysChem* **2013**, *14* (5), 952.

(4) Gittins, D. I.; Bethell, D.; Nichols, R. J.; Schiffrin, D. J. *Adv. Mater.* **1999**, *11* (9), 737.

(5) Gittins, D. I.; Bethell, D.; Schiffrin, D. J.; Nichols, R. J. *Nature* **2000**, *408* (6808), 67.

(6) Chou, A.; Eggers, P. K.; Paddon-Row, M. N.; Gooding, J. J. *J. Phys. Chem. C* **2009**, *113* (8), 3203.

(7) Shein, J. B.; Lai, L. M. H.; Eggers, P. K.; Paddon-Row, M. N.; Gooding, J. J. *Langmuir* **2009**, *25* (18), 11121.

(8) Suk, J.; Lee, J.; Kwak, J. *Bull. Korean Chem. Soc.* **2004**, *25* (11), 1681.

(9) Chirea, M.; Cruz, A.; Pereira, C. M.; Silva, A. F. **2009**, 13077.

(10) Jensen, P. S.; Chi, Q.; Zhang, J.; Ulstrup, J. *J. Phys. Chem. C* **2009**, *113* (31), 13993.

(11) Bakkers, E. P. A. M.; Roest, A. L.; Marsman, A. W.; Jenneskens, L. W.; de Jong-van Steensel, L. I.; Kelly, J. J.; Vanmaekelbergh, D. *J. Phys. Chem. B* **2000**, *104* (31), 7266.

(12) Baum, T.; Bethell, D.; Brust, M.; Schiffrin, D. J. *Langmuir* **1999**, *15* (2), 866.

(13) Musick, M. D.; Peña, D. J.; Botsko, S. L.; McEvoy, T. M.; Richardson, J. N.; Natan, M. J. *Langmuir* **1999**, *15* (3), 844.

(14) Ballarin, B.; Cassani, M. C.; Scavetta, E.; Tonelli, D. *Electrochim. Acta* **2008**, *53* (27), 8034.

(15) Cheng, W.; Dong, S.; Wang, E. *Anal. Chem.* **2002**, *74* (15), 3599.

(16) Doron, A.; Katz, E.; Willner, I. *Langmuir* **1995**, *11* (4), 1313.

(17) Tseng, J.-Y.; Lin, M.-H.; Chau, L.-K. *Colloids Surfaces A Physicochem. Eng. Asp.* **2001**, *182* (1–3), 239.

(18) Kondo, T.; Aoshima, S.; Honda, K.; Einaga, Y.; Fujishima, A.; Kawai, T. *J. Phys. Chem. C* **2007**, *111* (34), 12650.

(19) Cheng, W.; Dong, S.; Wang, E. *Langmuir* **2002**, *18* (25), 9947.

(20) Brust, M.; Bethell, D.; Kiely, C. J.; Schiffrin, D. J. *Langmuir* **1998**, *14* (19), 5425.

(21) Hongthani, W.; Fox, N. A.; Fermín, D. J. *Langmuir* **2011**, *27* (8), 5112.

(22) Montes de Oca, M. G.; Kumarakuru, H.; Cherns, D.; Fermín, D. J. *J. Phys. Chem. C* **2011**, *115* (21), 10489.

(23) Montes de Oca, M. G.; Fermín, D. J. *Electrochim. Acta* **2010**, *55* (28), 8986.

(24) Kissling, G. P.; Bünzli, C.; Fermín, D. J. *J. Am. Chem. Soc.* **2010**, *132* (47), 16855.

(25) Bradbury, C. R.; Zhao, J.; Fermín, D. J. *J. Phys. Chem. C* **2008**, *112* (27), 10153.

(26) Zhao, J.; Bradbury, C. R.; Fermín, D. J. *J. Phys. Chem. C* **2008**, *112* (17), 6832.

(27) Chirea, M.; García-Morales, V.; Manzanares, J. A.; Pereira, C.; Gulaboski, R.; Silva, F. *J. Phys. Chem. B* **2005**, *109* (46), 21808.

(28) Ottakam Thotiyl, M. M.; Basit, H.; Sánchez, J. A.; Goyer, C.; Coche-Guerente, L.; Dumy, P.; Sampath, S.; Labbé, P.; Moutet, J.-C. *J. Colloid Interface Sci.* **2012**, *383* (1), 130.

(29) Bradbury, C. R.; Bünzli, C.; Zhao, J.; Carrara, M.; Kissling, G. P.; Aslan-Guerel, E.; Fermín, D. J. *Chimia (Aarau).* **2008**, *62* (10), 841.

(30) Zhao, J.; Bradbury, C. R.; Huclova, S.; Potapova, I.; Carrara, M.; Fermín, D. J. *J. Phys. Chem. B* **2005**, *109* (48), 22985.

(31) Chirea, M.; Pereira, C. M.; Silva, F. *J. Phys. Chem. C* **2007**, *111* (26), 9255.

(32) Li, F.; Ciani, I.; Bertoncello, P.; Unwin, P. R.; Zhao, J.; Bradbury, C. R.; Fermin, D. J. *J. Phys. Chem. C* **2008**, *112* (26), 9686.

(33) Tang, Y.; Cheng, W. *Langmuir* **2013**, *29* (9), 3125.

(34) Xi, Q.; Chen, X.; Evans, D. G.; Yang, W. *Langmuir* **2012**, *28* (25), 9885.

(35) Cao, C.; Zhang, Y.; Jiang, C.; Qi, M.; Liu, G. *ACS Appl. Mater. Interfaces* **2017**, *9* (6), 5031.

(36) Gooding, J. J. *Electroanalysis* **2008**, *20* (6), 573.

(37) Bradbury, C. R.; Kuster, L.; Fermín, D. J. *J. Electroanal. Chem.* **2010**, *646* (1–2), 114.

(38) Lesniewski, A.; Matyjewicz, J.; Palys, B.; Niedziolka-Jonsson, J. *Electrochem. Commun.* **2015**, *53*, 20.

(39) Liu, G.; Luais, E.; Gooding, J. J. *Langmuir* **2011**, *27* (7), 4176.

(40) Lee, H. E.; Kang, Y. O.; Choi, S. H. *Int. J. Electrochem. Sci.* **2014**, *9* (12), 6793.

(41) Delamar, M.; Hitmi, R.; Pinson, J.; Savéant, J. *J. Am. Chem. Soc.* **1992**, *114* (14), 5883.

(42) González, M. C. R.; Orive, A. G.; Salvarezza, R. C.; Creus, A. H. *Phys. Chem. Chem. Phys.* **2016**, *18* (3), 1953.

(43) Liu, G.; Liu, J.; Davis, T. P.; Gooding, J. J. *Biosens. Bioelectron.* **2011**, *26* (8), 3660.

(44) Barfidokht, A.; Ciampi, S.; Luais, E.; Darwish, N.; Gooding, J. J. *Anal. Chem.* **2013**, *85* (2), 1073.

(45) Strother, T.; Knickerbocker, T.; Russell, J. N.; Butler, J. E.; Smith, L. M.; Hamers, R. J. *Langmuir* **2002**, *18* (4), 968.

(46) Wang, X.; Landis, E. C.; Franking, R.; Hamers, R. J. *Acc. Chem. Res.* **2010**, *43* (9), 1205.

(47) Tian, R.; Rao, T. N.; Einaga, Y.; Zhi, J. *Chem. Mater.* **2006**, *18* (4), 939.

(48) Young, S. L.; Kellon, J. E.; Hutchison, J. E. *J. Am. Chem. Soc.* **2016**, *138* (42), 13975.

(49) Nakamura, T.; Ohana, T. *Jpn. J. Appl. Phys.* **2012**, *51*, 85201.

(50) Le Saux, G.; Ciampi, S.; Gaus, K.; Gooding, J. J. *ACS Appl. Mater. Interfaces* **2009**, *1* (11), 2477.

(51) Kashi, M. B.; Wu, Y.; Gonçales, V. R.; Choudhury, M. H.; Ciampi, S.; Gooding, J. J. *Electrochem. Commun.* **2016**, *70*, 28.

(52) Kolb, H. C.; Finn, M. G.; Sharpless, K. B. *Angew. Chemie Int. Ed.* **2001**, *40*, 2004.

(53) Matyjewicz, J.; Lesniewski, A.; Niedziolka-Jonsson, J. *Electrochem. Commun.* **2014**, *48*, 73.

(54) Upadhyay, A. P.; Behara, D. K.; Sharma, G. P.; Bajpai, A.; Sharac, N.; Ragan, R.; Pala, R. G. S.; Sivakumar, S. *ACS Appl. Mater. Interfaces* **2013**, *5* (19), 9554.

(55) Fratila, R. M.; Navascuez, M.; Idiago-López, J.; Eceiza, M.; Miranda, J. I.; Aizpurua, J. M.; de la Fuente, J. M. *New J. Chem.* **2017**, 10835.

(56) Jensen, P. S.; Chi, Q.; Grumsen, F. B.; Abad, J. M.; Horsewell, A.; Schiffrin, D. J.; Ulstrup, J. *J. Phys. Chem.* **2007**, *111*, 6124.

(57) Nguyen, T. T.; Sly, K. L.; Conboy, J. C. *Anal. Chem.* **2012**, *84* (1), 201.

(58) Kar, P.; Tatard, F.; Lamblin, G.; Banet, P.; Aubert, P. H.; Plesse, C.; Chevrot, C. *J. Electroanal. Chem.* **2013**, *692*, 17.

(59) Huang, X.; Du, D.; Gong, X.; Cai, J.; Tu, H.; Xu, X.; Zhang, A. *Electroanalysis* **2008**, *20* (4), 402.

(60) Damos, F. S.; Luz, R. C. S.; Tanaka, A. A.; Kubota, L. T. *J. Electroanal. Chem.* **2010**, *639* (1–2), 36.

(61) Zuo, F.; Luo, C.; Zheng, Z.; Ding, X.; Peng, Y. *Electroanalysis* **2008**, *20* (8), 894.

(62) Hicks, J. F.; Zamborini, F. P.; Murray, R. W. *J. Phys. Chem. B* **2002**, *106* (32), 7751.

(63) Yamanoi, Y.; Shirahata, N.; Yonezawa, T.; Terasaki, N.; Yamamoto, N.; Matsui, Y.; Nishio, K.; Masuda, H.; Ikuhara, Y.; Nishihara, H. *Chem. - A Eur. J.* **2006**, *12* (1), 314.

(64) Liu, G.; Qi, M.; Zhang, Y.; Cao, C.; Goldys, E. M. *Anal. Chim. Acta* **2016**, *909*, 1.

(65) Strong, L.; Whitesides, G. M. *Langmuir* **1988**, *4* (3), 546.

(66) Laibinis, P. E.; Whitesides, G. M.; Allara, D. L.; Tao, Y. T.; Parikh, A. N.; Nuzzo, R. G. *J. Am. Chem. Soc.* **1991**, *113* (19), 7152.

(67) Zamborini, F. P.; Crooks, R. M. **1998**, *7463* (4), 3279.

(68) Schoenenberger, C.; Sondag-Huethorst, J. A. M.; Jorritsma, J.; Fokkink, L. G. J. *Langmuir* **1994**, *10* (3), 611.

(69) Edinger, K.; Goelzhaeuser, A.; Demota, K.; Woell, C.; Grunze, M. *Langmuir* **1993**, *9* (1), 4.

(70) Ruther, R. E.; Cui, Q.; Hamers, R. J. *J. Am. Chem. Soc.* **2013**, *135* (15), 5751.

(71) Adenier, A.; Combellas, C.; Kanoufi, F.; Pinson, J.; Podvorica, F. I. *Chem. Mater.* **2006**, *18* (8), 2021.

(72) Menanteau, T.; Dias, M.; Levillain, E.; Downard, A. J.; Breton, T. *J. Phys. Chem. C* **2016**, *120* (8), 4423.

(73) Menanteau, T.; Levillain, E.; Downard, A. J.; Breton, T. *Phys. Chem. Chem. Phys.* **2015**, *17* (19), 13137.

(74) Leroux, Y. R.; Fei, H.; Noël, J. M.; Roux, C.; Hapiot, P. *J. Am. Chem. Soc.* **2010**, *132* (40), 14039.

(75) Lee, L.; Ma, H.; Brooksby, P. A.; Brown, S. A.; Leroux, Y. R.; Hapiot, P.; Downard, A. J. *Langmuir* **2014**, *30* (24), 7104.

(76) Combellas, C.; Kanoufi, F.; Pinson, J.; Podvorica, F. I. *J. Am. Chem. Soc.* **2008**, *130* (27), 8576.

(77) Chirea, M.; Borges, J.; Pereira, C. M.; Silva, A. F. *J. Phys. Chem. C* **2010**, *114* (20), 9478.

(78) Chazalviel, J.; Allongue, P. *J. Am. Chem. Soc.* **2011**, *133*, 762.

(79) Macpherson, J. V. *Phys. Chem. Chem. Phys.* **2015**, *17* (5), 2935.

(80) Ruther, R. E.; Rigsby, M. L.; Gerken, J. B.; Hogendoorn, S. R.; Landis, E. C.; Stahl, S. S.; Hamers, R. J. *J. Am. Chem. Soc.* **2011**, *133*, 5692.

(81) Widrig, C. A.; Chung, C.; Porter, M. D. *J. Electroanal. Chem.* **1991**, *310* (1–2), 335.

(82) Muglali, M. I.; Erbe, A.; Chen, Y.; Barth, C.; Koelsch, P.; Rohwerder, M. *Electrochim. Acta* **2013**, *90*, 17.

(83) Lee, J.; Hwang, S.; Lee, H.; Kwak, J. *J. Phys. Chem. B* **2004**, *108* (17), 5372.

(84) Young, S. L.; Hutchison, J. E. **2018,** *Manuscript in preparation*.

Chapter III

(1) Saha, K.; Agasti, S. S.; Kim, C.; Li, X.; Rotello, V. M. *Chem. Rev.* **2012**, *112*, 2739–2779.

(2) Segev-Bar, M.; Haick, H. *ACS Nano* **2013**, *7*, 8366–8378.

(3) Oszajca, M. F.; Bodnarchuk, M. I.; Kovalenko, M. V. *Chem. Mater.* **2014**, *26*, 5422–5432.

(4) Oezaslan, M.; Hasché, F.; Strasser, P. *J. Phys. Chem. Lett.* **2013**, *4*, 3273–3291.

(5) Corma, A.; Garcia, H. *Chem. Soc. Rev.* **2008**, *37*, 2096–2126.

(6) Kleijn, S. E. F.; Lai, S. C. S.; Koper, M. T. M.; Unwin, P. R. *Angew. Chemie Int. Ed.* **2014**, *53*, 3558–3586.

(7) Schünemann, S.; Dodekatos, G.; Tüysüz, H. *Chem. Mater.* **2015**, *27*, 7743–7750.

(8) Zhu, M.; Diao, G. *J. Phys. Chem. C* **2011**, *115*, 24743–24749.

(9) Taniguchi, K.; Jin, X.; Yamaguchi, K.; Mizuno, N. *Chem. Commun.* **2015**, *51*, 14969–15082.

(10) Willner, I.; Willner, B. *Nano Lett.* **2010**, *10*, 3805–3815.

(11) Yu, A.; Liang, Z.; Cho, J.; Caruso, F. *Nano Lett.* **2003**, *3*, 1203–1207.

(12) Tsukamoto, D.; Shiraishi, Y.; Sugano, Y.; Ichikawa, S.; Tanaka, S.; Hirai, T. *J. Am. Chem. Soc.* **2012**, *134*, 6309–6315.

(13) Tang, Y.; Cheng, W. *Langmuir* **2013**, *29*, 3125–3132.

(14) Barfidokht, A.; Ciampi, S.; Luais, E.; Darwish, N.; Gooding, J. J. *Anal. Chem.* **2013**, *85*, 1073–1080.

(15) Bradbury, C. R.; Zhao, J.; Fermín, D. J. *J. Phys. Chem. C* **2008**, *112*, 10153–10160.

(16) Kauffman, D. R.; Alfonso, D.; Matranga, C.; Qian, H.; Jin, R. *J. Am. Chem. Soc.* **2012**, *134*, 10237–10243.

(17) Cao, Z.; Kim, D.; Hong, D.; Yu, Y.; Xu, J.; Lin, S.; Wen, X.; Nichols, E. M.; Jeong, K.; Reimer, J. A.; Yang, P.; Chang, C. J. *J. Am. Chem. Soc.* **2016**, *138*, 8120–8125.

(18) Zhu, W.; Michalsky, R.; Metin, O.; Lv, H.; Guo, S.; Wright, C. J.; Sun, X.; Peterson, A. A.; Sun, S. *J. Am. Chem. Soc.* **2013**, *135*, 16833–16836.

(19) Wang, J. X.; Inada, H.; Wu, L.; Zhu, Y.; Choi, Y.; Liu, P.; Zhou, W. P.; Adzic, R. R. *J. Am. Chem. Soc.* **2009**, *131*, 17298–17302.

(20) Padayachee, D.; Golovko, V.; Ingham, B.; Marshall, A. T. *Electrochim. Acta* **2014**, *120*, 398–407.

(21) Lee, H. *RSC Adv.* **2014**, *4*, 41017–41027.

(22) Seidel, Y. E.; Schneider, A.; Jusys, Z.; Wickman, B.; Kasemo, B.; Behm, R. J. *Langmuir* **2010**, *26*, 3569–3578.

(23) Diao, P.; Guo, M.; Zhang, Q. *J. Phys. Chem. C* **2008**, *112*, 7036–7046.

(24) Sun, X.; Guo, S.; Liu, Y.; Sun, S. *Nano Lett.* **2012**, *12*, 4859–4863.

(25) Weng, Z.; Liu, W.; Yin, L. C.; Fang, R.; Li, M.; Altman, E. I.; Fan, Q.; Li, F.; Cheng, H. M.; Wang, H. *Nano Lett.* **2015**, *15*, 7704–7710.

(26) Diao, P.; Zhang, D.; Wang, J.; Zhang, Q. *Electrochem. Commun.* **2010**, *12*, 1622–1625.

(27) Tang, Y.; Cheng, W. *Nanoscale* **2015**, *7*, 16151–16164.

(28) Chen, W.; Chen, S. *Angew. Chem. Int. Ed. Engl.* **2009**, *48*, 4386–4389.

(29) Reske, R.; Mistry, H.; Behafarid, F.; Cuenya, B. R.; Strasser, P. *J. Am. Chem. Soc.* **2014**, *136*, 6978–6986.

(30) Salehi-Khojin, A.; Jhong, H. R. M.; Rosen, B. A.; Zhu, W.; Ma, S.; Kenis, P. J. A.; Masel, R. I. *J. Phys. Chem. C* **2013**, *117*, 1627–1632.

(31) Masuda, H.; Yasui, K.; Nishio, K. *Adv. Mater.* **2000**, *12*, 1031–1033.

(32) Penner, R. M. *J. Phys. Chem. B* **2002**, *106*, 3339–3353.

(33) Ivanova, O. S.; Zamborini, F. P. *Anal. Chem.* **2010**, *82*, 5844–5850.

(34) Lopez-Serrano, A.; Olivas, R. M.; Landaluze, J. S.; Camara, C. *Anal. Methods* **2014**, *6*, 38–56.

(35) Smith, B. L.; Hutchison, J. E. *J. Phys. Chem. C* **2013**, *117*, 25127–25137.

(36) Lopez-Sanchez, J. A.; Dimitratos, N.; Hammond, C.; Brett, G. L.; Kesavan, L.; White, S.; Miedziak, P.; Tiruvalam, R.; Jenkins, R. L.; Carley, A. F.; Knight, D.; Kiely, C. J.; Hutchings, G. J. *Nat. Chem.* **2011**, *3*, 551–556.

(37) Kilmartin, J.; Sarip, R.; Grau-Crespo, R.; Di Tommaso, D.; Hogarth, G.; Prestipino, C.; Sankar, G. *ACS Catal.* **2012**, *2*, 957–963.

(38) Shein, J. B.; Lai, L. M. H.; Eggers, P. K.; Paddon-Row, M. N.; Gooding, J. J. *Langmuir* **2009**, *25*, 11121–11128.

(39) Jensen, P. S.; Chi, Q.; Grumsen, F. B.; Abad, J. M.; Horsewell, A.; Schiffrin, D. J.; Ulstrup, J. *J. Phys. Chem.* **2007**, *111*, 6124–6132.

(40) Liu, F.; Khan, K.; Liang, J.-H.; Yan, J.-W.; Wu, D.-Y.; Mao, B.-W.; Jensen, P. S.; Zhang, J.; Ulstrup, J. *ChemPhysChem* **2013**, *14*, 952–957.

(41) Liu, G.; Luais, E.; Gooding, J. J. *Langmuir* **2011**, *27*, 4176–4183.

(42) Matyjewicz, J.; Lesniewski, A.; Niedziolka-Jonsson, J. *Electrochem. Commun.* **2014**, *48*, 73–76.

(43) Le Saux, G.; Ciampi, S.; Gaus, K.; Gooding, J. J. *ACS Appl. Mater. Interfaces* **2009**, *1*, 2477–2483.

(44) Tian, R.; Rao, T. N.; Einaga, Y.; Zhi, J. *Chem. Mater.* **2006**, *18*, 939–945.

(45) Kondo, T.; Aoshima, S.; Honda, K.; Einaga, Y.; Fujishima, A.; Kawai, T. *J. Phys. Chem. C* **2007**, *111*, 12650–12657.

(46) Widrig, C. A.; Chung, C.; Porter, M. D. *J. Electroanal. Chem.* **1991**, *310*, 335–359.

(47) Boubour, E.; Lennox, R. B. *Langmuir* **2000**, *16*, 7464–7470.

(48) Mattiuzzi, A.; Jabin, I.; Mangeney, C.; Roux, C.; Reinaud, O.; Santos, L.; Bergamini, J.-F.; Hapiot, P.; Lagrost, C. *Nat. Commun.* **2012**, *3*, 1130.

(49) McCreery, R. L. *Chem. Rev.* **2008**, *108*, 2646–2687.

(50) Li, G.; Jin, R. *Acc. Chem. Res.* **2013**, *46*, 1749–1758.

(51) Mckenzie, L. C.; Zaikova, T. O.; Hutchison, J. E. *J. Am. Chem. Soc.* **2014**, *136*, 13426–13435.

(52) Hicks, J. F.; Zamborini, F. P.; Murray, R. W. *J. Phys. Chem. B* **2002**, *106*, 7751–7757.

(53) Strother, T.; Knickerbocker, T.; Russell, J. N.; Butler, J. E.; Smith, L. M.; Hamers, R. J. *Langmuir* **2002**, *18*, 968–971.

(54) Ilavsky, J.; Jemian, P. R. *J. Appl. Crystallogr.* **2009**, *42*, 347–353.

(55) Yamanoi, Y.; Shirahata, N.; Yonezawa, T.; Terasaki, N.; Yamamoto, N.; Matsui, Y.; Nishio, K.; Masuda, H.; Ikuhara, Y.; Nishihara, H. *Chem. - A Eur. J.* **2006**, *12*, 314–323.

(56) Weare, W. W.; Reed, S. M.; Warner, M. G.; Hutchison, J. E. *J. Am. Chem. Soc.* **2000**, *122*, 12890–12891.

(57) Seshan, V.; Ullien, D.; Castellanos-Gomez, A.; Sachdeva, S.; Murthy, D. H. K.; Savenije, T. J.; Ahmad, H. A.; Nunney, T. S.; Janssens, S. D.; Haenen, K.; Nesládek, M.; van der Zant, H. S. J.; Sudhölter, E. J. R.; de Smet, L. C. P. M. *J. Chem. Phys.* **2013**, *138*, 234707.

(58) Nichols, B. M.; Butler, J. E.; Russell, J. N.; Hamers, R. J. *J. Phys. Chem. B* **2005**, *109*, 20938–20947.

(59) Woehrle, G. H.; Hutchison, J. E. *Inorg. Chem.* **2005**, *44*, 6149–6158.

(60) Chidsey, C. E. D.; Bertozzi, C. R.; Putvinski, T. M.; Mujsce, A. M. *J. Am. Chem. Soc.* **1990**, *112*, 4301–4306.

(61) Elliott, E. W.; Glover, R. D.; Hutchison, J. E. *ACS Nano* **2015**, *9*, 3050–3059.

(62) Macpherson, J. V. *Phys. Chem. Chem. Phys.* **2015**, *17*, 2935–2949.

(63) Woehrle, G. H.; Brown, L. O.; Hutchison, J. E. *J. Am. Chem. Soc.* **2005**, *127*, 2172–2183.

(64) Woehrle, G. H.; Warner, M. G.; Hutchison, J. E. *J. Phys. Chem. B* **2002**, *106*, 9979–9981.

(65) Ingram, R. S.; Hostetler, M. J.; Murray, R. W. *J. Am. Chem. Soc.* **1997**, *119*, 9175–9178.

(66) Chazalviel, J.; Allongue, P. *J. Am. Chem. Soc.* **2011**, *133*, 762–764.

(67) Patten, H. V.; Lai, S. C. S.; MacPherson, J. V.; Unwin, P. R. *Anal. Chem.* **2012**, *84*, 5427–5432.

(68) Patten, H. V.; Meadows, K. E.; Hutton, L. A.; Iacobini, J. G.; Battistel, D.; McKelvey, K.; Colburn, A. W.; Newton, M. E.; MacPherson, J. V.; Unwin, P. R. *Angew. Chemie - Int. Ed.* **2012**, *51*, 7002–7006.

(69) Ruther, R. E.; Cui, Q.; Hamers, R. J. *J. Am. Chem. Soc.* **2013**, *135*, 5751–5761.

(70) Li, Y.; Huang, W.; Sun, S. *Angew. Chemie* **2006**, *118*, 2599–2601.

(71) Reincke, F.; Hickey, S. G.; Kegel, W. K.; Vanmaekelbergh, D. *Angew. Chemie* **2004**, *116*, 464–468.

(72) Chen, S. *Langmuir* **2001**, *17*, 6664–6668.

(73) Trasatti, S.; Petrii, O. *Pure Appl. Chem.* **1991**, *63*, 711–734.

(74) Wang, X.; Ruther, R. E.; Streifer, J. A.; Hamers, R. J. *J. Am. Chem. Soc.* **2010**, *132*, 4048–4049.

(75) Maat, J. Ter; Regeling, R.; Yang, M.; Mullings, M. N.; Bent, S. F.; Zuilhof, H. *Langmuir* **2009**, *25*, 11592–11597.

(76) Franking, R.; Kim, H.; Chambers, S. A.; Mangham, A. N.; Hamers, R. J. *Langmuir* **2012**, *28*, 12085–12093.

(77) Colavita, P. E.; Sun, B.; Tse, K. Y.; Hamers, R. J. *J. Am. Chem. Soc.* **2007**, *129*, 13554–13565.

Chapter IV

(1) Xiao, W.; Lei, W.; Gong, M.; Xin, H. L.; Wang, D. *ACS Catal.* **2018**, *8* (4), 3237.

(2) Rick, J.; Tsai, M.; Hwang, B. *Nanomaterials* **2016**, *6* (1), 5.

(3) Cardoso, D. S. P.; Šljukić, B.; Santos, D. M. F.; Sequeira, C. A. C. *Org. Process Res. Dev.* **2017**, *21* (9), 1213.

(4) Zhu, M.; Aikens, C. M.; Hollander, F. J.; Schatz, G. C.; Jin, R. *J. Am. Chem. Soc.* **2008**, *130* (18), 5883.

(5) Hicks, J. F.; Miles, D. T.; Murray, R. W. *J. Am. Chem. Soc.* **2002**, *124* (44), 13322.

(6) Li, G.; Jin, R. *Acc. Chem. Res.* **2013**, *46* (8), 1749.

(7) Chen, W.; Chen, S. *Angew. Chemie Int. Ed.* **2009**, *48* (24), 4386.

(8) Young, S. L.; Hutchison, J. E. **2018** *Manuscript in preparation*.

(9) Baez, V. B.; Pletcher, D. *J. Electroanal. Chem.* **1995**, *382* (1–2), 59.

(10) Taylor, R. J.; Humffray, A. A. *J. Electroanal. Chem. Interfacial Electrochem.* **1975**, *64* (1), 63.

(11) Young, S. L.; Kellon, J. E.; Hutchison, J. E. *J. Am. Chem. Soc.* **2016**, *138* (42), 13975.

(12) Anderson, D. P.; Alvino, J. F.; Gentleman, A.; Qahtani, H. Al; Thomsen, L.; Polson, M. I. J.; Metha, G. F.; Golovko, V. B.; Andersson, G. G. *Phys. Chem. Chem. Phys.* **2013**, *15* (11), 3917.

(13) Mckenzie, L. C.; Zaikova, T. O.; Hutchison, J. E. *J. Am. Chem. Soc.* **2014**, *136*, 13426.

(14) Weare, W. W.; Reed, S. M.; Warner, M. G.; Hutchison, J. E. *J. Am. Chem. Soc.* **2000**, *122* (17), 12890.

(15) Woehrle, G. H.; Hutchison, J. E. *Inorg. Chem.* **2005**, *44* (18), 6149.

(16) Woehrle, G. H.; Brown, L. O.; Hutchison, J. E. *J. Am. Chem. Soc.* **2005**, *127* (7), 2172.

(17) Niu, Z.; Li, Y. *Chem. Mater.* **2014**, *26*, 72.

(18) Seidel, Y. E.; Schneider, A.; Jusys, Z.; Wickman, B.; Kasemo, B.; Behm, R. J. *Faraday Discuss.* **2009**, *140*, 167.

(19) Seidel, Y.; Jusys, Z.; Wickman, B.; Kasemo, B.; Behm, R. J. *ECS Transitions* **2010**, *25* (23), 91.

Chapter V

(1) Xiao, W.; Lei, W.; Gong, M.; Xin, H. L.; Wang, D. *ACS Catal.* **2018**, *8* (4), 3237.

(2) Tang, Z.; Ma, Z. *Biosens. Bioelectron.* **2017**, *98* (June), 100.

(3) Allioux, F.; David, O.; Merenda, A.; Maina, J. W.; Benavides, M. E.; Tanaka, A. P.; Dumée, L. F. *J. Mater. Chem. A* **2018**, Advance Article.

(4) Cardoso, D. S. P.; Šljukić, B.; Santos, D. M. F.; Sequeira, C. A. C. *Org. Process Res. Dev.* **2017**, *21* (9), 1213.

(5) Chen, G.; Kuttiyiel, K. A.; Su, D.; Li, M.; Wang, C. H.; Buceta, D.; Du, C.; Gao, Y.; Yin, G.; Sasaki, K.; Vukmirovic, M. B.; Adzic, R. R. *Chem. Mater.* **2016**, *28* (15), 5274.

(6) Oezaslan, M.; Hasché, F.; Strasser, P. *J. Phys. Chem. Lett.* **2013**, *4* (19), 3273.

(7) Tang, Y.; Cheng, W. *Nanoscale* **2015**, *7* (39), 16151.

(8) Young, S. L.; Kellon, J. E.; Hutchison, J. E. *J. Am. Chem. Soc.* **2016**, *138* (42), 13975.

(9) Song, C.; Zhang, J. In *PEM Fuel Cell Electrocatalysts and Catalyst Layers*; Springer London: London, 2008; pp 89–134.

(10) Ge, X.; Sumboja, A.; Wuu, D.; An, T.; Li, B.; Goh, F. W. T.; Hor, T. S. A.; Zong, Y.; Liu, Z. *ACS Catal.* **2015**, *5* (8), 4643.

(11) Gorlin, Y.; Chung, C.; Nordlund, D. *ACS Catal.* **2012**, *2*, 2687−2694.

(12) Liang, J.; Jiao, Y.; Jaroniec, M.; Qiao, S. Z. *Angew. Chemie - Int. Ed.* **2012**, *51* (46), 11496.

(13) Huang, Y.-X.; Xie, J.-F.; Zhang, X.; Xiong, L.; Yu, H.-Q. *ACS Appl. Mater. Interfaces* **2014**, *6* (18), 15795.

(14) Singh, P.; Buttry, D. A. *J. Phys. Chem. C* **2012**, *116* (19), 10656.

(15) Chen, W.; Chen, S. *Angew. Chemie Int. Ed.* **2009**, *48* (24), 4386.

(16) Chen, L.; Deming, C. P.; Peng, Y.; Hu, P.; Stofan, J.; Chen, S. *Nanoscale* **2016**, *8* (30), 14565.

(17) Song, Y.; Liu, K.; Chen, S. *Langmuir* **2012**, *28* (49), 17143.

(18) Wang, Q.; Yang, H.; Zhou, Z.; Wang, L.; Yan, W.; Wu, W.; Chen, S.; Liu, Z.; Tang, Z. *Int. J. Hydrogen Energy* **2017**, *42* (16), 11295.

(19) Hu, P.; Song, Y.; Chen, L.; Chen, S. *Nanoscale* **2015**, *7* (21), 9627.

(20) Pradhan, S.; Hedberg, J.; Blomberg, E.; Wold, S.; Odnevall Wallinder, I. *J. Nanoparticle Res.* **2016**, *18* (9), 1.

(21) Taylor, R. J.; Humffray, A. A. *J. Electroanal. Chem* **1975**, *64*, 63.

(22) Yamanoi, Y.; Shirahata, N.; Yonezawa, T.; Terasaki, N.; Yamamoto, N.; Matsui, Y.; Nishio, K.; Masuda, H.; Ikuhara, Y.; Nishihara, H. *Chem. - A Eur. J.* **2006**, *12* (1), 314.

(23) Elliott, E. W.; Glover, R. D.; Hutchison, J. E. *ACS Nano* **2015**, *9* (3), 3050.

(24) Herrero, E.; Buller, L. J.; Abruna, H. D. *Chem. Rev.* **2001**, *101* (7), 1897.

(25) Lee, J.; Hwang, S.; Lee, H.; Kwak, J. *J. Phys. Chem. B* **2004**, *108* (17), 5372.

(26) Price, S. W. T.; Speed, J. D.; Kannan, P.; Russell, A. E. *J. Am. Chem. Soc.* **2011**, *133* (48), 19448.

(27) Wu, Z. *Angew. Chemie - Int. Ed.* **2012**, *51* (12), 2934.

(28) Yao, C.; Chen, J.; Li, M.-B.; Liu, L.; Yang, J.; Wu, Z. *Nano Lett.* **2015**, *15* (2), 1281.

(29) Liu, M.; Chi, F.; Liu, J.; Song, Y.; Wang, F. *RSC Adv.* **2016**, *6* (67), 62327.

(30) Polavarapu, L.; Liz-Marzán, L. M. *Nanoscale* **2013**, *5* (10), 4355.

(31) Sun, Y.; Wang, Y. *Nano Lett.* **2011**, *11* (10), 4386.

Chapter VI

(1) Jansons, A. W.; Hutchison, J. E. *ACS Nano* **2016**, *10* (7), 6942.

(2) Lee, J.; Hwang, S.; Lee, H.; Kwak, J. *J. Phys. Chem. B* **2004**, *108* (17), 5372.

(3) Price, S. W. T.; Speed, J. D.; Kannan, P.; Russell, A. E. *J. Am. Chem. Soc.* **2011**, *133* (48), 19448.

(4) Young, S. L.; Hutchison, J. E. **2018**.

(5) Weber, K.; Creager, S. E. *Anal. Chem.* **1994**, *66* (19), 3164.

(6) Liu, G.; Luais, E.; Gooding, J. J. *Langmuir* **2011**, *27* (7), 4176.

(7) Zhang, X.; Su, Z. *Adv. Mater.* **2012**, *24* (33), 4574.

(8) Mistry, H.; Behafarid, F.; Reske, R.; Varela, A. S.; Strasser, P.; Roldan Cuenya, B. *ACS Catal.* **2016**, *6* (2), 1075.

(9) Seidel, Y. E.; Schneider, A.; Jusys, Z.; Wickman, B.; Kasemo, B.; Behm, R. J. *Faraday Discuss.* **2009**, *140*, 167.

(10) Minguzzi, A.; Lugaresi, O.; Achilli, E.; Locatelli, C.; Vertova, A.; Ghigna, P.; Rondinini, S. *Chem. Sci.* **2014**, *5* (9), 3591.

(11) Cortes, F. J. Q.; Boebinger, M. G.; Xu, M.; Ulvestad, A.; McDowell, M. T. *ACS Energy Lett.* **2018**, *3* (2), 349.

(12) Chapman, K. W. *MRS Bull.* **2016**, *41* (3), 231.

(13) Zhang, C.; Grass, M. E.; Yu, Y.; Gaskell, K. J.; Decaluwe, S. C.; Chang, R.; Jackson, G. S.; Hussain, Z.; Bluhm, H.; Eichhorn, B. W.; Liu, Z. *ACS Catal.* **2012**, *2* (11), 2297.

(14) Mehdi, B. L.; Gu, M.; Parent, L. R.; Xu, W.; Nasybulin, E. N.; Chen, X.; Unocic, R. R.; Xu, P.; Welch, D. A.; Abellan, P.; Zhang, J. G.; Liu, J.; Wang, C. M.; Arslan, I.; Evans, J.; Browning, N. D. *Microsc. Microanal.* **2014**, *20* (2), 484.

Appendix B

(1) Anderson, D. P.; Alvino, J. F.; Gentleman, A.; Qahtani, H. Al; Thomsen, L.; Polson, M. I. J.; Metha, G. F.; Golovko, V. B.; Andersson, G. G. *Phys. Chem. Chem. Phys.* **2013**, *15* (11), 3917.

(2) Mckenzie, L. C.; Zaikova, T. O.; Hutchison, J. E. *J. Am. Chem. Soc.* **2014**, *136*, 13426.

(3) Weare, W. W.; Reed, S. M.; Warner, M. G.; Hutchison, J. E. *J. Am. Chem. Soc.* **2000**, *122* (17), 12890.

(4) Young, S. L.; Kellon, J. E.; Hutchison, J. E. *J. Am. Chem. Soc.* **2016**, *138* (42), 13975.

(5) Woehrle, G. H.; Hutchison, J. E. *Inorg. Chem.* **2005**, *44* (18), 6149.